Cu, Zn-based catalysts for methanol synthesis

vorgelegt von
Diplom-Chemikerin
Julia Schumann (geb. Neuendorf)
geb. in Berlin

von der Fakultät II - Mathematik und Naturwissenschaften
der Technischen Universität Berlin
zur Erlangung des akademischen Grades
Doktor der Naturwissenschaften
– Dr. rer. nat. –
genehmigte Dissertation

Promotionsausschuss:

Vorsitzender: Prof. Dr. rer. nat. Thorsten Ressler
Gutachter: Prof. Dr. rer. nat. Robert Schlögl
Gutachter: Prof. Dr. rer. nat. Reinhard Schomäcker
Gutachter: Prof. Dr. rer. nat. Malte Behrens

Tag der wissenschaftlichen Aussprache: 26.02.2015

Berlin 2015

Dans la vie, rien n'est à craindre,
tout est à comprendre.

(Marie Curie)

Acknowledgement

I would like to express my sincere gratitude to my advisor Prof. Dr. Robert Schlögl, Director of the Department of Inorganic Chemistry at the Fritz-Haber-Institute of the Max-Planck-Society, for the opportunity to work at his institute and for his support. Thanks to his guidance and the productive work environment he created at his department, I was able to accomplish my PhD project.

My special thanks and appreciation go to my supervisor Prof. Dr. Malte Behrens, former leader of the nanostructures group, for his guidance but also the freedom to develop and follow my own scientific curiosity. I am truly grateful for his positive, encouraging, and motivating style and his continuing support.

I would like to particularly acknowledge Prof. Dr. Reinhard Schomäcker, who accepted to invest his valuable time in reviewing this work. Additional gratitude goes to Prof. Dr. Thorsten Ressler for taking the chair of the examination board.

I thank my co-authors for their contributions to the manuscripts and the paper included in this dissertation, in alphabetical order: Consuelo Álvarez Galván, Maik Eichelbaum, José Luis García Fierro, Elias Frei, Thomas Lunkenbein, Andrey Tarasov and Nygil Thomas.

Furthermore, I thank Michael Hävecker for his support during several beam times at Bessy, Pierre Kube for his introduction into catalytic and kinetic measurements and all the technical staff of the department for their routine measurements and support.

I thank all the former members of the Cu-team, especially Steffi Kühl and Stefan Zander for their help and care introducing me to all the standard techniques required for the preparation and characterization of copper-based catalysts, and Frank Girgsdies for his advices concerning XRD.

Additionally, I thank Maria Heenemann for proof-reading the part about MCPT, and Steffi for valuable comments and help with LaTeX.

I thank the cooperation partners of the Cu-IX project from TU Munich and RUB for a fruitful collaboration and Clariant Produkte (Deutschland) GmbH for financial support.

At this point I would like to express my gratitude to my fellow collegues not only for the daily support in my research work, but also for the daily company and the sometimes neccessary distraction from science during lunch and coffee breaks. Thanks Kathi, Pia and Youngmi! I will never forget the fun we had at conferences, after PhD days, during department trips, and at Christmas parties.

I thank my husband, who inspires, challenges and motivates me every day. I thank my family for their unconditional support and their faith in me.

Abstract

Copper-zinc oxide based catalysts are applied industrially in methanol synthesis for more than 45 years in the low temperature process, commercially implemented by the ICI company. The growing use of methanol as a convenient energy storage molecule will require further improvement of the catalyst and adjustment to changing feedstock and process parameters. Many parameters of the catalyst preparation influence the activity to different degrees. The complex industrial recipe was developed from a combination of empirical trial and error methods. In order to understand the relationships of preparation, structure and function of the final catalyst, careful and systematic studies are necessary which include the realistic features of the active catalyst.

In this thesis different aspects were investigated: (i) the influence of the precursor structure, (ii) the role of the promoter and (iii) the influence of residual carbonates, known as high temperature cabonates (HT-CO_3) in the calcined catalyst. It was shown that neither zincian malachite (ZM) nor aurichalcite (AU) – both are mixed Cu-Zn hydroxy carbonate phases commonly used as precursors for Cu-Zn based catalysts – are *a priori* superior to the other. In the binary case, AU seems the better precursor, as it allows higher Zn/Cu ratios leading to smaller Cu-particles and more efficient ZnO spacers hindering Cu particle sintering, which is one of several reasons for catalyst deactivation. Upon promotion with small amounts of Al the situation changes drastically. For instance, the morphology of the promoted precursors is influenced such, that the BET surface area increases significantly. Most important, the deactivation of catalysts derived from both ZM and AU is much slower and sintering is no longer the primary deactivation mechanism. This leads to the situation, that ZM, with the higher Cu content, becomes now indeed superior to AU.

In addition, it was shown that the Al promoter has a significant effect on the ZnO support. Al^{3+} introduces additional defects into the ZnO, which lead to higher conductivity of the support. In a similar manner also Ga^{3+} acts as efficient promoter. Mg^{2+} on the other hand, leads to a strong decrease of defects, of the intrinsically n-doped ZnO, and consequently in a decreased conductivity. It turned out, that the conductivity of the support scaled with the activity of the copper impregnated support in reverse water-gas shift (rWGS) and methanol synthesis.

Another part of this work dealed with the role of the HT-CO_3, a fraction of the carbonate that only decomposes at temperatures $> 600\,\mathrm{K}$, and showed that its role is ambivalent. On the one hand, HT-CO_3 prevents the formation of large, crystalline CuO and ZnO particles during calcination. On the other hand, it leads to a dilution of the active copper-zinc component and thus leads to a decrease of the activity. Furthermore, it was shown that the amount of HT-CO_3 is linked to the number of oxygen vacancies in the ZnO support.

In summary, the results reported in this thesis show how the catalytic performance can be influenced by a careful tuning of synthesis parameters resulting in structural and electronic control of the active phase. This better understanding will enable the knowledge-based development of the catalyst for the requirements of future sustainable processes.

Zusammenfassung

Kupfer-Zinkoxid basierte Katalysatoren werden seit mehr als 45 Jahren im industriellen tieftemperatur ICI Prozess für die Herstellung von Methanol verwendet. Die zunehmende Verwendung von Methanol als Energiespeicher wird die weitere Verbesserung des Katalysators und seine Anpassung an veränderte Rohstoffe und Prozessparameter erfordern. Viele verschiedene Syntheseparameter beeinflusssen die Aktivität des Katalysators. Die komplexe, industriell entwickelte Rezeptur wurde mittels Versuch und Irrtum entwickelt. Um die Wechselwirkungen von Präparation, Struktur und Aktivität des Katalysators besser zu verstehen, sind weitere sorgfältige und systematische Studien notwendig, die die realen Eigenschaften des aktiven Katalysators untersuchen.

In der vorliegenden Dissertation wurden verschiedene Aspekte der Katalysatorpräparation untersucht: (i) der Einfluss der Präkursorstruktur, (ii) die Rolle des Promoters und (iii) der Einfluss von Hochtemperaturkarbonat (HT-CO_3) im kalizinierten Katalysator. Die Untersuchungen haben gezeigt, dass von den zwei Präkursorphasen Zinkmalachit (ZM) und Aurichalcit (AU) – beides gebräuchliche Hydroxykarbonate zur Herstellung von Kupfer-Zink-basierten Katalysatoren – keine *a priori* die bessere ist. Im binären Fall erwies sich AU als der bessere Katalysator. AU ermöglicht ein höheres Zn/Cu Verhältnis, welches zu kleineren CuO Partikeln und effizienteren ZnO Platzhaltern führt. Dadurch wird das Sintern von Kupferpartikeln verhindert, einer der Gründe für Katalysatordeaktivierung. Durch Promotierung mit kleinen Mengen von Aluminium ändert sich die Situation drastisch. Zum Beispiel wird die Morphologie der promotierten Präkursoren derart verändert, dass die BET Oberfläche stark vergrößert wird. Am allerwichtigsten jedoch ist, dass die Deaktivierung der promotierten Katalysatoren, von sowohl ZM als auch AU, signifikant verlangsamt wird. Das Sintern ist nicht mehr der vorrangige Deaktivierungsmechanismus. Das führt dazu, dass ZM, mit dem höheren Cu-Anteil, nun eine überlegene Aktivität in der Methanolsynthese zeigt.

Weiterhin wurde gezeigt, dass der Al Promoter den ZnO Träger signifikant beeinflusst. Al^{3+} führt zusätzliche Defekte in das ZnO ein, die zu einer erhöhten Leitfähigkeit des Trägers führen. Auf analoge Weise verhält sich auch Ga^{3+} als effizienter Promoter. Mg^{2+} auf der anderen Seite, führt zu einer Verringerung der Defekte im intrinisch n-leitenden ZnO. Das führt zu einer verringerten Leitfähigkeit. Es hat sich herausgestellt, dass die Leitfähigkeit des Trägermaterials mit der Aktiviät des mit Kupfer imprägnierten Trägers in der Methanolsynthese und in der reversen Wassergaskonvertierungsreaktion skaliert.

In einem weiteren Teil der Arbeit konnte gezeigt werden, dass die Rolle des HT-CO_3, ein Teil des Karbonats der Präkursorphase welcher erst bei Temperaturen $> 600\,\mathrm{K}$ zersetzt wird, ambivalent ist. Auf der einen Seite verhindert die Anwesenheit von HT-CO_3 die Bildung großer, kristalliner CuO und ZnO Partikel. Auf der anderen Seite führt es auch zu einer Verdünnung der aktiven Cu,Zn Komponente im Katalysator und damit zu einer Verringerung der Aktivität. Außerdem wurde gezeigt, dass die Menge an HT-CO_3 mit der Anzahl an Sauerstofffehlstellen im ZnO Träger korreliert.

Zusammengefasst zeigen die Ergebnisse dieser Arbeit, dass die katalytische Leistung als Ergebnis von struktureller und elektronischer Kontrolle über die aktive Phase, durch gewissenhaftes Einstellen der Syntheseparameter beeinflusst werden kann. Besseres Verständnis wird in Zukunft eine wissensbasierte Weiterentwicklung des Katalysators für nachhaltige Prozesse ermöglichen.

Contents

List of Figures

List of Tables

Abbreviations

AU	aurichalcite
BE	binding energy
BET	Brunauer Emmett Teller
GC	gas chromatography
GHSV	gas hourly space velocity
HAADF-STEM	high angle annular dark field- scanning transmission electron miscroscopy
HT-CO3	high temperature carbonate
ICI	Imperial Chemical Industries
MCPT	microwave cavity perturbation technique
MS	mass spectrometry
RFC	reactive frontal chromatography
rWGS	reverse water-gas-shift
SA	surface area
SEM	scanning electron microscopy
SMSI	strong metal support interaction
TA	transient adsorption
TCD	thermal conductivity detector
TEM	transmission electron miscroscopy
TPD	temperature programmed desorption
TPR	temperature programmed reduction
WGS	water-gas-shift

XRD	X-ray diffraction
XPS	X-ray photoelectron spectroscopy
ZM	zincian malachite

1 Introduction

1.1 Methanol

Methanol is a very important bulk chemical with a constantly growing relevance, which is pronounced in the immense growth of the annual methanol production. While in 1985 12.4 mio tons[1] were produced, in 2012 the production of methanol has already reached 60.6 million tons.[2]

The major part of methanol is used for formaldehyde production (see Figure 1.1). Next to that, synthesis of tert-Butylmethylether (MTBE) as a fuel additive to enhance antiknock properties of gasoline is an important utilization of methanol. Furthermore the direct usage as fuel, either pure or as a blend with gasoline becomes more and more important. For fuel cell applications methanol can either be used in the direct methanol fuel cell (DMFC), or it is steam reformed and the released hydrogen acts as the fuel in reformed methanol fuel cells (RMFC).[2]

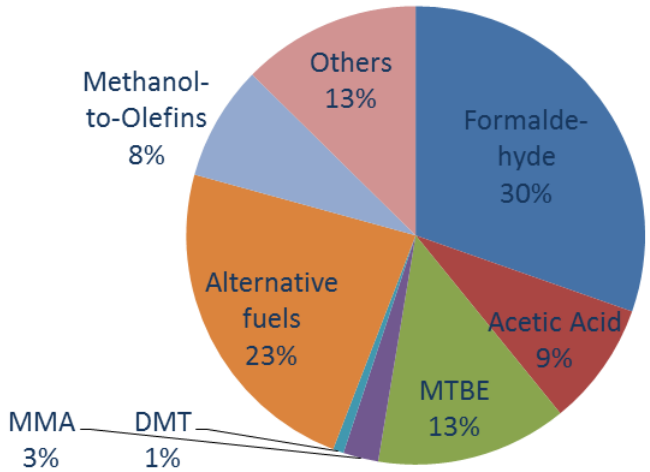

Figure 1.1: World consumption of methanol 2012[2]

The use of methanol in terms of an energy storage is of growing importance, since the fossil fuel resources are finite and alternatives have to be found. Methanol is a suitable candidate for a convenient engery storage molecule. It has a high energy density and is superior to hydrogen, in that it can be much better stored and transported as it is a liquid within a broad temperature range. Besides, it contains more hydrogen atoms per volume than liquid hydrogen itself. By methanol steam reforming, hydrogen can be generated for those applications where hydrogen is favourable, as e.g. in certain fuel cells.[2]

The reaction of hydrogen with carbon dioxide to yield methanol is highly promising as a system to store energy without net release of carbon dioxide. (In case hydrogen is produced from renewable energy sources.) When the energy is needed, methanol can be burned or steam reformed and the produced carbon dioxide can be recycled by again reacting with hydrogen to methanol. This way, the carbon dioxide emission could be greatly decreased and the impact on climate change diminished.

A reaction closely related to methanol synthesis from carbon dioxide and hydrogen is the reverse water-gas shift reaction. This reaction is an important part of the methanol synthesis reaction system, but it is also promising in terms of carbon dioxide recycling. Via formation of syngas it allows the production of valuable chemicals and at the same time it can reduce the dependency on fossil resources.

1.2 Methanol Synthesis

1.2.1 History

The first industrial process to prepare methanol from syngas (a mixture of CO and CO_2 in H_2) started in 1923 at BASF.[1,3,4] The first catalyst was made of ZnO/Cr_2O_3. It was not very active and thus required high reaction temperatures of 570 to 670 K. To shift the equilibrium at this high temperature towards methanol production, a very high pressure of 250 to 350 bar had to be used.

Copper-based catalysts were found to be much more active than ZnO-based catalysts, but also much easier poisoned by sulfur contaminations present in syngas made of coal. Only when naphta and natural gas sources were used for the formation of syngas in the mid 60s, copper based catalysts gained industial importance. Since that time industrial methanol synthesis has been performed via the so-called low pressure Imperial Chemical Industries (ICI) process. The ICI process is based on $Cu/ZnO/Al_2O_3$ catalysts and runs at 490-570 K (220-300°C) with pressures of 35-55 bar.[1,3,4]

$$CO + 2\,H_2 \rightleftharpoons CH_3OH \qquad \Delta H_{298K,50bar} = -91\,kJ\,mol^{-1} \qquad (1.1)$$

$$CO_2 + 3\,H_2 \rightleftharpoons CH_3OH + H_2O \qquad \Delta H_{298K,50bar} = -41\,kJ\,mol^{-1} \qquad (1.2)$$

Scheme 1.1: Methanol synthesis from syngas[3]

1.2.2 Carbon source of methanol

Whether the direct source of methanol over copper based catalyst is CO or CO_2, was a matter of debate over decades. In the beginning, CO was regarded as the source of methanol, probably because CO_2 had no effect on the first high pressure ZnO-Cr_2O_3 catalyst.[5] Only later it was found that small amounts of CO_2 act as a promoter for methanol synthesis over copper-zinc based catalysts.[5] Not until radioactive labelling studies were performed by Chinchen et al.[6] it was slowly established, that CO_2 is the source of methanol. The reason for the long scepticism probably lies in the poisoning effect of high water contents produced in CO_2-rich feed gases over Cu/ZnO based catalysts. Also to prevent scrambling of CO and CO_2 through water-gas-shift meaningful labelling studies needed differential conditions.[6,7] Additionally, there are also Cu-based, Zn-free catalysts, that are poisoned by CO_2 or rather by strongly bound formate adsorbates.[8,9] Due to these reasons it took a long time to agree on one carbon source and to unravel that apparently contradicting results actually derived from different testing conditions and catalysts. Furthermore the picture was complicated by theoretical calculations, which could not confirm that the mechanism using CO_2 hydrogenation was energenically favoured over CO hydrogenation until recently. Only when van der Waals forces were considered in the functional used for the DFT calculation, the difference between CO and CO_2 hydrogenation could be explained.[10]

1.2.3 Active sites and role of ZnO

Despite the fact that copper based catalysts have been used in methanol synthesis for more than 45 years, it was not clear what the exact mechanism and active sites for this reaction are, nor is there a uniform belief regarding the role of ZnO and other promoters, e.g. Al_2O_3.[3]

The nature of the active site was for a long time a matter of strong debate. Where some argue that metallic Cu^0 is the active site,[11,12] others make out Cu^+ dissolved in ZnO, stabilized by promoters as active sites.[13,14] It is also suggested that Cu^- at the

Schottky junction, the interface of Cu metal and ZnO, is the active site.[15,16] The Topsøe model[17,18] supports the idea of a strong metal support interaction (SMSI)[19,20]: Under reducing conditions Zn atoms migrate onto the copper surface. Behrens et al. report in a study which combines experimental evidence and theoretical prediction, that a steped, Zn decorated Cu surface are the active sites for the methanol synthesis from a CO_2 contaning feed.[7]

It is agreed upon that ZnO acts as a structural promoter. As a spacer ZnO particles inhibit the sintering of the copper particles and enhance copper dispersion.[21] Therefore the copper surface area is increased leading to a likewise increase of catalytic activity. However, as it was found out that the activity of Cu/ZnO catalysts is not linearly increasing with the copper surface area, ZnO also seems to play a role in the formation of active sites. Campbell et al.[22] claim that the ZnO support only helps to form thin copper islands with a highly active surface. By inducing strain a high Cu/ZnO interface area could lead to defect formation on the copper surface.[23,24] Alternatively it is also believed that Zn atoms migrate to the copper surface or even form a copper-zinc alloy (brass) under reaction conditions[17–20] (SMSI effect).

One reason that made it so difficult to compare activities and other characteristics of the catalysts and draw clear conclusion regarding active sites is the strong dependence of the catalysts on their precursors. This influence is often termed the chemical memory of the catalyst system. Besides, contradictions often arose again from the comparison of different conditions and catalyst systems.

1.3 Reverse water-gas shift reaction (rWGS)

1.3.1 General

One important reaction known to also take place during methanol synthesis is the reaction of carbon monoxide and water to carbon dioxide and hydrogen. This reaction is called the water-gas shift (WGS) reaction.

$$CO + H_2O \rightleftharpoons CO_2 + H_2 \qquad \Delta H_{298K,1bar} = -41\ kJ\,mol^{-1} \tag{1.3}$$

Scheme 1.2: Water-gas shift reaction[25]

The most important industrial applications of the WGS reaction are (i) adjustment of the CO_2/H_2 ratio and removal of CO in the effluent of steam reforming.[26,27] CO is the most potent poison mitigating the efficiency of fuel cells and can be removed by WGS reaction.[26,28] (ii) Hydrogen production for ammonia synthesis and other bulk chemicals[25] and (iii) detoxification of town gas.[27]

Application of the reverse water-gas shift (rWGS) reaction has only lately come into focus of research as a reaction which allows to recycle CO_2. Instead of being released as one of the most potent greenhouse gases and to further boost climate change, CO_2 is supposed as a feedstock for fuels and other valuable chemicals.[29] E.g. as part of the CAMERE process rWGS is used as the first step towards methanol synthesis from CO_2 and H_2.[30] The partition into two steps, allows the separation of H_2O after the first reaction, which is a strong inhibitor in methanol synthesis. Therefore the efficiency of the second step, the methanol synthesis from a $CO_2/CO,H_2$ mixed feed is improved. Before, the reverse WGS reaction has only been viewed as a side reaction in methanol synthesis, which at atmospheric pressure becomes the predominant observable reaction.

Currently three different classes of catalysts are investigated for WGS reaction.[29] The first class, copper based catalysts, are used in the low temperature region (up to 573 K). They are of similar composition as catalysts for methanol synthesis: Cu/ZnO catalysts with different possible promoters such as e.g. the oxides of Al, Zr and Si to improve stability or dispersion of copper particles.

For high temperatures (>670 K) a group of iron based catalysts is used for forward WGS (not suited for reverse WGS). A third group are cerium based catalysts, often in conjuction with precious metals, e.g. Pt/CeO_2 at medium high temperatures.[29]

1.3.2 Active sites

The rWGS reaction on copper catalysts was found to be structure sensitive. Different activities for different copper single crystal surface planes were found in studies with model catalysts as well as in theoretical DFT studies.[22,31,32] Cu(110) is an open plane with the coordinatively most unsaturated copper atoms of all low index surface planes and was found to be the most active of those surface planes for rWGS.[22,32]

Due to the similarities of activation energy on model Cu catalysts and high surface area catalysts, it was supposed that metallic copper is the active site.[33] Contrary to findings in methanol synthesis, most studies did not find evidence for a promotional effect of ZnO for Cu catalysts in the WGS reaction, neither on model catalysts[31,34] nor on high surface area

catalysts.[35] But Rodriguez et al.[36,37] reported that they observed an enhancement of the rWGS reaction rate using copper deposited on ZnO($000\bar{1}$) by about factor 50 as compared to Cu(111). A recent theoretical study by Studt et al.[38] showed that a stepped Cu(211) surface and zinc decorated copper steps are equally active for the WGS. This controversy shows that the question of the active site is not fully answered yet and it cannot be excluded that a SMSI plays a beneficial role in the rWGS reaction.

1.3.3 Mechanisms

For the forward and reverse WGS reaction over copper containing catalysts, three different mechanisms are currently debated. There is the surface redox mechanism[27,33,39]: metallic copper on the surface of the catalyst is first oxidized and later reduced during the catalytic cycle (see Scheme 1.3). The rate determining step of this reaction is the dissociation of CO_2 (eq.(1.4)).[27]

$$CO_2 + 2\,^* \rightleftharpoons CO^* + O^* \tag{1.4}$$

$$CO^* \rightleftharpoons CO + {}^* \tag{1.5}$$

$$H_2 + 2\,^* \rightleftharpoons 2\,H^* \tag{1.6}$$

$$2\,H^* + O^* \rightleftharpoons H_2O^* + 2\,^* \tag{1.7}$$

$$H_2O^* \rightleftharpoons H_2O + {}^* \tag{1.8}$$

Scheme 1.3: Surface redox mechanism for the rWGS reaction[27], * - symbol for free adsorption site

Most investigations have found high surface coverages with formate.[34,40–42] Some groups assumed therefore that formate has to be some kind of intermediate.[22,34] Recent DFT studies on Cu(111) as well as stepped Cu(211) and Zn decorated Cu stepped surfaces showed that most likely the WGS reaction proceeds via a carboxyl intermediate.[38,43] A mikrokinetic study by Madon et al.[42] resulted, too, in a model where carboxyl is an intermediate of the reaction (see Scheme 1.4), but formate is only a spectator species. Here the carboxyl decomposition (eq.(1.14)) is proposed as the rate determining step for the rWGS.[43]

$$\mathrm{CO} + {}^* \rightleftharpoons \mathrm{CO}^* \tag{1.9}$$

$$2\,\mathrm{H}^* \rightleftharpoons \mathrm{H_2} + 2\,{}^* \tag{1.10}$$

$$\mathrm{H_2O} + {}^* \rightleftharpoons \mathrm{H_2O}^* \tag{1.11}$$

$$\mathrm{CO_2^*} \rightleftharpoons \mathrm{CO_2} + {}^* \tag{1.12}$$

$$2\,\mathrm{H_2O}^* + 2\,{}^* \rightleftharpoons 2\,\mathrm{H}^* + 2\,\mathrm{OH}^* \tag{1.13}$$

$$\mathrm{CO}^* + \mathrm{OH}^* \rightleftharpoons \mathrm{COOH^*_{cis}} + {}^* \tag{1.14}$$

$$\mathrm{COOH^*_{trans}} + \mathrm{OH}^* \rightleftharpoons \mathrm{CO_2^*} + \mathrm{H_2O}^* \tag{1.15}$$

$$\mathrm{COOH^*_{cis}} \rightleftharpoons \mathrm{COOH^*_{trans}} \tag{1.16}$$

Scheme 1.4: 8 Step mechanism via carboxyl intermediate for low temperature WGS reaction[42]

1.4 Catalyst preparation

Copper based catalysts have been used for more than 40 years in methanol synthesis and WGS reaction. Many different copper systems and preparation routes have been investigated. The catalyst commonly used in industrial applications comprises zinc and aluminium next to copper with an approximate ratio of Cu:Zn:Al 60:30:10.[44] The most relevant route for the preparation of highly active catalysts is coprecipitation of the metal nitrates (copper, zinc, aluminium nitrates) with sodium carbonate in a way that the pH of the slurry remains constant.[45] This is done by adding metal and carbonate solution simultaneously to a seperate reactor vessel (Figure 1.2). For the ternary system optimum preparation conditions were found at a reaction temperature of 338 K and nearly neutral pH (6.5).[46,47] As important as the precipitation itself is the ageing of the catalyst precursor in the mother liquor for 30 - 120 min.[45,48,49] After the ageing period, the precipitate is filtrated, washed several times to remove residual $NaNO_3$, and spraydried. Afterwards the catalyst precurser is calcined at mild temperatures between 600-700 K.[45] To obtain the active catalyst, CuO needs to be reduced to metallic Cu. This is usually done in situ in the catalysis reactor.

Various precursor preparation parameters, especially of the early stages of precipitation and ageing, as e.g. pH, temperature, ageing time next to the chemical composition were found to strongly influence the properties of the final catalyst.[47,48] The conditions

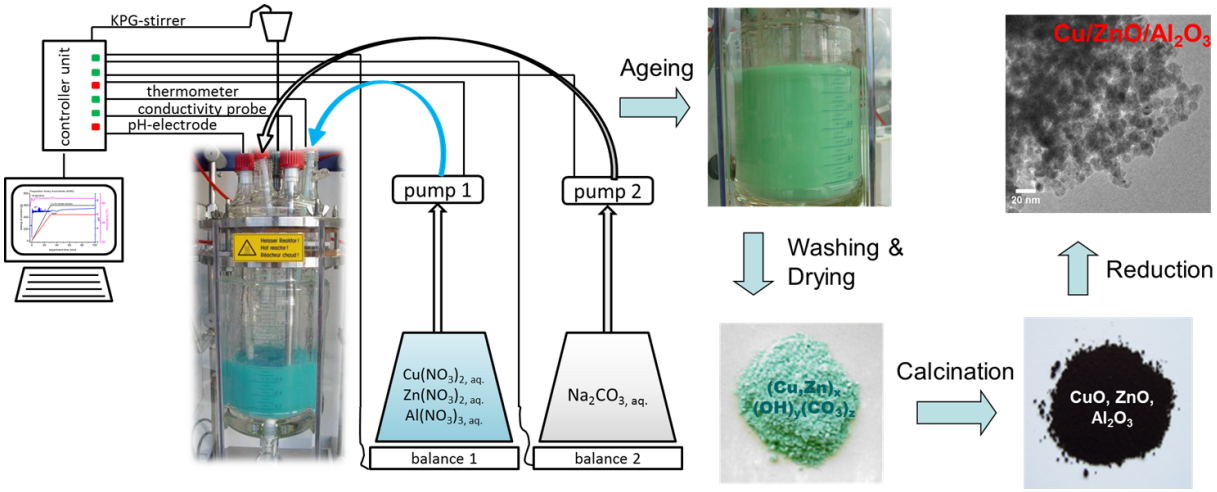

Figure 1.2: Schematic picture of the precipitation setup (left) and subsequent steps of the catalyst preparation (right). Adopted from[44,48].

determined to yield the best catalyst can be reasoned in terms of leading to the best interdispersion of copper and zinc atoms and a favourable microstructure in the solid precursor.[50]

The Cu/Zn-ratio determines the major precursor phase, which is formed after coprecipitation and ageing. At high fractions of copper (down to 73 % Cu), zincian malachite (ZM) is formed, while at lower copper content aurichalcite (AU) is begining to form. At ratios of about 1 aurichalcite is the main phase, whereas hydrozincite is formed as zinc-rich byphase at higher zinc content (see Table 1.1).[48,51] The presence of ternary promoters influences the phase diagram again, such that low amounts of Al^{3+} lead to an increased incorporation limit of Zn into the ZM phase and the formation of zinc-rich aurichalcite can be lessened.[52] Higher amounts of Al^{3+} lead to the formation of a hydrotalcite-like phase.[52] Although different opinions exist about the question whether zincian malachite or aurichalcite is the better precursor structure yielding the more active catalysts,[20,50,53] and it seems no phase is *a priori* the superior precursor, it is evident, that the formation of multiple phases is undesired as the enrichment of one element in a side phase prevents the homogeneous element distribution in the solid.[50]

The mode of precipitation, i.e. constant, decreasing or increasing pH also works on the phase formation.[44,48] When starting from a basic pH, i.e. in the decreasing pH precipitation, where the metal solution is slowly added to the base, hydroxide rich aurichalcite formation is favoured.[48] Increasing pH mode would be even worse, because it would lead to subsequent precipitation of first Cu and secondly Zn species, and no homogeneous metal

Table 1.1: Possible binary precursor phases[48,51]

precursor phase	formula	copper content
malachite	$Cu_2(OH)_2CO_3$	100 %
zincian malachite	$(Cu,Zn)_2(OH)_2CO_3$	73-100 %
aurichalcite	$(Zn,Cu)_5(OH)_6(CO_3)_2$	ca. 10-50 %
hydrozincite	$Zn_5(OH)_6(CO_3)_2$	ca. 0-10 %

distribution in the precipitate would be reached. A constant pH is best, as it ensures constant precipitation conditions throughout the coprecipitation process and prevents segregation of the elements.[44,48]

The pH value needs to be just high enough to ensure complete precipitation, and should not be too high to inhibit oxalation of Cu and formation of additional precursor phases.[44] If the pH is too low, the Zn component could be incompletely precipitated or leached from the solid precipitate during ageing.[49] Thus the optimal pH value was determined as 6.5.

The temperature mainly influences the kinetics of the precipitation and ageing process.[46] Elevated temperatures accelerate the recrystallization, but also reduce the precipitation pH of Zn by one unit.[49] Accordingly, lower temperatures during aging were found to lead to leaching of the Zn component. Too high temperatures should also be avoided to prevent the formation of large crystallites.[49] Thus the optimal temperature was found around 338 K.

All of the afore mentioned optimal conditions during the precipitation process will not yield highly active catalysts, if the ageing is not done right. This is the essential step during which the initially amorphous precipitate is restructuring and forming a crystalline solid.[48,49] This process is accompanied by a colour change and so-called pH-drop. It is agreed upon, that the amorphous precipitate is transformed by continuing partial dissolution/re-precipitation processes.[48] Georgeite is the amorphous phase with the same anionic composition as zincian malachite and the mineral rosasite and therefore assumed to be the direct precursor for ZM. Depending on the precipitation conditions also other amorphous phases, e.g. hydroxy-rich carbonates might be formed and restructure to georgeite or lead to the formation of other crystalline phases as aurichalcite. Once the nuclei of crystalline phases, e.g. ZM or AU, are formed the final crystallization of the hydroxycarbonate proceeds rapidly.[48]. Zander et al.[49] discovered the intermediate formation of a zinc rich storage phase ($Na_2Zn_3(CO_3)_4$) at higher pH values, which quickly disappeared again upon incorporation of the Zn into the mixed Cu,Zn hydroxycarbonate.

Mild calcination conditions are applied such that the hydroxy carbonate decomposes to nano-crystalline mixed CuO/ZnO, but the oxide still contains some undecomposed carbonate, the so-called high-temperature carbonate (HT-CO_3).[48,53] Higher temperatures are supposed to lead to sintering of the catalyst, destruction of the porosity, and loss of copper surface area.[50]

1.5 Selected methods

For the comparison of differently prepared catalysts and deeper insight into structure-function relationships the Cu-surface area (SA) is an important property. Different methods have been developed for its determination. Two methods, N_2O-reactive frontal chromatography (RFC) and H_2-transient adsorption, are briefly discussed in the following two subsections.

The third method presented is used to obtain insights into the changes of the electronic structure of semiconductor materials under working conditions.

1.5.1 N_2O-reactive frontal chromatography (RFC)

Cu-SA of the reduced catalysts were conveniently measured by nitrous oxide (N_2O) chemisorption using the Reactive Frontal Chromatography (RFC) method since Chinchen et al. introduced that method in 1987.[54] This method is based on the assumption, that the reaction of N_2O with a Cu surface proceeds quantitatively according to $N_2O + 2\,Cu \longrightarrow N_2 + Cu_2O$ resulting in half a monolayer coverage with oxygen. This is possible because the activation barrier of this reaction is very low with 0 - 8 $kJ\,mol^{-1}$. Hence the lineshapes are very sharp, with a rectangular shape as can be seen exemplarily in Figure 1.3. The N_2O capacity of the samples can then easily be calculated by quantifying the amount of released N_2. Using the average density of Cu-atoms per surface area ($1.47 \cdot 10^{19}$ atoms per m^2), the metal Cu-SA used to be calculated. Recent results revealed, that N_2O not only reacts with the Cu surface atoms, but also reacts with partially reduced ZnO_x species in conventional Cu/ZnO-based catalysts[55,56] and catalysts, where the ZnO component was introduced in a subsequent impregnation step.[56] Therefore, the Cu-SA is overestimated in samples containing ZnO. Exposed Cu^0 and partially reduced ZnO_x surfaces of a pre-reduced Cu/ZnO catalyst were oxidized by switching the feed from an inert He stream to a reactive N_2O/He mixture.

Within certain so-called catalyst families, i.e. catalysts with a similar preparation history, the number of probed surface sites was found proportional to the activity in methanol synthesis.[57] However, no universal relationship between N_2O-sites and activity was found.

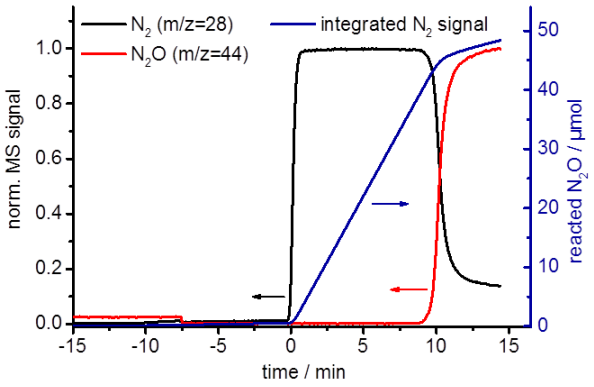

Figure 1.3: N_2O-RFC experiment over a $Cu/ZnO/Al_2O_3$ catalyst

1.5.2 H_2-transient adsorption (TA)

The principle of H_2-TA derives from the observed autocatalytic reduction of a Cu_2O covered Cu surface.[58,59] After an initially very slow reduction of a surface layer Cu_2O on Cu, the rate accelerates after the induction period, as observed in a surface study with STM and XPS.[58] Also for a bulk catalyst, it was shown by means of H_2-temperature programmed adsorption experiments, that a reduction of a N_2O oxidized Cu surface is possible close to room temperature.[59] Kuld et al. showed only recently that by H_2-TA complementary information to that obtained by N_2O-RFC can be gained.[55] For the measurement, H_2 isothermal adsorption profiles after switching from an inert gas feed to a H_2-containg one are recorded of a Cu sample in 3 different states: firstly in the "as is" state (fully oxidized), secondly after reduction of the Cu component, and thirdly after an N_2O-RFC measurement, when the surface is oxidized to Cu_2O. The profiles reveal that the oxidized catalyst interacts least with the H_2 from the feed (see Figure 1.4). After reduction, the equilibrium concentration of H_2 in the feed is only reached slightly later compared to the oxidized state. That indicates a stronger interaction of H_2 with the reduced catalyst, which can be either metal Cu or partially reduced ZnO_x. As one of few metals, Cu exhibits a significant activation barrier for H_2 adsorption, due to the deep lying d bands of metallic

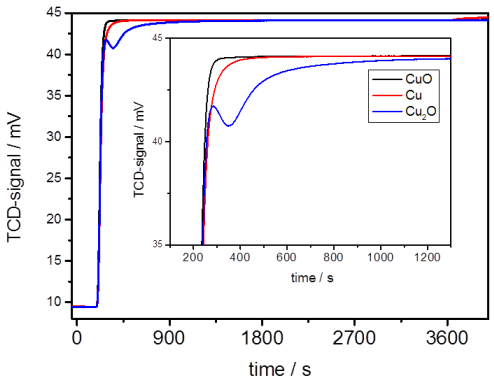

Figure 1.4: H_2-TA experiment over a $Cu/ZnO/Al_2O_3$ catalyst. t=0 indicates point of switching from an inert gas feed to a 5% H_2 containing feed.

copper.[60,61] On the low-index faces Cu(1 0 0), (1 1 0) and (1 1 1) no adsorption of molecular hydrogen was observed at room temperature. Only on the higher-index faces (2 1 1), (3 1 1) and (7 5 5) dissoziative H_2 adsorption was confirmed.[61] This demonstrates the necessity of surface defects, as steps or edges for a successful H_2 chemisorption. According to Kuld et al.[55] the equilibrium coverage of H_2 on a free Cu surface is $\theta_H = 0.04$ monolayers, for a H_2 concentration of 1 % at room temperature calculated by applying the single Langemuirian model. These low coverages indicate that surface defects must play a dominant role as adsorptions sites for hydrogen.

The profile of the transient adsorption after oxidation of the surface with N_2O seems for the first 300 s after switching from inert gas very similar to the reduced state profile, but then suddenly the H_2-concentration decreases again indicating a process where H_2 is consumed. This observation agrees well with the preveously observed autocatalytic reduction of a Cu_2O layer on Cu. Thus this additional H_2-consumption is attributed to the reduction of Cu_2O to Cu^0. Kuld et al. report that there is a systematic difference between the Cu-SA determined by H_2-TA and H_2-TPD, which is performed under harsh conditions at elevated hydrogen pressure and slightly reduced temperature.[55] This can be explained by the controversial assumption of a 4:1 Cu:H_2 stoichiometry for the H_2-TPD, as determined from single crystal studies on different low index planes.[62,63] Fichtl et al.[56] reported recently, that a 3:1 stoichiometry for the adsorption of H_2 on copper catalysts during H_2-TPD is in much better agreement with N_2O-RFC measurements of zinc free copper systems.[56] These controversies illustrate that it is not entirely understood what kind of sites are measured with these methods. In fact it becomes apparent, that none of

the presented methods can measure the active site for methanol synthesis as such. The different values that can be determined might be proportional to the activity within certain boundaries, but do not resemble the active sites. Additionally it must be stated, that the catalyst surface is highly dynamic and also changes with changing reaction conditions during methanol synthesis.[18,19,64]

1.5.3 Microwave-cavity perturbation technique (MCPT)

In order to better understand electronic structure-function relationships electrical conductivity and complex permittivity measurements can be performed.[65] Conductivity changes of catalysts under operating conditions are of great interest, as they can give insight into the adsorbate-surface interaction and tell whether the free charge carrier density in the conduction or valence band is influenced by reactive gases.

In heterogeneous catalysis conductivity measurements used to be performed by contacting the catalyst powder or pressed pellets with two metal electrodes as it is done for sensing materials.[66] Improved methods nowadays already use 4-contact measurements. The disadvantage of this method remains that the measured conductivities strongly depend on the quality of the contacts and additionally the grain boundaries lead to contact resistances. Problems arise additionally from possible incorporation of metal impurities from the electrodes into the studied sample and from electrode polarization.

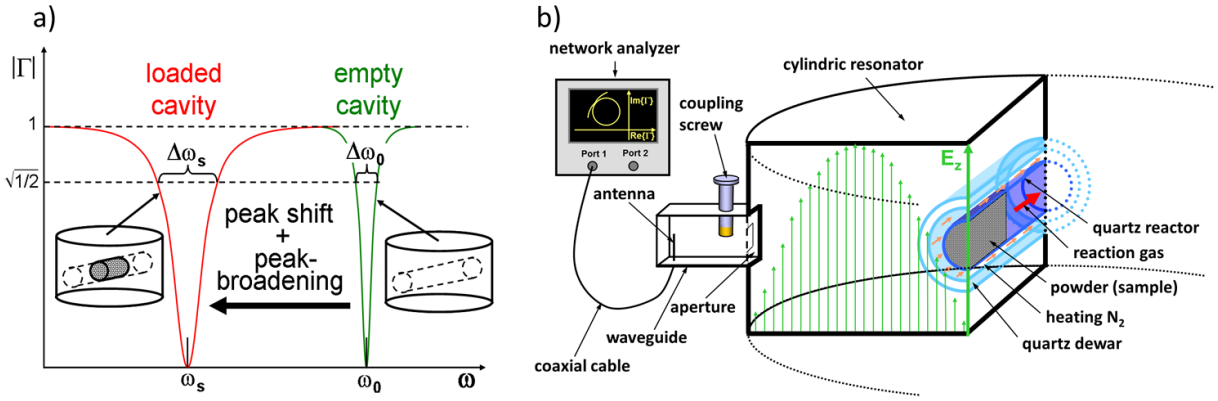

Figure 1.5: a) Measurement principle of MCPT. Shown is the reflection factor Γ versus frequency ω for critical coupling with and without sample. Adapted from[67]
b) Schematic presentation of the MCPT setup for measuring permittivities and conductivities of catalysts under in situ conditions. Adapted from[68].

Therefore the MCPT, a contact-free method, was introduced into the field of catalysis in order to study the (di)electric properties of powder catalysts under *in situ* conditions. It was already successfully applied for the investigation of vanadium-phosphorous-oxides [67] and a $MoVTeNbO_x$ catalyst (M1) [69] in selective oxidation reactions of different hydrocarbons. Only if the measurements are performed *in situ*, true correlations between conductivity and catalytic activity and selectivity can be deduced. By working contact free all problems with contact resistances and electrode problems can be avoided.

MCPT works by placing a catalyst powder inside a microwave cavity. The shift of the resonance frequency (ω_i) and broadening of the resonance signal expressed as the change of the quality factor $Q_i = \frac{\omega_i}{\Delta\omega_i}$ upon introducing the sample into the cavity (see Figure 1.5a), can be related to the complex permittivity $\varepsilon = \varepsilon_1 - i\varepsilon_2$ of the sample. If the penetration depth of the microwave field into the sample is much larger than the sample dimensions, the following approximations are valid:

$$\frac{\omega_0 - \omega_s}{\omega_0} = A(\varepsilon_1 - 1)\frac{V_s}{V_c} \tag{1.17}$$

$$\frac{1}{Q_s} - \frac{1}{Q_0} = 2B\varepsilon_2\frac{V_s}{V_c}, \text{with } Q_i = \frac{\omega_i}{\Delta\omega} \tag{1.18}$$

where A and B are constants, depending on the geometry of the cavity and sample and on the resonance mode, and V_s and V_c are the volume of the sample and the cavity, respectively. For insulators and poorly conducting samples as semiconductors, the above mentioned equations are valid. However for metallic conducting samples the penetration depth of the microwave field into the sample is much smaller, so that equations 1.17 and 1.18 may not be valid anymore and the skin depth regime needs to be accounted for. [70] The imaginary part of the permittivity ε_2 is directly related to the electrical conductivity, in the case of dry, semiconducting samples.

$$\sigma = \omega \cdot \varepsilon_0 \cdot \varepsilon_2 \tag{1.19}$$

It has been shown feasible to use a cylindrical X-band TM_{110} silver plated brass cavity with a height of 19.5 mm and a diameter of 38.5 mm as resonator, which operates at a frequency of 9.2 GHz. The catalyst bed is placed in a plug-flow quartz reactor, which is surrounded by a double walled quartz dewar mantle, in the middle of the cavity, parallel to the endplates. In between the inner quartz reactor and the evacuated dewar mantle a preheated N_2 flow is responsible for heating the reactor, reactor gases and the catalyst bed.

The dewar mantle shields the reactor from the resonator and thus prevents heat losses and irradiation of the resonator walls. Additionally the cavity endplates are cooled with two Peltier elements. A network analyzer is used to generate the mirowaves and record the resonance signal. The electromagnetic waves are coupled via a waveguide to the resonator. A schematic representation of the setup is shown in Figure 1.5b.

1.6 Aim and outline of this work

Despite their successful application in industry for nearly 50 years, still several aspects of the preparation of Cu/Zn-based catalysts for methanol synthesis remain ill understood. The question of the role of high-temperature carbonate (HT-CO_3) was not resolved so far. It was observed, that precursors with a high HT-CO_3 content show superior activity.[71,72] However, a detailed study about the role of the HT-CO_3 in the calcined precatalyst was lacking. The role of the Al promoter, a vital component of industrial copper based catalysts for methanol synthesis, was also lacking some fundamental understanding. Controversies also existed about the optimal precursor phase.[20,50] These realistic features deriving from the preparation history of the active catalyst system are often neglected in model studies and needed further systematic investigation provided in this thesis.

The starting point of this work was the preparation, characterization and testing in rWGS of a series of binary Cu/ZnO catalysts derived from either zincian malachite or aurichalcite precursors, depending on the Cu/Zn ratio. These results are presented in chapter 2. In chapter 3, two representative phase pure samples were selected for the further in depth investigation of the influence of the calcination conditions, in this case the heating ramp.

As the industrial relevant methanol catalyst usually contains Al as a promoter, and previous results[52] suggested, that with already 3 % Al an optimal promotion was successfully achieved, further studies were performed to investigate the origin of the beneficial modification through Al. The influence of a small amount of Al promotion on the two precursor systems ZM and AU was investigated as well as the resulting catalysts in chapter 4. Furthermore the impact of calcination conditions on those Al promoted catalysts was studied in chapter 4. Chapter 5 presents detailed characterization of a reference catalyst, prepared in a 100 g scale. This chapter is adapted from the publication: 'Synthesis and Characterisation of a Cu/ZnO based catalyst' by Julia Schumann, Thomas Lunkenbein, Andrey

Tarasov, Nygil Thomas, Robert Schlögl and Malte Behrens; ChemCatChem, 6(10), pages 2889-2897, October 2014.

In chapter 6, a model type study is presented, in which the influence of 3 % promoter on the ZnO support is investigated. For a better insight different promoters were studied, apart from Al^{3+}, also Ga^{3+} and Mg^{2+} were compared with the unpromoted ZnO. After investigating the bare support, also the ZnO:M samples impregnated with 10 % Cu were studied and tested in rWGS and methanol synthesis.

In chapter 7 a summary of the results is given.

1.7 References

[1] G. Chinchen, P. Denny, J. Jennings, M. Spencer, K. Waugh, *Appl. Catal.* **1988**, *36*, 1.

[2] Source: http://www.methanol.org/methanol-basics/the-methanol-industry.aspx, checked 21/06/2011.

[3] J. B. Hansen, P. E. H. Nielsen, *Handbook of Heterogeneous Catalysis*, chapter Methanol Synthesis, Wiley-VCH, Weinheim, 2nd Edition, **2008**, pp. 2920–2944.

[4] K.-O. Hinrichsen, J. Strunk, *Nachr. Chem.* **2006**, *54*, 1080.

[5] K. Klier, in D. Eley, H. Pines, P. B. Weisz, Eds., *Adv. Catal.*, Vol. 31, Academic Press, **1982**, pp. 243–313.

[6] G. Chinchen, P. Denny, D. Parker, M. Spencer, D. Whan, *Appl. Catal.* **1987**, *30*, 333.

[7] M. Behrens, F. Studt, I. Kasatkin, S. Kühl, M. Hävecker, F. Abild-Pedersen, S. Zander, F. Girgsdies, P. Kurr, B. L. Kniep, M. Tovar, R. W. Fischer, J. K. Nørskov, R. Schlögl, *Science* **2012**, *336*, 893.

[8] S. Zander, E. L. Kunkes, M. E. Schuster, J. Schumann, G. Weinberg, D. Teschner, N. Jacobsen, R. Schlögl, M. Behrens, *Angew. Chem. Int. Ed.* **2013**, *52*, 6536.

[9] F. Studt, M. Behrens, E. L. Kunkes, N. Thomas, S. Zander, A. Tarasov, J. Schumann, E. Frei, J. B. Varley, F. Abild-Pedersen, J. K. Nørskov, R. Schlögl, The mechanism of CO and CO_2 hydrogenation to methanol over cu based catalysts, **2014**, unpublished results.

[10] F. Studt, F. Abild-Pedersen, J. B. Varley, J. K. Norskov, *Catal. Lett.* **2013**, *143*, 71.

[11] G. Chinchen, K. Waugh, D. Whan, *Appl. Catal.* **1986**, *25*, 101.

[12] P. B. Rasmussen, P. M. Holmblad, T. Askgaard, C. V. Ovesen, P. Stoltze, J. K. Nørskov, I. Chorkendorff, *Catal. Lett.* **1994**, *26*, 373.

[13] V. Ponec, *Surf. Sci.* **1992**, *272*, 111.

[14] T. M. Yurieva, L. M. Plyasova, T. A. Kriger, V. I. Zaikovskii, O. V. Makarova, T. P. Minyukova, *React. Kinet. Catal. Lett.* **1993**, *51*, 495.

[15] J. C. Frost, *Nature* **1988**, *334*, 577.

[16] F. Liao, Y. Huang, J. Ge, W. Zheng, K. Tedsree, P. Collier, X. Hong, S. C. Tsang, *Angew. Chem. Int. Ed.* **2011**, *50*, 2162.

[17] N.-Y. Topsøe, H. Topsøe, *Top. Catal.* **1999**, *8*, 267.

[18] J.-D. Grunwaldt, A. Molenbroek, N.-Y. Topsøe, H. Topsøe, B. Clausen, *J. Catal.* **2000**, *194*, 452.

[19] R. Naumann d'Alnoncourt, X. Xia, J. Strunk, E. Löffler, O. Hinrichsen, M. Muhler, *Phys. Chem. Chem. Phys.* **2006**, *8*, 1525.

[20] T. Fujitani, J. Nakamura, *Catal. Lett.* **1998**, *56*, 119.

[21] M. S. Spencer, *Top. Catal.* **1999**, *8*, 259.

[22] J. Yoshihara, C. T. Campbell, *J. Catal.* **1996**, *161*, 776.

[23] M. Günter, T. Ressler, B. Bems, C. Büscher, T. Genger, O. Hinrichsen, M. Muhler, R. Schlögl, *Catal. Lett.* **2001**, *71*, 37.

[24] I. Kasatkin, P. Kurr, B. Kniep, A. Trunschke, R. Schlögl, *Angew. Chem.* **2007**, *119*, 7465.

[25] K.-O. Hinrichsen, K. Kochloefl, M. Muhler, *Handbook of Heterogeneous Catalysis*, chapter Water Gas Shift and COS Removal, Wiley-VCH, Weinheim, **2008**, pp. 2905–2920.

[26] H. Purnama, T. Ressler, R. E. Jentoft, H. Soerijanto, R. Schlögl, R. Schomäcker, *Appl. Catal., A* **2004**, *259*, 83.

[27] M. Ginés, A. Marchi, C. Apesteguía, *Appl. Catal., A* **1997**, *154*, 155.

[28] Y. Tanaka, T. Utaka, R. Kikuchi, K. Sasaki, K. Eguchi, *Appl. Catal., A* **2003**, *242*, 287.

[29] G. Centi, S. Perathoner, *Catal. Today* **2009**, *148*, 191.

[30] O.-S. Joo, K.-D. Jung, I. Moon, A. Y. Rozovskii, G. I. Lin, S.-H. Han, S.-J. Uhm, *Ind. Eng. Chem. Res.* **1999**, *38*, 1808.

[31] I. Nakamura, T. Fujitani, T. Uchijima, J. Nakamura, *Surf. Sci.* **1998**, *400*, 387.

[32] G.-C. Wang, L. Jiang, X.-Y. Pang, Z.-S. Cai, Y.-M. Pan, X.-Z. Zhao, Y. Morikawa, J. Nakamura, *Surf. Sci.* **2003**, *543*, 118.

[33] C. T. Campbell, K.-H. Ernst, *Surface Science of Catalysis*, chapter 8: Forward and Reverse Water-Gas ShiftReactions on Model Copper Catalysts - Kinetics and Elementary Steps, ACS Symposium Series, American Chemical Society, **1992**.

[34] T. Fujitani, I. Nakamura, T. Uchijima, J. Nakamura, *Surf. Sci.* **1997**, *383*, 285.

[35] F. S. Stone, D. Waller, *Top. Catal.* **2003**, *22*, 305.

[36] J. A. Rodriguez, P. Liu, J. Hrbek, J. Evans, M. Pérez, *Angew. Chem. Int. Ed.* **2007**, *46*, 1329.

[37] Y. Yang, J. Evans, J. A. Rodriguez, M. G. White, P. Liu, *Phys. Chem. Chem. Phys.* **2010**, *12*, 9909.

[38] F. Studt, M. Behrens, F. Abild-Pedersen, *Catal. Lett.* **2014**, *144*, 1973.

[39] G.-C. Wang, J. Nakamura, *J. Phys. Chem. Lett.* **2010**, *1*, 3053.

[40] S. Fujita, M. Usui, N. Takezawa, *J. Catal.* **1992**, *134*, 220.

[41] J. Yoshihara, S. C. Parker, A. Schafer, C. T. Campbell, *Catal. Lett.* **1995**, *31*, 313.

[42] R. J. Madon, D. Braden, S. Kandoi, P. Nagel, M. Mavrikakis, J. A. Dumesic, *J. Catal.* **2011**, *281*, 1.

[43] A. A. Gokhale, J. A. Dumesic, M. Mavrikakis, *J. Am. Chem. Soc.* **2008**, *130*, 1402.

[44] M. Behrens, D. Brennecke, F. Girgsdies, S. Kißner, A. Trunschke, N. Nasrudin, S. Zakaria, N. F. Idris, S. B. A. Hamid, B. Kniep, R. Fischer, W. Busser, M. Muhler, R. Schlögl, *Appl. Catal., A* **2011**, *392*, 93.

[45] M. Behrens, R. Schlögl, *Z. anorg. allg. Chem.* **2013**, 2683.

[46] J.-L. Li, T. Inui, *Appl. Catal., A* **1996**, *137*, 105.

[47] C. Baltes, S. Vukojevic, F. Schüth, *J. Catal.* **2008**, *258*, 334.

[48] B. Bems, M. Schur, A. Dassenoy, H. Junkes, D. Herein, R. Schlögl, *Chem. Eur. J.* **2003**, *9*, 2039.

[49] S. Zander, B. Seidlhofer, M. Behrens, *Dalton Trans.* **2012**, *41*, 13413.

[50] M. Behrens, *J. Catal.* **2009**, *267*, 24.

[51] M. Behrens, F. Girgsdies, *Z. anorg. allg. Chem.* **2010**, *636*, 919.

[52] M. Behrens, S. Zander, P. Kurr, N. Jacobsen, J. Senker, G. Koch, T. Ressler, R. W. Fischer, R. Schlögl, *J. Am. Chem. Soc.* **2013**, *135*, 6061.

[53] G. J. Millar, I. H. Holm, P. J. R. Uwins, J. Drennan, *J. Chem. Soc., Faraday Trans.* **1998**, *94*, 593.

[54] G. Chinchen, C. Hay, H. Vandervell, K. Waugh, *J. Catal.* **1987**, *103*, 79.

[55] S. Kuld, C. Conradsen, P. G. Moses, I. Chorkendorff, J. Sehested, *Angew. Chem. Int. Ed.* **2014**, *53*, 5941.

[56] M. B. Fichtl, J. Schumann, I. Kasatkin, N. Jacobsen, M. Behrens, R. Schlögl, M. Muhler, O. Hinrichsen, *Angew. Chem. Int. Ed.* **2014**, *53*, 7043.

[57] M. Kurtz, N. Bauer, C. Büscher, H. Wilmer, O. Hinrichsen, R. Becker, S. Rabe, K. Merz, M. Driess, R. Fischer, M. Muhler, *Catal. Lett.* **2004**, *92*, 49.

[58] F. Yang, Y. Choi, P. Liu, J. Hrbek, J. A. Rodriguez, *J. Phys. Chem. C* **2010**, *114*, 17042.

[59] O. Hinrichsen, T. Genger, M. Muhler, in S. M. Avelino Corma, Francisco V. Melo, J. L. G. Fierro, Eds., *12th International Congress on Catalysis Proceedings of the 12th ICC*, Vol. Volume 130, Elsevier, **2000**, pp. 3825–3830.

[60] K. Christmann, *Molecular Physics* **1989**, *66*, 1.

[61] K. Christmann, *Surface Science Reports* **1988**, *9*, 1.

[62] M. Muhler, L. P. Nielsen, E. Tornqvist, B. S. Clausen, H. Topsoe, *Catal. Lett.* **1992**, *14*, 241.

[63] G. Anger, A. Winkler, K. Rendulic, *Surface Science* **1989**, *220*, 1.

[64] O. Martin, J. Perez-Ramirez, *Catal. Sci. Technol.* **2013**, *3*, 3343.

[65] M. Eichelbaum, R. Stoßer, A. Karpov, C.-K. Dobner, F. Rosowski, A. Trunschke, R. Schlogl, *Phys. Chem. Chem. Phys.* **2012**, *14*, 1302.

[66] S. Sänze, A. Gurlo, C. Hess, *Angew. Chem. Int. Ed.* **2013**, *52*, 3607.

[67] M. Eichelbaum, M. Hävecker, C. Heine, A. Karpov, C. K. Dobner, F. Rosowski, A. Trunschke, R. Schlögl, *Angew. Chem. Int. Ed.* **2012**, *51*, 6246.

[68] C. Heine, F. Girgsdies, A. Trunschke, R. Schlögl, M. Eichelbaum, *Appl. Phys. A* **2013**, *112*, 289.

[69] C. Heine, M. Hävecker, M. Sanchez-Sanchez, A. Trunschke, R. Schlögl, M. Eichelbaum, *J. Phys. Chem. C* **2013**, *117*, 26988.

[70] O. Klein, S. Donovan, M. Dressel, G. Grüner, *Int. J. Infrared Millimeter Waves* **1993**, *14*, 2423.

[71] M. Schur, B. Bems, A. Dassenoy, I. Kasatkin, J. Urban, H. Wilmes, O. Hinrichsen, M. Muhler, R. Schlögl, *Angew. Chem. Int. Ed.* **2003**, *42*, 3815.

[72] P. Kowalik, M. Konkol, K. Antoniak, W. Próchniak, P. Wiercioch, *J. Molec. Catal. A: Chem.* **2014**, *392*, 127.

2 Elucidating the importance of Cu/ZnO interactions for rWGS catalysts

Consuelo Álvarez Galván, Julia Schumann, Malte Behrens, Elias Frei, José Luis García Fierro and Robert Schlögl

2.1 Abstract

The physicochemical properties of hydroxycarbonate-based precipitates [zincian malachite (ZM) and aurichalcite precursors], calcined CuO/ZnO precatalysts and finally reduced Cu/ZnO catalysts, with several Cu-Zn ratios, have been investigated by different characterization techniques. Results from isothermal physisorption of N_2 (BET), X-ray Diffraction (XRD), Temperature Programmed Reduction (TPR), N_2O Reactive Frontal Chromatography (N_2O-RFC), X-ray Photoelectron Spectroscopy (XPS) and Scanning Electron Microscopy (SEM) have been correlated with the catalytic activity for the rWGS reaction in order to provide an insight into the still controversial nature of active species in carbon dioxide activation, respectively the role of Cu and ZnO. Average crystalline domains of CuO and ZnO show a relationship with the amount of each phase in the calcined sample. TPR analyses indicate that the ZnO phase increases the dispersion of copper particles, in which the XPS measurements point out the surface enrichment of ZnO, less pronounced with higher ZnO/(ZnO+Cu) ratios. Activity results show that high surface area ex-aurichalcite (Zn content, 50-70 % atom) catalysts are more active in rWGS than ex-ZM catalysts (Zn content, 15-30 % atom) with comparable N_2O-capacity. Thus, the CO formation rates per N_2O-chemisorption sites indicate that the reaction rate is not only dependent on these surface sites. In accordance with our characterization results, we have to point out that the precursor structure and the corresponding intimate interspersion of the Cu and ZnO

components are crucial. It seems that Cu/ZnO interface is as important as an optimized metal ratio.

2.2 Introduction

Carbon dioxide has been attributed to be the main source of the greenhouse effect. Nowadays, there are increasing attempts to consider it as a resource, rather than waste, since large amounts of low cost and relatively pure carbon dioxide will be soon available from carbon sequestration and storage facilities. The actual use of CO_2 is limited to a few processes like the syntheses of urea, salicylic acid and polycarbonates, but these only correspond to a few percentage of the potential CO_2 suitable to be converted to chemicals and/or fuels.[1] The catalytic conversion of CO_2 with H_2, via the reverse water-gas shift (rWGS) reaction, has been recognized as one of the most promising processes for CO_2 utilization. Synthesis gas could be used to produce hydrocarbons or oxygenated hydrocarbons via Fischer-Tropsch reaction, and also for the synthesis of methanol, a basic chemical for the production of synthetic fuels and polymers. Among other formulations, Cu/ZnO based systems are active catalysts for the rWGS (eq. 2.1)[2] and for the synthesis of methanol (eq. 2.2)[3] at low temperatures (443-523 K).

$$CO_2 + H_2 \rightleftharpoons CO + H_2O \qquad \Delta H_{298K} = 41\ \mathrm{kJ\,mol^{-1}} \tag{2.1}$$

$$CO_2 + 3\,H_2 \rightleftharpoons CH_3OH + H_2O \qquad \Delta H_{298K,1bar} = -50\ \mathrm{kJ\,mol^{-1}} \tag{2.2}$$

Although methanol synthesis as well as the (r)WGS reaction on Cu/ZnO have been investigated for several decades, many controversies still exist about the reaction mechanism and active sites of the catalyst. Although a copper metal surface is widely regarded as the primary reaction center in the forward, the reverse shift and in methanol synthesis, according to previous studies, different phases could have a role in the activity of above systems: Cu^0,[4] Cu^+ in the lattice of ZnO,[5,6] the Schottky barrier at the Cu-ZnO interface,[7,8] defects in ZnO (oxygen vacancies) formed on the surface on ZnO crystals,[9] active sites for CO and CO_2 chemisorption[6] or a strong metal-support interaction (SMSI effect) by which Cu particles are partially covered or encapsulated by ZnO.[10,11] Another important issue which has not been solved yet is the question, whether the rWGS reaction and methanol synthesis go through the same intermediate, or even happen at the same active site. It is generally accepted, that Zn plays an active role for methanol synthesis,[12–14]

but for the rWGS this is still controversial. Whereas some studies do not see a promotional effect of ZnO [12,13,15] others report that there is a beneficial effect of ZnO. [16,17] The role of CO_2 in methanol synthesis is ambiguous. On the one hand, it has been shown in isotope-labelled experiments under differential conditions, that CO_2 is the carbon source of methanol. [14,18] It is known as well, that CO_2 in the feed prevents the over-reduction of the ZnO component. [19–21] On the other hand, the formation of water as byproduct of the methanol synthesis from CO_2 and rWGS has an inhibitory effect on the activity, probably by blocking the active sites on the surface. [22–24] Further, CO can act as a scavenger for the surface water. [25] However, in order to get a better control over the selectivity of the reaction pathway (methanol synthesis vs. rWGS reaction), it is necessary to understand the reactions and the role of the preparation history of the catalyst. In this study, the influence of the nominal Cu/Zn ratio on the properties of the catalysts and its role in the reactivity in the rWGS reaction has been examined. Different binary Cu/ZnO catalysts have been prepared by a controlled and automatized co-precipitation method, which ensures the reliability of the changing physicochemical properties. Furthermore, we have analyzed the influence of the precursor phases zincian malachite [$(Cu,Zn)_2(OH)_2CO_3$] and aurichalcite [$(Zn,Cu)_5(OH)_6(CO_3)_2$] on the microstructure and activity of the Cu/ZnO catalysts in the rWGS reaction. The different materials obtained during the genesis of the final catalyst samples, like copper and zinc hydroxycarbonates (precursors), calcined samples (precatalysts) and reduced samples (catalysts) have been thoroughly analyzed by different techniques (BET-SA, XRD, XRF, TPR, XPS and SEM). In the second part of the paper, the activities of the catalysts for the production of carbon monoxide and their activation energies by the rWGS reaction have been evaluated and correlated to their physicochemical properties. Because of the endothermic nature of the reaction, a high reaction temperature is favorable in the rWGS reaction to shift the equilibrium and generate more CO. However, we have used lower temperatures in the activity tests, since the goal of this study is to elucidate the reactivity of CO_2 and H_2 with Cu-ZnO catalysts for the comparison to the methanol synthesis reaction.

2.3 Experimental methods

2.3.1 Preparation of Cu-Zn catalysts precursors

As reported in the literature, [26] the microstructural arrangement of CuO and ZnO particles in the catalyst precursor is determined by the physicochemical properties of the precipi-

tates, that strongly depends on small variations in the precipitation and post-precipitation processes. Variations of the conditions such as the mode of adding the reactants, precipitation pH, ageing time, ageing temperature, washing, etc. are responsible for the so called ŽŽchemical memory"of the precipitates when they are converted into Cu/ZnO catalysts. According to previous studies, the Cu/Zn-precursors were prepared by a pH-controlled co-precipitation[27] in an automated reactor (LabMax from Mettler-Toledo). Different phases were systematically prepared: aurichalcite (Cu:Zn, 50:50, 40:40 and 30:70, molar ratios) and zincian malachite (Cu:Zn, 85:15, 80:20, 75:25 and 70:30). The proper amount of $Zn(NO_3)_2 \cdot 6\,H_2O$ and $Cu(NO_3)_2 \cdot 3\,H_2O$ was dissolved in Millipore water and 15 mL of concentrated HNO_3 to obtain 600 mL of a 1 M solution of the metal salts. This solution was added to the partially filled reactor at a constant rate of 20 mL/min. The proper amount of Na_2CO_3 solution (1.6 M) was automatically added to keep the pH constant at 6.5. The precipitation temperature was adjusted to 338 K. The precipitation process was followed by an ageing time of 1 h (338 K, pH=6.5), once the turbidity started to increase. The solid was then filter-collected and washed several times by redispersion in water until the conductivity of the washing medium was below 0.5 mS/cm. The solid hydroxy-carbonate precursors were obtained by spray drying. Calcination of the precursor for 3 h at 603 K yielded the CuO-ZnO precatalysts.

2.3.2 Characterization methods

XRD data were collected using a Bruker AXS D8 Advance Theta-theta diffractometer in Bragg-Brentano geometry, equipped with Cu anode, incident beam germanium monochromator (CuK radiation) and scintillation counter. Measurements were taken between 4 and 80° 2θ with a step width of 0.5° and a counting time of 30 s/step. The diffractograms were analyzed by Rietveld fitting using the Topas software package[28] from Bruker AXS to extract the lattice parameters, estimate phase composition and determine the mean crystallite size from the L_{vol}-IB value. BET surface area was calculated from isothermal N_2 adsorption (77 K) in a Quantachrome 6 port BET system. Prior to the measurements the samples were evacuated for 2 h at 373 K. Temperature programmed reduction (TPR) studies have been conducted on a TPD/R/O 1100 instrument (CE Instruments). TPR studies were carried out by passing 5 vol.% H_2/Ar at a flow of 80 mL/min over a certain amount of the catalyst sample, maintaining the amount of copper oxide constant (25 mg). The temperature was increased to 573 K with a heating ramp of 6 K min^{-1}. The apparent Cu^0 surface area (SA) of the reduced catalysts was measured by nitrous oxide

(N_2O) chemisorption using the Reactive Frontal Chromatography (RFC) method.[29] Recent results revealed, that N_2O-RFC not only reacts with the Cu surface atoms, but also reacts with partially reduced ZnOx species.[30,31] Therefore, the Cu-SA was overestimated in samples containing ZnO and we will refer to it as the apparent Cu^0-SA. Exposed Cu^0 and partially reduced ZnO_x surfaces of a pre-reduced Cu/ZnO catalyst were oxidized by switching the feed from an inert He stream to a reactive N_2O/He mixture. The N_2O capacity of the samples was calculated by quantifying the amount of released N_2. A detailed description of the experiment can be found in the section 2.8. X-ray photoelectron spectra were recorded with a VG 200 R electron spectrometer operated in a constant pass mode and provided with a non-monochromatic MgK_α ($h\nu$ = 1253.6 eV, 1 eV = $1.603 \cdot 10^9$ J) X-ray source operated at 10 mA and 12 kV. Prior to the analysis the reduced and passivated samples were subjected to reduction (493 K, in H_2 flow, for 10 min) in the treatment chamber of the spectrometer. The residual pressure in the ion-pumped analysis chamber was maintained below $4.2 \cdot 10^{-9}$ mbar during data acquisition. The Cu 2p; Zn 2p; O 1s and C 1s energy regions were recorded for each sample and the respective binding energies (BE) were calibrated using the C 1s line at 284.9 eV as internal reference. BE values within an accuracy of 0.2 eV were obtained. Data processing was performed with the XPS peak program. For details see Appendix. X-ray fluorescence spectroscopy (XRF) was performed of the precursor powder in a Bruker S4 Pioneer X-ray spectrometer. Scanning electron microscopy (SEM) images were taken in a Hitachi S-4800 field emission gun (FEG) system.

2.3.3 Activity test

Preliminary runs were carried out to determine the proper catalyst particle size and reactant flow to avoid internal and external diffusion resistance, respectively. Catalytic activity measurements were carried out in an 8-fold parallel reactor setup for rWGS. We used tubular quartz glass reactors with an inner diameter of 6 mm. The reactor was placed inside a programmable furnace and the temperatures were measured using type K thermocouples placed in the catalyst beds. 20 mg catalyst of a defined sieve fraction (0.1-0.2 mm) was diluted with SiC, to improve heat transport and prevent hotspot formation. Prior to the activity tests, the samples were reduced in situ in a 5 % H_2 in N_2 flow (30 mL/min) with a heating ramp of 1 K min^{-1} to 523 K and a holding time of 30 min. For the activity tests, a space velocity of 520 h^{-1} (GHSV) and a H_2/CO_2 ratio of 1 was used. The gas flows (H_2:CO_2:N_2 1:1:8) were adjusted by mass flow controllers. The feed and product

gas compositions were determined by online gas chromatography (GC), equipped with a thermal conductivity detector (TCD). Helium was used as the carrier gas and separation was accomplished using PPQ and mole sieve columns. The product gas composition was measured at 473 up to 503 K and reported values are averages from at least 3 consecutive analyses.

2.4 Results and discussion

2.4.1 Characterization of the precursors

The XRD patterns of the co-precipitated precursors show (Figure 2.1) that for high Cu:Zn ratios (Cu content $\geq$ 70 at%), the zincian malachite (ZM) [$(Cu,Zn)_2(CO_3)(OH)_2$] phase dominates.

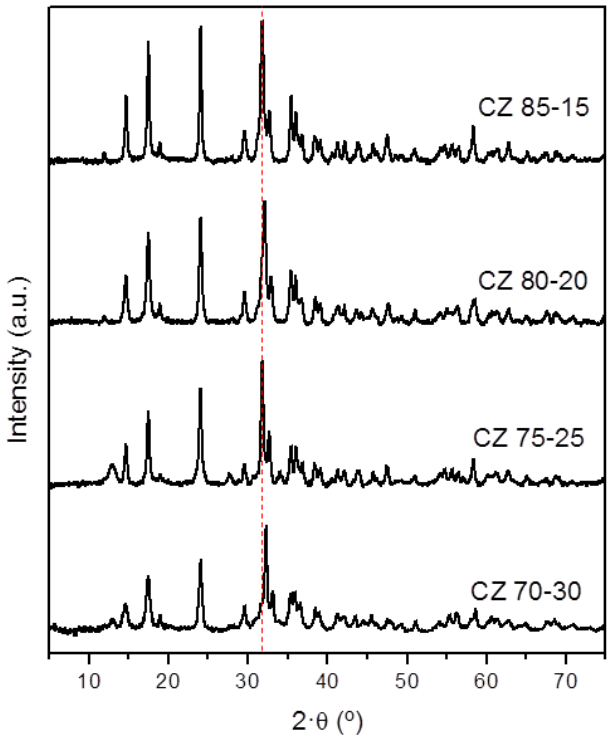

Figure 2.1: Powder XRD patterns of the different Cu-rich zincian malachite precursors.

The structure of the ZM phase can be derived from the malachite crystal structure [$Cu_2CO_3(OH)_2$], by replacing some of the Cu^{2+} ions with Zn^{2+}. This replacement leads to changes in the lattice parameters, e.g. contraction of the cell volume, as already noted by Porta et. al.[32] The most dominant change observed in the XRD pattern is the shift of the d($20\bar{1}$) reflection (red line in Figure 2.1 to guide the eye), which scales linearly with the amount of incorporated zinc.[33,34] This change is observed for our samples as well (Table 2.1).

Table 2.1: Chemical composition (XRF), d-spacing of the $20\bar{1}$ reflection (XRD), BET surface area and reduction properties of the precatalysts

Sample	**Cu:Zn (XRF)**	**d($20\bar{1}$) [Å]**	**BET [m^2/g]**	**T_{onset} [K]**	**T_{max} [K]**	**% area (1st peak)**	**% area (2nd + 3rd peak)**
CZ 85-15	85:15	2.809	22	417	482	26	74
CZ 80-20	80:20	2.789	43	410	474	24	76
CZ 75-25	75:25	2.797	50	420	478	28	72
CZ 70-30	70:30	2.770	53	414	466	22	78
CZ 50-50	50:50	2.802	52	410	468	44	56
CZ 40-60	40:60	-	55	420	471	44	56
CZ 30-70	31:69	-	64	428	485	43	57

For the precursors CZ 85-15 and CZ 80-20, pure ZM is obtained, while for CZ 75-25 and CZ 70-30, additionally a minor amount ($< 10\%$) of aurichalcite is present, seen at the additional reflex at 13° 2θ. This also explains the deviation of the d($20\bar{1}$) value for CZ 75-25. Because of the enrichment of Zn in the aurichalcite byphase, a higher d($20\bar{1}$) value (corresponding to a lower amount of Zn in the ZM structure) than expected is observed. For low Cu:Zn ratios (Cu contents $\leq$ 50 at%), the aurichalcite [$(Cu,Zn)_5(CO_3)_2(OH)_6$] is the main phase, with a minor zincian malachite impurity for the CZ 50-50 sample (Figure 2.2).

BET surface areas of the precursors decrease with increasing Cu content from 64 m^2/g for CZ 30-70 to 22 m^2/g for the copper richest CZ 85-15 sample (Table 2.1, Figure 2.3).

SEM micrographs show different morphologies for different precursor structures (Figure 2.4). Thin platelets were found for the CZ 40-60 (aurichalcite, Figure 2.4b) and rod-like for the CZ 80-20 (ZM, Figure 2.4a) sample. The smaller microstructures found in the aurichalcite samples are in accordance with the higher surface areas obtained for these precursors. XRF results showed, that the Cu/Zn-ratios in the precursors correspond to their nominal values (see Table 2.1).

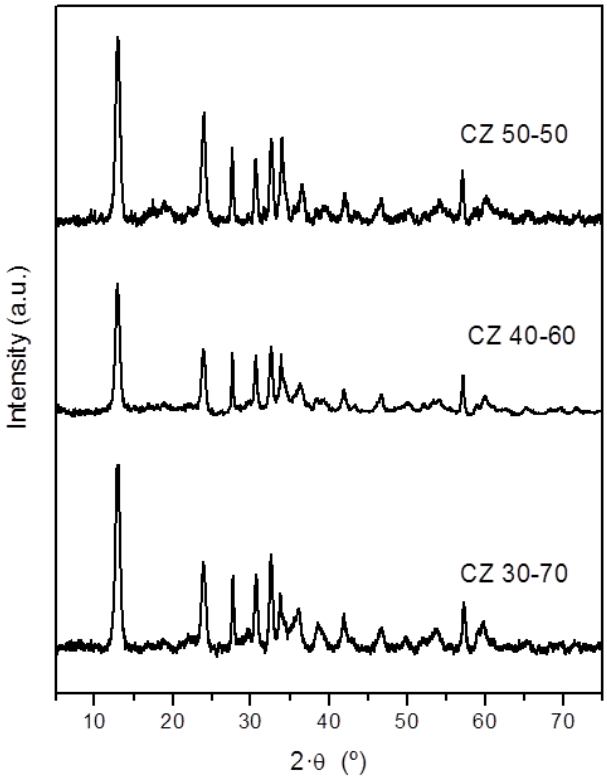

Figure 2.2: Powder XRD patterns of the different aurichalcite precursors.

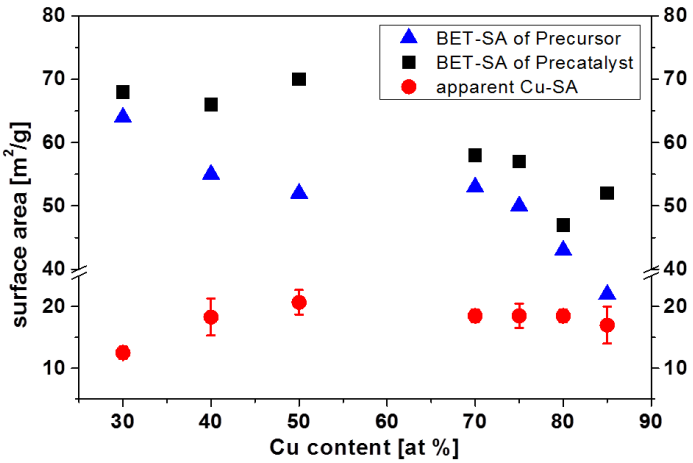

Figure 2.3: BET-SA of the precursors (triangles, blue), precatalysts (squares, black) and the apparent Cu-SA of the reduced catalysts (circles, red).

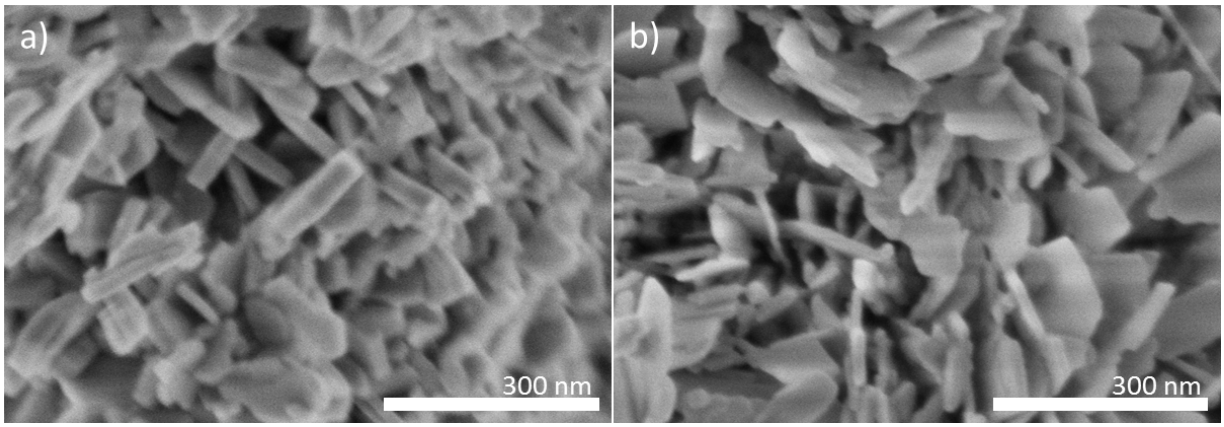

Figure 2.4: SEM images of the precursors morphology: a) zincian malachite and b) aurichalcite.

2.4.2 Characterization of the precatalyst

After the calcination, the precatalysts were characterized by: (i) X-ray Diffraction to determine the phase composition and crystallite size, (ii) by isothermal physisorption of N_2 at 77 K, to determine the surface area with the BET method and by (iii) temperature programmed reduction (TPR), to analyze the composition and interaction between different phases. After the calcination process, all the samples formed particles of CuO and ZnO with crystallite domains smaller 7 nm (see Figure 2.5). Obtained results showed a progressive growth of the crystallite size of the metal oxides with an increase of the corresponding cation ratio. Calcination of the precursors led for all samples to an increase of the surface area (Figure 2.4).

In accordance with some results reported in the literature for similar precursors, the surface area of the precatalysts reach a maximum value for the samples consisting of equal amounts of Cu and Zn.[35] However, the higher Cu content leads to bigger, less dispersed particles with a lower surface area. The reduction profiles of the precatalysts are displayed in Figure 2.6. The Cu-rich samples fit very well with the XRD results of the precursors. The more Zn is incorporated into the ZM structure measures by the shift of the d($20\bar{1}$) value, the less stable and earlier reducible is the resulting sample. This can be observed in the shift of the maximum temperature of the reduction profiles of the calcined samples derived from ZM-precursors, from 482 K, for calcined CZ 85-15 to 466 K, for calcined CZ 70-30 (Table 2.1; see also Figure 2.6). According to the general interpretation, the first peak, with a flat maximum around 440 K for calcined samples derived from zincian malachite-precursors and around 465 K for calcined samples derived from aurichalcite-precursors, is associated to highly dispersed CuO particles. As reported in Table 2.1, the

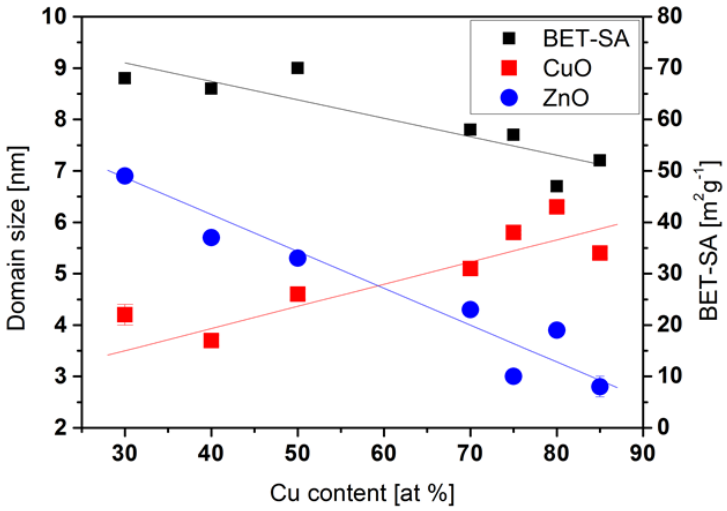

Figure 2.5: BET-SAs of the precatalysts (squares, black) and the corresponding crystallite domain size of CuO (squares, red) and ZnO (circles, blue).

area of this contribution compared to the overall reduction area is higher for the samples derived from aurichalcite-precursors, pointing out that this type of precursors gives rise to catalysts with a higher dispersion of the Cu phase. Another study investigating different precursor systems came to the conclusion, that a lower temperature shoulder is attributed to the first reduction step from Cu(II) to Cu(I). If the Cu(I) species is kinetically stabilized by a strong interaction with the oxide matrix the shoulder is more pronounced.[36,37] The ex-aurichalcite samples show a greater area of the low-temperature shoulder, compared to the ex-ZM samples, which either indicates that a large fraction of highly dispersed CuO species is formed or that the interaction of Cu(I) intermediate with ZnO is stronger in ex-aurichalcite samples than in the ex-ZM samples. The second contribution, with a maximum above 465 K, is attributed to a fraction of crystalline, difficult to reduce CuO particles.[38–42] The increase in the contribution of this peak to the total reduction profile in samples with a higher proportion of ZnO may also indicate a strong interaction of copper with the support due to a stronger embedment of CuO in the ZnO matrix, which hinders the reduction process. Some authors explain this reduction peak at high temperature by the development of a SMSI effect.[43,44] As observed in Figure 2.6 the proportion of this last peak to the overall hydrogen consumption is higher for aurichalcite-derived samples, which would indicate a stronger development of this effect with increasing Zn content.

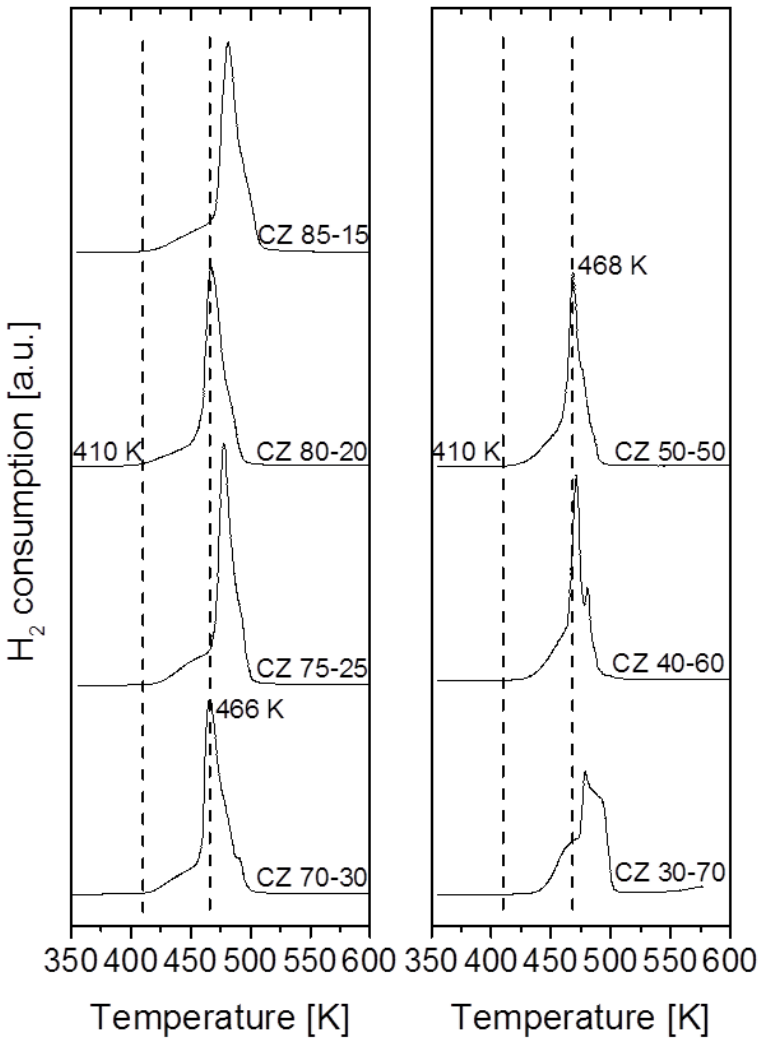

Figure 2.6: TPR profiles of all precatalysts, the dashed lines highlight the lowest T_{onset} and lowest T_{max} temperatures.

2.4.3 Characterization of the catalysts

The activation treatment in a reductive atmosphere at 523 K, described in the experimental section, is sufficient to reduce the CuO crystallites in the precatalysts to Cu metal, as seen in the TPR profiles. The reduced samples are characterized by N_2O decomposition to determine the apparent specific SA of Cu^0 and by XPS in order to analyze the surface composition. Results obtained by the N_2O-RFC (Figure 2.5 and Table S.2.2), point out that the apparent Cu^0-SA are close to 19 m^2/g for all the reduced samples, except for the sample CZ 30-70 (r), which presents a value around 12 m^2/g due to the small amount of Cu present in the sample. The maximum value of 21 m^2/g is found for the catalyst CZ 50-50 with the same ratio of Cu and Zn and the highest BET-SA of the precatalysts. Although the amount of Cu is higher in the samples derived from ZM precursors, the apparent Cu-SAs are smaller. In these samples the proportion of ZnO seems not to be high enough to provide a better dispersion of the Cu phase, as also seen in the bigger domain size of CuO in the precatalysts. Additionally a more pronounced sintering during the reduction stage could occur.[15] The higher apparent Cu-SA of the CZ 50-50 sample, could also be originated in the similar particle sizes of 5 nm for ZnO and CuO in the precatalyst, which avoids the sintering of Cu and facilitates the partial reduction of ZnO to ZnO_x (which would lead to an additional N_2O consumption).[30] XPS measurements provide valuable information about the surface state of the freshly reduced catalysts. As the binding energies of both Cu^0 and Cu^+ species are quite similar, the modified Auger parameters were calculated to differentiate which of these Cu species are present in the reduced catalysts. Typical values of this parameter around 1851.3 and 1849.5 eV were found in the literature for Cu^0 and Cu^+ species, respectively.[45] The binding energies of the core electrons and the modified Auger parameters (α_A) were determined for all the catalysts and obtained values are reported in Table 2.2. As representative spectra, the Cu $2p_{3/2}$ photoelectron and CuLMM Auger spectra of catalyst CZ 50-50 are shown in Figure S.2.1. All the samples display a narrow peak for $Cu2p_{3/2}$ centered around 932.1-932.4 eV.[35,46,47] The Auger parameters of Cu in all the samples (1852.0-1852.2) indicate the presence of metallic Cu^0 species on the surfaces of the catalysts, exclusively (Table 2.2).

There are no significant variations in the binding energies of Zn as a function of the Cu/Zn ratio and values corresponding to the Zn $2p_{3/2}$ core level are indicative of ZnO.[45,48,49] Here, it is no direct spectroscopic evidence of a partially reduced ZnO_x species. Hence, the partial Zn amounts at the surface have been calculated (Table 2.2). For all catalysts, an enrichment of Zn at the surface is occurring. This phenomenon is well known in the

Table 2.2: Auger parameters and Binding energies (eV) of core levels and surface atomic ratios of Cu/ZnO catalysts determined by X-ray Photoelectron Spectroscopy

Catalyst	$Cu2p_{3/2}$	$Zn2p_{3/2}$	CuLMM	α_A	Nominal Zn/(Cu+Zn)	Surface Zn/(Cu+Zn)
CZ 85-15	932.2	1021.6	334.6	1852.1	0.15	0.54 (260%)[a]
CZ 80-20	932.1	1021.6	334.6	1852.1	0.20	0.61 (205%)[a]
CZ 75-25	932.2	1021.6	334.6	1852.2	0.25	0.72 (188%)[a]
CZ 70-30	932.1	1021.5	334.5	1852.2	0.30	0.70 (133%)[a]
CZ 50-50	932.2	1021.6	334.7	1852.1	0.50	0.82 (64%)[a]
CZ 40-60	932.1	1021.6	334.7	1852.0	0.60	0.80 (33%)[a]
CZ 30-70	932.1	1021.6	334.6	1852.1	0.70	0.83 (19%)[a]

[a]Comparison of the nominal and surface value of Zn/(Cu+Zn) ratio, to quantify the Zn-enrichment at the surface.

literature and commonly explained by the strong metal support interaction (SMSI) of Cu and ZnO[14,46,47]: Under reducing conditions ZnO_x species partially cover the Cu surface. The calculation of the relative surface Zn enrichment, comparing the surface Zn/Cu ratios and the nominal counterparts (values in brackets, Table 2.2 last column), evidences a trend of a lesser Zn surface enrichment with an increase of the nominal Zn/Cu ratio. This observation would also fit with the consecutive growth of the ZnO particle size in the precatalysts with the increasing Zn/Cu ratio (Figure 2.4).

2.4.4 Activity tests of the catalysts

The activity for the rWGS reaction of the catalysts derived from the precursors with different Cu:Zn ratios was determined using differential testing conditions, with CO_2 conversions below 4% in the entire temperature range. The activity per mass of the catalysts at 503 K and activation energies versus the Cu content are shown in Figure 2.7.

These results indicate a better catalytic performance for the catalysts with similar proportions of Cu and Zn, derived from the aurichalcite enriched precursors. The most active catalyst is the CZ 40-60, closely followed by sample CZ 50-50.[15] The higher activity of these samples is in accordance with the corresponding lower activation energies for the rWGS reaction. The lowest CO_2 conversion values for all the reaction temperatures are obtained for the CZ 85-15 catalyst, followed by the catalyst CZ 80-20 and CZ 75-25, all derived from a ZM phase (see also Figure S.2.2). The activity data as a function of the apparent Cu-SA values are shown in Figure 2.8. For similar Cu-SA values (18 - 21 m^2/g),

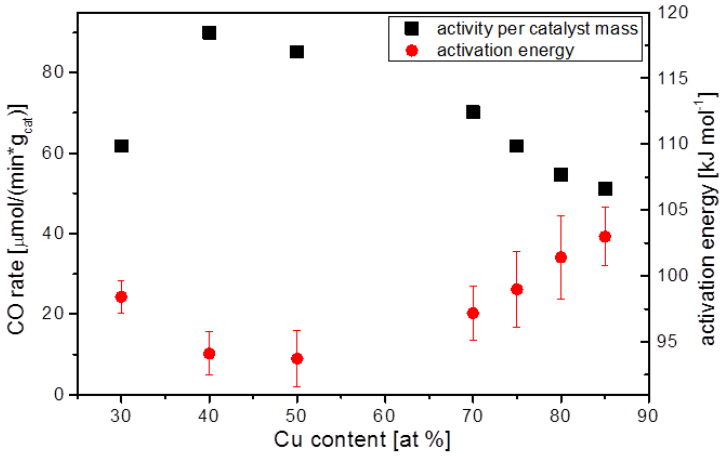

Figure 2.7: CO formation rate per the catalyst masses and activation energies, as a function of the Cu content.

the ex-aurichalcite samples show a much higher activity than the corresponding ex-ZM samples. This is a clear indication, that not only the apparent Cu-SA, but also other factors are crucial for the rWGS reaction and points out the importance of the Cu/ZnO interface determined by the initial state of the precursor formation. This is in contrast to the results of Stone and Waller.[15]

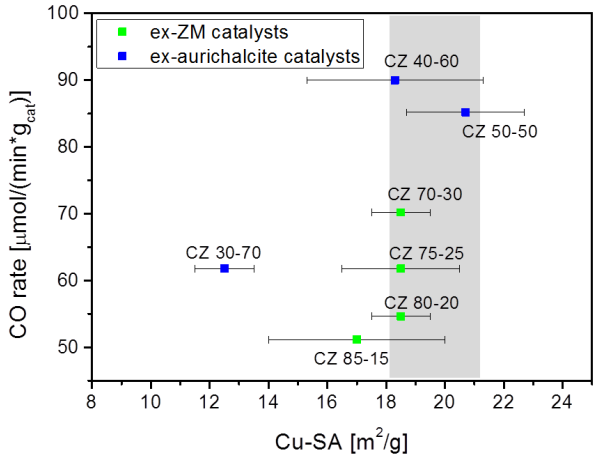

Figure 2.8: Activity per catalyst masses in the rWGS reaction related to the apparent Cu-SAs. The dashed lines highlight the region of comparable apparent Cu-SA and the corresponding activity differences.

Referring to the reaction order of H_2 (0.11 - 0.15) and CO_2 (0.26 - 0.3) for $H_2/CO_2 \geq 3$ (Table S.2.3), the CO_2 activation is more critical. That means the rate determining step involves the CO_2 activation, and obviously the Zn-richer samples cope better with this, independent from their apparent Cu-SA.[50] That means the ex-aurichalcite catalysts provide a special interaction/activity and do not only display a higher number of active sites for CO_2 adsorption. The likely coverage of Cu phase by ZnOx species with O vacancies at the Cu/ZnO interface could create these adsorption sites for CO_2, facilitating its adsorption.[11]

2.5 Conclusions

A series of binary Cu/ZnO catalysts was prepared by calcination and reduction of either zincian malachite precursors (70 < Cu content < 85, atom %) or aurichalcite precursors (30 < Cu content < 50, atom %). SEM analyses show different morphology for different precursor structures: thin sheets in case of aurichalcite and more massive, column-like rods for zincian malachite, which is in accordance with the lower BET surface areas of the precursors with increasing Cu content. The calcination of these precursors forms a microstructure arrangement of CuO and ZnO particles with average domain sizes smaller 7 nm. The domain sizes of the oxides increase with an increase of the respective metal content. Larger surface areas result for the calcined ex-aurichalcite samples. The reduction profiles suggest a higher dispersion of CuO particles and also a stronger embedment of these phases with increasing proportion of Zn. Apparent copper surface areas of Cu/ZnO catalysts, determined by N_2O RFC, indicate values around 19 m^2/g (except for 30:70 sample). As revealed by XPS, the surface composition of Cu/ZnO catalysts (reduced samples) is based on copper in metallic state and ZnO. The analyses suggest that a higher proportion of ZnO prevents the Cu particles to sinter and lowers the tendency of a ZnO surface enrichment. The quantity of this surface enrichment does not correlate with the activity in the rWGS reaction. It seems that only a small part of ZnO on the enriched surface is responsible for the activity and a further deposition of "bulk ZnO" has an inverse effect. Activity results of these catalysts for the rWGS reaction show that ex-aurichalcite catalysts are more active than ex-zincian malachite catalysts with comparable Cu surface areas. This is probably a result of a beneficial microstructure providing high BET-SAs and an optimized Cu-Zn interface.

2.6 Acknowledgements

Part of this work was carried out during the stay of MCAG at Fritz Haber Institute from Max Planck Society (Department of Inorganic Chemistry). She gratefully acknowledges the German Research Foundation (DFG) for financial support and the group members for their help and hospitality. The authors thank Pierre Kube, Tom Cotter and Pierre Schwach for their help with the catalytic measurements, Gisela Lorenz for BET analyses; Edith Kitzelmann and Frank Girgsdies for XRD analyses, and Wiebke Frandsen for SEM analyses.

2.7 References

[1] G. Centi, S. Perathoner, *Catal. Today* **2009**, *148*, 191.

[2] Y. Tanaka, T. Utaka, R. Kikuchi, K. Sasaki, K. Eguchi, *Appl. Catal., A* **2003**, *242*, 287.

[3] T. Ressler, B. L. Kniep, I. Kasatkin, R. Schlögl, *Angew. Chem.* **2005**, *117*, 4782.

[4] G. Chinchen, K. Waugh, D. Whan, *Appl. Catal.* **1986**, *25*, 101.

[5] T. M. Yurieva, L. M. Plyasova, T. A. Kriger, V. I. Zaikovskii, O. V. Makarova, T. P. Minyukova, *React. Kinet. Catal. Lett.* **1993**, *51*, 495.

[6] K. Klier, in D. Eley, H. Pines, P. B. Weisz, Eds., *Adv. Catal.*, Vol. 31, Academic Press, **1982**, pp. 243–313.

[7] J. C. Frost, *Nature* **1988**, *334*, 577.

[8] F. Liao, Y. Huang, J. Ge, W. Zheng, K. Tedsree, P. Collier, X. Hong, S. C. Tsang, *Angew. Chem. Int. Ed.* **2011**, *50*, 2162.

[9] S. Miao, R. N. d'Alnoncourt, T. Reinecke, I. Kasatkin, M. Behrens, R. Schlögl, M. Muhler, *Eur. J. Inorg. Chem.* **2009**, *2009*, 910.

[10] J.-D. Grunwaldt, A. Molenbroek, N.-Y. Topsøe, H. Topsøe, B. Clausen, *J. Catal.* **2000**, *194*, 452.

[11] R. Naumann d'Alnoncourt, X. Xia, J. Strunk, E. Löffler, O. Hinrichsen, M. Muhler, *Phys. Chem. Chem. Phys.* **2006**, *8*, 1525.

[12] T. Fujitani, I. Nakamura, T. Uchijima, J. Nakamura, *Surf. Sci.* **1997**, *383*, 285.

[13] I. Nakamura, T. Fujitani, T. Uchijima, J. Nakamura, *Surf. Sci.* **1998**, *400*, 387.

[14] M. Behrens, F. Studt, I. Kasatkin, S. Kühl, M. Hävecker, F. Abild-Pedersen, S. Zander, F. Girgsdies, P. Kurr, B. L. Kniep, M. Tovar, R. W. Fischer, J. K. Nørskov, R. Schlögl, *Science* **2012**, *336*, 893.

[15] F. S. Stone, D. Waller, *Top. Catal.* **2003**, *22*, 305.

[16] J. A. Rodriguez, P. Liu, J. Hrbek, J. Evans, M. Pérez, *Angew. Chem. Int. Ed.* **2007**, *46*, 1329.

[17] Y. Yang, J. Evans, J. A. Rodriguez, M. G. White, P. Liu, *Phys. Chem. Chem. Phys.* **2010**, *12*, 9909.

[18] G. Chinchen, P. Denny, D. Parker, M. Spencer, D. Whan, *Appl. Catal.* **1987**, *30*, 333.

[19] B. Denise, R. Sneeden, B. Beguin, O. Cherifi, *Appl. Catal.* **1987**, *30*, 353.

[20] D. King, R. Nix, *J. Catal.* **1996**, *160*, 76.

[21] J. Lee, K. Lee, S. Lee, Y. Kim, *J. Catal.* **1993**, *144*, 414.

[22] K. Fujimoto, Y. Yu, *Second Int. Conf. Spillover* **1993**, 393.

[23] T. Inui, T. Takeguchi, *Catal. Today* **1991**, *10*, 95.

[24] E. Kunkes, M. Behrens, *Chemical Energy Storage*, De Gryter, Berlin/Boston, **2013**.

[25] C. Yang, Z. Ma, N. Zhao, W. Wei, T. Hu, Y. Sun, *Catal. Today* **2006**, *115*, 222.

[26] B. Bems, M. Schur, A. Dassenoy, H. Junkes, D. Herein, R. Schlögl, *Chem. Eur. J.* **2003**, *9*, 2039.

[27] M. Behrens, *J. Catal.* **2009**, *267*, 24.

[28] A. Coelho, *TOPAS: General Profile and Structure Analysis Software for Powder Diffraction Data; Bruker AXS GmbH: Karlsruhe, Germany* **2006**, *version 3.0*.

[29] G. Chinchen, C. Hay, H. Vandervell, K. Waugh, *J. Catal.* **1987**, *103*, 79.

[30] M. B. Fichtl, J. Schumann, I. Kasatkin, N. Jacobsen, M. Behrens, R. Schlögl, M. Muhler, O. Hinrichsen, *Angew. Chem. Int. Ed.* **2014**, *53*, 7043.

[31] S. Kuld, C. Conradsen, P. G. Moses, I. Chorkendorff, J. Sehested, *Angew. Chem. Int. Ed.* **2014**, *53*, 5941.

[32] P. Porta, S. De Rossi, G. Ferraris, M. Lo Jacono, G. Minelli, G. Moretti, *J. Catal.* **1988**, *109*, 367.

[33] M. Behrens, F. Girgsdies, *Z. anorg. allg. Chem.* **2010**, *636*, 919.

[34] S. Zander, B. Seidlhofer, M. Behrens, *Dalton Trans.* **2012**, *41*, 13413.

[35] J. Agrell, M. Boutonnet, I. Melián-Cabrera, J. L. Fierro, *Appl. Catal., A* **2003**, *253*, 201.

[36] A. Tarasov, S. Kühl, J. Schumann, M. Behrens, *High Temp.-High Press.* **2013**, *42*, 377 .

[37] S. Kühl, A. Tarasov, S. Zander, I. Kasatkin, M. Behrens, *Chem. Eur. J.* **2014**, *20*, 3782.

[38] S. D. Jones, H. E. Hagelin-Weaver, *Appl. Catal., B* **2009**, *90*, 195.

[39] L. Huang, W. Chu, Y. Long, Z. Ci, S. Luo, *Catal. Lett.* **2006**, *108*, 113.

[40] L. Liu, T. Zhao, Q. Ma, Y. Shen, *J. Nat. Gas Chem.* **2009**, *18*, 375.

[41] J. P. Breen, J. R. Ross, *Catal. Today* **1999**, *51*, 521.

[42] H. Jeong, K. I. Kim, T. H. Kim, C. H. Ko, H. C. Park, I. K. Song, *J. Power Sources* **2006**, *159*, 1296.

[43] J. Sloczynski, R. Grabowski, A. Kozlowska, P. K. Olszewski, J. Stoch, *Phys. Chem. Chem. Phys.* **2003**, *5*, 4631.

[44] M. G. Sanchez, J. L. Gazquez, *J. Catal.* **1987**, *104*, 120.

[45] C. D. Wagner, L. H. Gale, R. H. Raymond, *Anal. Chem.* **1979**, *51*, 466.

[46] W. Jansen, J. Beckers, J. v. d. Heuvel, A. Denier v. d. Gon, A. Bliek, H. Brongersma, *J. Catal.* **2002**, *210*, 229.

[47] J. Sloczynski, R. Grabowski, P. Olszewski, A. Kozlowska, J. Stoch, M. Lachowska, J. Skrzypek, *Appl. Catal., A* **2006**, *310*, 127.

[48] L. Alejo, R. Lago, M. A. Peña, J. L. G. Fierro, *Appl. Catal., A* **1997**, *162*, 281.

[49] B. Peplinski, W. Unger, I. Grohmann, *Appl. Surf. Sci.* **1992**, *62*, 115.

[50] M. Ginés, A. Marchi, C. Apesteguía, *Appl. Catal., A* **1997**, *154*, 155.

[51] C. D. Wagner, L. E. Davis, M. V. Zeller, J. A. Taylor, R. H. Raymond, L. H. Gale, *Surf. Interface Anal.* **1981**, *3*, 211.

2.8 Supplementary information

Content

- Description of the N_2O-RFC experiment
- Details of XPS data treatment
- Cu 2p XPS and Cu-LMM Auger spectrum of CZ 50-50
- Zn/Cu surface ratios determined from XPS
- Surface areas of precursors, precatalysts and apparent Cu-SA of reduced catalysts
- Additional activity data
- Internal FHI sample numbers

Description of the N_2O-RFC experiment

For this analysis, a sample amount of 90-100 mg precatalyst was used. After reducing the sample at 523 K for 30 min in 5% H_2/Ar (80 ml/min), it was cooled to the chemisorption temperature (298 K). After flushing with helium (40 mL/min), the flow was switched to a 1% N_2O/He mixture (10 mL/min). The N_2 signal and the delayed N_2O front, which is caused by the decomposition of N_2O to N_2 on the exposed Cu_0 and partially reduced ZnO_x surface, were monitored using a Mass Spectrometer. The Cu0 surface area was calculated assuming a molar stoichiometry of N_2O/Cu^0=0.5 and a mean Cu-atom density of $1.47 \cdot 10^{19}$ per m^2.

Details of XPS data treatment

The spectra were decomposed with the least squares fitting routine provided with the "XPS peak" software, with a Gauss/Lorentz product function and after subtracting a Shirley background. High resolution spectra envelopes were obtained by curve fitting synthetic peak components using the software "XPS peak". The raw data were used with no preliminary smoothing. Symmetric Gaussian-Lorentzian product functions were used to approximate the line shapes of the fitting components. Atomic ratios were computed from experimental intensity ratios and normalized by atomic sensitivity factors[51]. The Cu_{LMM} and Zn_{LMM} Auger peaks were also recorded and the modified Auger parameters (αA) were calculated according to the equation below, where the expression in parenthesis represents the difference between the kinetic energy of the Auger electron and the $2p_{3/2}$ photoelectron: $\alpha_{Cu} = h\nu + (KE(Cu_{LMM}) - KE(Cu\ 2p_{3/2}))$. Figure S.2.1 shows, as an example, Cu $2p_{3/2}$ photoelectron and Cu_{LMM} spectra of catalyst CZ 50-50.

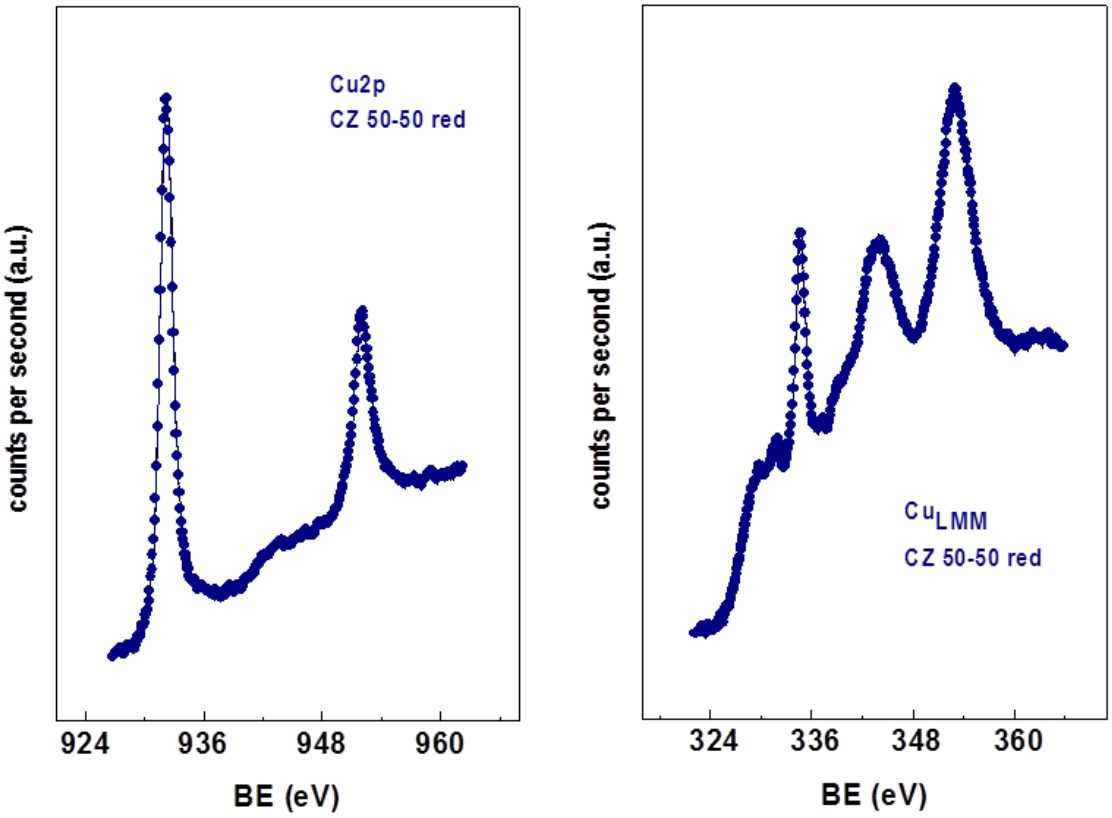

Figure S.2.1: Cu $2p_{3/2}$ photoelectron and Cu_{LMM} spectra of the catalyst CZ 50-50.

Table S.2.1: Determined Zn/Cu surface ratios from the XPS data.

Catalyst	**Surface Zn/Cu**
CZ 85-15	1.18
CZ 80-20	1.56
CZ 75-25	2.56
CZ 70-30	2.38
CZ 50-50	4.55
CZ 40-60	4.00
CZ 30-70	5.0

Table S.2.2: Surface areas of the precursors, precatalysts and the Cu-SA of the catalysts

Sample	BET-SA precursor [m^2/g]	BET-SA precatalyst [m^2/g	Apparent Cu-SA [m^2/g]	Error of Cu-SA [m^2/g]
CZ 85-15	22	52	17	3
CZ 80-20	43	47	18.5	1
CZ 75-25	50	57	18.5	2
CZ 70-30	53	58	18.5	1
CZ 50-50	52	70	20.7	2
CZ 40-60	55	66	18.3	3
CZ 30-70	64	68	12.5	1

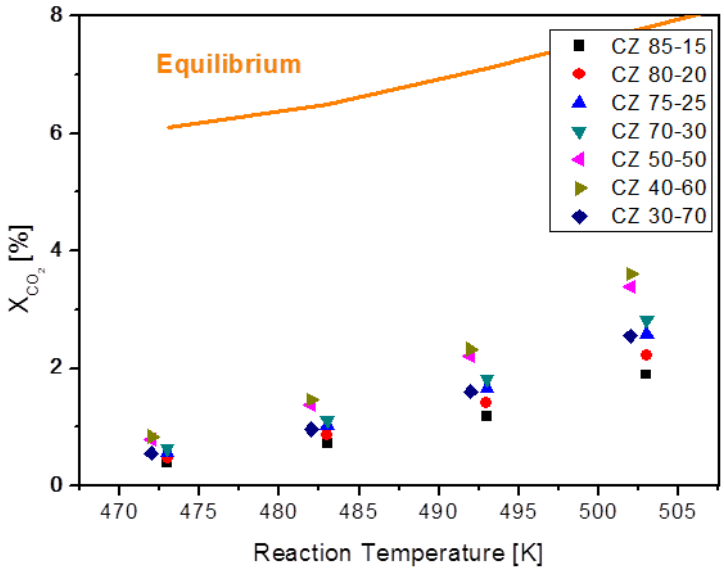

Figure S.2.2: CO_2 conversion (%) for the rWGS reaction as a function of the reaction temperature of different Cu-Zn catalysts

Table S.2.3: Results from a kinetic study of the rWGS reaction at 1 bar in a temperature range 473 - 503 K. Errors of app. Ea are determined from fitting parameters.

Catalyst	**app. E_a [kJ mol^{-1}]**	**Reaction order H_2**	**Reaction order CO_2**
CZ 85-15	103.0 ± 2.2	0.11	0.26
CZ 80-20	101.4 ± 3.2	0.13	0.31
CZ 75-25	99.0 ± 2.9	0.15	0.33
CZ 70-30	97.2 ± 2.1	0.13	0.31
CZ 50-50	93.7 ± 2.1	0.12	0.31
CZ 40-60	94.1 ± 1.6	0.12	0.28
CZ 30-70	98.4 ± 1.2	0.15	0.23

Table S.2.4: FHI internal sample numbers for future reference.

Catalyst	**Precursor #**	**Precatalyst #**
CZ 85-15	11365	13102
CZ 80-20	12716	12717
CZ 75-25	12013	12014
CZ 70-30	12707	10708
CZ 50-50	12541	12542
CZ 40-60	12630	12631
CZ 30-70	11571	11618, 13105

3 Investigating the role of high temperature carbonate by calcination experiments

Julia Schumann, Andrey Tarasov, Nygil Thomas, Robert Schlögl and Malte Behrens

3.1 Abstract

Cu/Zn based catalysts for methanol synthesis derived from zincian malachite and aurichalcite precursor phases were investigated. The decomposition process of the different hydroxy-carbonates to yield the carbonate modified metal oxides (calcined catalyst) was studied in detail. The influence of heating rates during calcination was investigated. It was possible to obtain different amounts of the so-called high temperature carbonate (HT-CO_3) in the calcined catalyst after calcination at the same temperature, which resulted in differences in crystallinity, IR spectra and decomposition profile. However, the effect on the catalytic activity was low and does not confirm a beneficial effect of large amounts of HT-CO_3 in the calcined catalyst.

3.2 Introduction

Two of the most relevant precursor phases for the preparation of Cu,Zn based catalysts are zincian malachite [$(Cu,Zn)_2CO_3(OH)_2$] (ZM) and aurichalcite [$(Cu,Zn)_5(CO_3)_2(OH)_6$] (AU).[1] Numerous studies investigated the influence of parameters of the precursor formation as ageing, pH value, temperature and elemental composition.[2–7] The activity of the final catalyst, strongly depends on the properties fixed during those early stages of the catalyst preparation. Although it is known that wrong conditions can ruin a "good" precursor phase,[8] relatively few systematic studies have been performed about the calcina-

tion step of the catalyst synthesis.[9] Typically synthetic mixed hydroxy-carbonate phases decompose in two main steps, a first one with simultaneous evolution of H_2O and CO_2 and a second one at higher temperature with evolution of CO_2 only. The intermediate is called anion modified mixed metal oxide[4] or high temperature carbonate (HT-CO_3).[2] Although the occurrence of this high temperature stable carbonate in the precursor phase is said to be beneficial for the Cu dispersion in the final catalyst,[10] detailed investigations about the calcination process and understanding of the role of HT-CO_3 for catalysis are still lacking. The influence of self-generated gaseous products on the kinetics and mechanism of thermal decomposition of synthetic malachite, $Cu_2CO_3(OH)_2$, was first studied by Koga and co-workers.[11] In water containing atmosphere the carbonate decomposes more rapidly and already at lower temperatures.[12,13] The evolved water during decomposition promotes the crystallization of CuO. This effect was also observed by Fujita et al.[9,13] who studied the influence of the heating rate during calcination on the methanol formation rate. It was demonstrated that calcination at mild heating rates results in better dispersed CuO and ZnO, thus preventing aggregation of oxides and leading to lower dispersion of metal particles in the reduced catalyst. A detailed kinetic analysis of the decomposition process of ZM and AU was published by our group recently.[12] We showed that the decomposition of the HT-CO_3 is significantly influenced by the transport conditions of the evolved water.[12] The aim of this study is to investigate the influence of the calcination parameters on the properties and catalytic performance of catalysts derived from both ZM and AU precursors, which differ in their Cu/Zn-ratio. Results of thermokinetic studies on binary Cu/Zn samples in a thermobalance as well as application on larger batch calcination experiments are presented. With the knowledge of the formal calcination kinetics, the decomposition rate as well as the amount of the reaction products can be controlled. Two series of calcined catalysts were prepared, from both ZM and AU precursor. We varied the amount of the residual HT-CO_3 by controlling water transfer conditions during the calcination. The resulting catalysts have been characterized in detail by XRD, TG analysis and IR spectroscopy and the catalytic activities in methanol synthesis have been tested. The influence of intermediate HT-CO_3 on the catalyst activity in methanol synthesis and the effect of calcination rate on the development of surface area of the binary precursors were revealed.

3.3 Experimental

3.3.1 Sample preparation

Cu/Zn precursors were prepared by pH-controlled co-precipitation[14] in an automated reactor (LabMax from Mettler-Toledo). The proper amount of $Cu(NO_3)_2 \cdot 3\,H_2O$ and $Zn(NO_3)_2 \cdot 6\,H_2O$ was dissolved in Millipore water and 15 mL of concentrated HNO_3 to obtain 600 mL of a 1 M solution of the metal salts. This solution was added to the reactor containing 400 mL of water at a constant rate of 20 mL/min. The proper amount of Na_2CO_3 solution (1.6 M) was automatically added to keep the pH constant at 6.5. The precipitation temperature was 338 K. Precipitation was followed by ageing for 1 h (338 K, pH=6.5), once the turbidity started to increase. The solid was then filter-collected and washed several times by re-dispersion in water until the conductivity of the washing medium was below 0.5 mS/cm. Approximately 40 g of the solid hydroxy-carbonate precursors were obtained by spray drying. All samples not prepared in the thermobalance were calcined in a rotating furnace, (turn number of 3, tube diameter 40 mm and length of sample bed 300 mm) with a flow of 100 mL/min in 20% O_2 in Ar. 0.75 g of the precursor powder were calcined at a maximum temperature of 603 K and a dwell time of 180 min, the heating rates were varied between 0.1 and 2 $K\,min^{-1}$.

3.3.2 Characterization methods

X-ray diffraction (XRD) data were collected using a STOE STADI P transmission diffractometer equipped with a primary focusing Ge monochromator (Cu $K_{\alpha 1}$ radiation) and a linear position sensitive detector (moving mode, step size 0.5°, counting time 30 s/step). The samples were mounted in the form of a clamped sandwich of small amounts of powder fixed with a small amount of grease between two layers of thin polyacetate film. The phase composition was determined by full pattern refinement in the 2θ range 4-80° according to the Rietveld method using the TOPAS software[15] and crystal structure data from the ICSD database. Summarized refinement parameters are displayed in the Supporting Information (SI). X-ray fluorescence spectroscopy (XRF) was performed in a Bruker S4 Pioneer X-ray spectrometer. Scanning electron microscopy (SEM) images were taken in a Hitachi S-4800 field emission gun (FEG) system. Thermogravimetric analysis (TG/DSC) was performed on a Netzsch STA449 Jupiter thermoanalyzer (10 $K\,min^{-1}$, 100 $NmL\,min^{-1}$ 21 % O_2 in Ar). Evolution of the gas phase during reaction was monitored with a quadrupole

mass spectrometer (Pfeiffer, QMS200 Omnistar). The kinetic data obtained in the TG experiments were processed using Netzsch software and are presented elsewhere.[12] The Thermokinetics program package was used for processing kinetic dependences and for component kinetic analysis. The NETZSCH Procedure is described in Ref.[16,17] IR spectra of precursors and calcined samples were recorded using an ATR Vario 670 spectrometer, equipped with an MCT detector and diamond as ATR crystal. No pretreatment of the powdered samples was performed. The aperture was set to 0.5 cm^{-1} and the resolution was 4 cm^{-1}. Spectra were recorded using 64 scans. Specific surface areas were determined by N_2 physisorption using the BET method[18] in a Quantachrome Autosorb-1 machine. Prior to analysis, the samples were degassed for 2 h at 353 K. The mesopore size distribution and pore volume were calculated according to Barrett, Joyner and Halenda modified Kelvin equation.[19] N_2O chemisorption capacity was determined using reactive frontal chromatography (RFC).[20] Approx. 100 mg of calcined sample (100-200 μm particle size) was placed in a fixed bed reactor. After in-situ reduction, the sample was cooled down in the reducing gas to room temperature, purged with He and then switched to 10 mL/min of a 1% N_2O in He mixture. The N_2O chemisorption capacity and a resulting apparent Cu surface area ($Cu\text{-}SA_{N2O}$) were calculated from the MS signal of the N_2 trace ($m/z = 28$). Apparent $Cu\text{-}SA_{N2O}$ were calculated assuming a stoichiometry of $N_2 : Cu = 1 : 2$, according to the surface reaction $N_2O + 2\,Cu \longrightarrow Cu_2O + N_2$ and an average surface density of $1.47 \cdot 10^{19}$ Cu-atoms per m^2.

3.3.3 Catalytic measurements

Methanol synthesis from syngas was tested in a fixed bed flow reactor. 50 mg (100-200 μm particle diameter, diluted with 0.7 g of SiO_2) were loaded into a 6 mm inner diameter stainless steel reactor tube using a bed volume of 1.7 mL, which resulted in a GHSV of 3500 h^{-1}. The catalyst was reduced at 523 K (1 K min^{-1}) for 1.5 hours in 20 % H_2 in Ar. Upon completion of the reduction, the reactor was cooled to 503 K, a syngas mixture with a composition of 6 % CO, 8 % CO_2, 59 % H_2 and balance Ar was introduced into the reactor, and the pressure was raised to 30 bars. Online analysis of products was performed with a gas chromatograph (Agilent 7890A). Methanol synthesis was performed under differential conditions (< 4 % conversion). Activation energies were determined in the temperature range 463 - 523 K.

3.4 Results and discussion

3.4.1 Constant mass loss calcination and its influence on the porosity

Consideration of the calcination kinetics allows controlling the decomposition rate of the hydroxy- carbonate precursor. It was demonstrated in[21] that thermal carbonization of polymer materials with constant mass loss rate has a beneficial effect on BET specific leading to a narrower pore size distribution compared to samples prepared using constant heating rate. Reading and Dollimore[22] examined thermal decomposition of synthetic malachite by means of constant rate thermal analysis (CRTA). The $Cu_2CO_3(OH)_2$ sample was thermally decomposed under flowing nitrogen maintaining a weight loss rate of 0.06 wt.% min^{-1} with a maximum temperature reached at 603 K. It was shown that there is a non-linear relationship between the extent of the decomposition reaction and the BET surface area. The surface area increases to the reaction extent of 92 % (26.4 % weight loss). A drop of the surface area is observed upon subsequent heating to final temperature. The authors suggested that water loss is associated with a greater surface area increase than carbon dioxide.

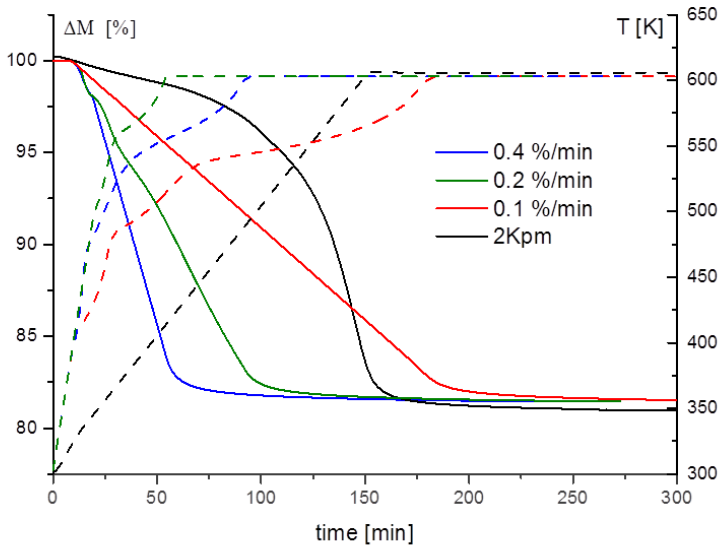

Figure 3.1: Experimental TG curves of Aurichalcite precursor with constant heating rate (black curve) and constant mass loss rate (blue, green, red curve). Dashed line indicates the temperature program.

Based on the determined formal decomposition mechanism and thermokinetic parameters[12] several temperature programs were calculated enabling calcination with the constant mass loss rate (Figure 3.1). Table 3.1 summarizes the BET-SA values of the samples calcined with constant mass loss rate and conventionally calcined carbonate precursor at constantly rising heating rate. The maximum reached temperature was 603 K, with holding time of 3 h. A decrease in the BET surface was observed with the higher heating rates. The pore size distribution of the calcined material did not undergo crucial changes within the parameter space covered (Figure S.3.1 in section 3.8), unlike demonstrated for other systems.[21] This result indicated that the properties of the calcined materials were stronger depending on the final temperature rather than on the heating rate what is in good agreement with the literature.[22] Analogues behavior was observed for the pure ZM precursor.

Table 3.1: BET-SA of the calcined AU precursor

Calcination programm	**BET-SA [$m^2 g^{-1}$]**
2 Kpm, 603 K, 3h	97
0.1 wt%/min, 603 K, 3 h	91
0.2 wt%/min, 603 K, 3 h	89
0.4 wt%/min, 603 K, 3 h	76

3.4.2 Calcination series of binary precursors

The typical calcination temperatures around 600 K would favor the formation of HT-CO_3 for both precursor structures. Further increase of calcination temperature may cause a decrease of the surface area and segregation and sintering of the metal oxides. High temperature carbonate (HT-CO_3) has been considered as a possible reason for the superior catalytic activity of methanol synthesis catalysts prepared by the co-precipitation route via basic carbonate precursors, but its exact role for the catalytic activity remained unclear.[10,23] In order to gain better understanding of the HT-CO_3 we prepared two series of catalysts by variation of the calcination conditions. The first series started from a phase pure AU, $(Zn_{1-x}Cu_x)_5(CO_3)_2(OH)_6$, (x=0.4). The second series started from the ZM precursor $(Cu_{1-x}Zn_x)(CO_3)(OH)_2$ (x=0.2). Results of formal kinetic analysis of our previous study[12] enabled us to predict the amount of the reaction products under different calcination conditions. Figure 3.2 illustrates the changes in solid components of the reaction

upon decomposition of ZM precursor at 2 Kpm. The high temperature carbonate starts to accumulate from 510 K and completely decomposes at 740 K. The total amount of the HT-CO_3 might be regulated either by varying the maximum calcination temperature or modifying the product transfer conditions e.g. by changing the heating rate or gas flow.

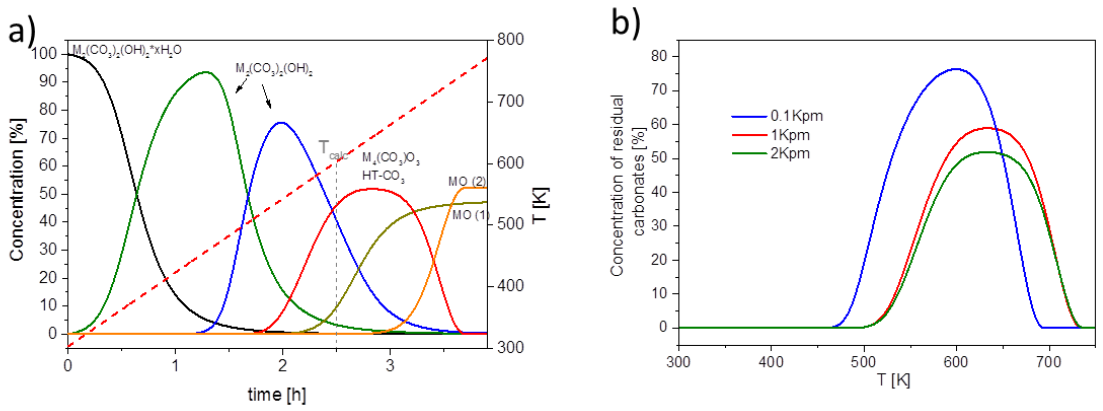

Figure 3.2: a) *Component kinetic analysis of ZM decomposition at 2 Kpm. b) Kinetic Simulation of HT-CO3 evolution at different heating rates. Based on the results of the thermokinetic calculation performed in Reference*[12].

Figure 3.2b depicts the simulated evolution of the HT-CO_3 concentration in solid products of ZM decomposition at different heating rates. By increasing the heating rate, more water accumulates in the atmosphere above the sample as the result of faster decomposition of the sample and H_2O cannot be purged out fast enough. The amount of water in the atmosphere during calcination crucially influences the decomposition kinetics of the hydroxy carbonate by promoting the decomposition of the HT-CO_3 and the crystallization of the metal oxides CuO and ZnO in agreement with results from the literature.[9,11] This effect was additionally demonstrated with experiments where H_2O was introduced artificially during the calcination process.[9,12] It should be noted that great care should be taken by upscaling the results of kinetic analysis for massive calcination ovens and larger catalyst batches. Since the mass and heat transfer conditions in the thermobalance are optimized for the TG experiment and very crucial for the process kinetics it remains difficult to impose identical conditions on the calcination furnace with other design and geometrical parameters. Taking into consideration the simulated data and conditions set in the thermobalance both precursor series were calcined in a rotating furnace with different heating rates between 0.1 and 2 Kpm and a reasonable small batch size of < 1 g. Rotation of the calcination tube was applied in order to further reduce the mass transfer limitation.

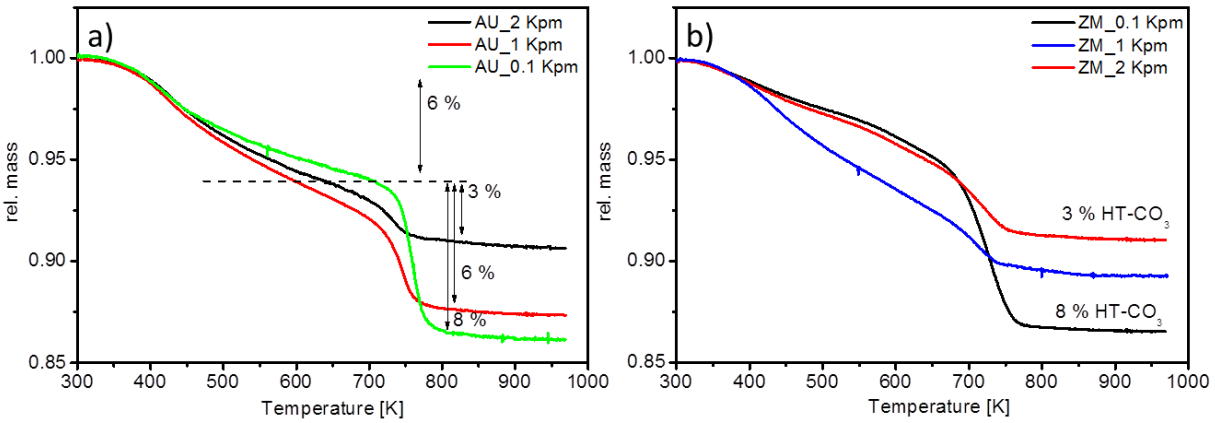

Figure 3.3: TG curves of a) calcined ex-AU samples and b) ex-ZM samples.

TG investigations of three of the calcined samples of each series revealed, that catalysts heated with different heating rates contain different amounts of HT-CO_3 after calcination (see Figure 3.3) and are thus suited to study the role of HT-CO_3 without too many other factors interfering into the data interpretation. The samples calcined with the slowest ramp of 0.1 Kpm contain the highest amount of HT-CO_3, whose decomposition led to a mass loss of about 8 %, which is close to the theoretical maximum.[12] Increasing the heating ramp up to 1 Kpm led only to small changes of the residual fraction of HT-CO_3. Only the samples calcined with the 2 Kpm ramp contained less HT-CO_3, corresponding to a mass loss of about 3 %. Samples calcined in static environment basically do not contain any strongly bound carbonates, which are released at high temperature, because the accumulating evolved gases led to a reduction of the decomposition temperature. Slow heating ramps and small amounts of sample represent very dry conditions of calcination, leading a correspondingly higher decomposition temperature of the carbonate. This was further confirmed by XRD measurements (Figure 3.4). The samples with the highest heating rates were most crystalline in both series, with domain sizes of CuO or ZnO of around 3 nm (see Table S.3.1 in section 3.8). The samples of the ex-aurichalcite series with heating rates smaller 2 Kpm were nearly amorphous, with some weak features that cannot be ascribed to either ZnO or CuO (Figure 3.4a). Some very weak features around 11° and 30° 2θ could be ascribed to originate from undecomposed AU precursor. The samples derived from the ZM precursor on the other hand all displayed crystalline CuO in their diffraction pattern. The minor component ZnO is not crystalline (see Figure 3.4). Only under harsher conditions, in static atmosphere, ZnO crystallized from the ZM phase. For

both ZM and AU phases calcination under static atmosphere led to domain sizes of CuO and ZnO of 5-6 nm (see Table S.3.1 in section 3.8).

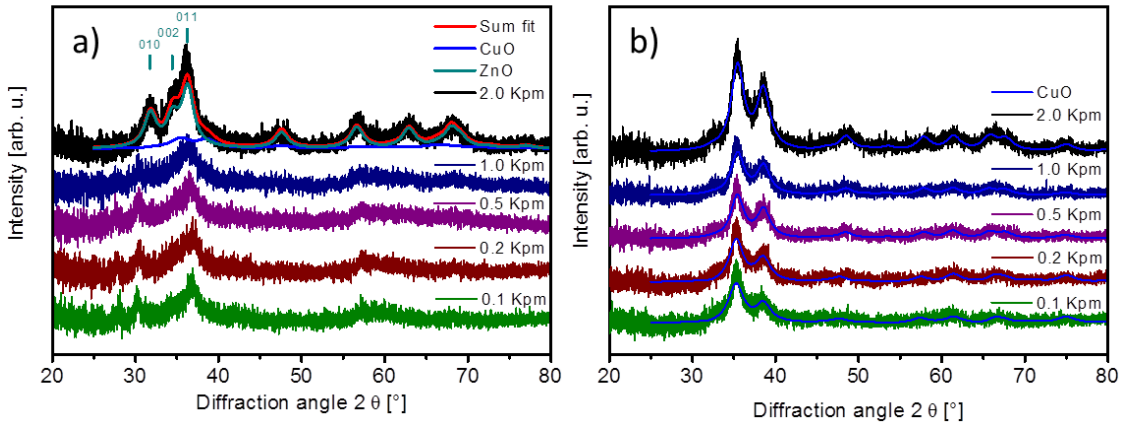

Figure 3.4: XRD pattern of a) ex-AU sample series b) ex-ZM samples calcined at 603 K for 3 h with different heating rates. The background of the pattern was subtracted and the pattern were vertically offset for clarity.

IR spectra of the calcined samples showed bands only in the carbonate and OH regions (displayed in Figure 3.5). The bands attributed to the M-OH bonds in the precursor have vanished. Comparison with the precursors showed some similarity of the HT-CO_3 with features of the precursor, especially in the AU series. The four strong bands observed in AU precursor at 1558, 1507, 1406 and 1366 cm^{-1} (see Figure 3.5a), corresponding to the asymmetric C-O stretching mode ν_3 of carbonate, agreed very well with the data published in the literature.[5,23,24] In the calcined AU sample series 4 bands could still be recognized. The position of the band at 1406 cm^{-1} had not shifted, just decreased in intensity. For the four AU samples with the lowest heating rates, the other 3 bands were shifted to lower wavenumbers by about 15 cm^{-1}. The intensity of the band with the lowest wavenumber around 1350 cm^{-1} was most intense, the other three were all about the same intensity. AU calcined at 2 Kpm differed significantly, the band at 1350 cm^{-1} shifted back slightly to higher wavenumbers, lost in intensity and all the bands broadened (see Figure 3.5a). The ZM precursor also agreed reasonably well with the literature data.[5,23] Two strong bands were observed at 1504 and 1383 cm^{-1} and a shoulder at 1427 cm^{-1} (Figure 3.5c). The calcined ZM samples differed significantly with only one very broad feature between the bands of the precursor. In this case the 2 Kpm sample was more similar to the other samples of this series, only weaker in overall intensity (see Figure 3.5c). In the range between 1200 to 500 cm^{-1} deformation vibrations of OH and further carbonate bands appeared for the precursors

(see Figure 3.5b and d). The strong and broad OH deformation bands of the precursors at 1032, 968 and 866 cm^{-1} for AU and 1101, 1049 and 865 cm^{-1} for ZM precursor all vanish after calcination, supporting the complete decomposition of the hydroxyl groups. In line with this conclusion, the special fingerprint feature for AU precursor, a M-OH band at 1208 cm^{-1}, also disappeared. Some weak bands remain that must correspond to out-of-plane and asymmetric O-C-O bending modes of carbonate (ν_2 and ν_4). For the calcined AU series these correspond to a band at 703 and split band around 837 cm^{-1}. A third feature of the AU series at 1058 cm^{-1} can be attributed to a symmetric stretching vibration of carbonate (ν_1), which is expected for malachite samples at 1085 cm^{-1} according to literature.[25] The calcined ZM series on the other hand only displayed a band 820 cm^{-1}. Below 600 cm^{-1} the rise of a broad feature was observed for both series, which could be attributed to the vibrations of the M-O skeleton.[26]

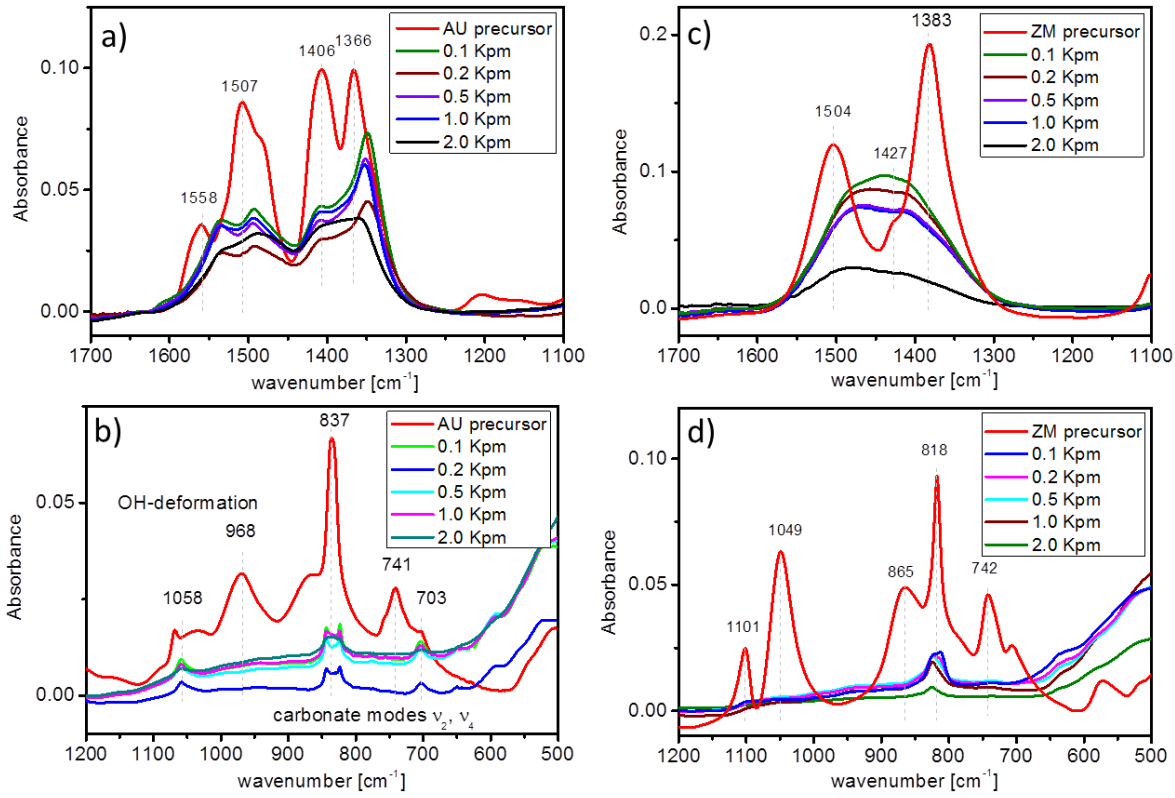

Figure 3.5: IR spectra of calcination series a) and b) AU samples and c) and d) ZM samples.

N_2O-chemisorption capacities varied in a range of 220-270 μmol g^{-1} and 160-230 μmol g^{-1} for the AU-red and ZM-red sample series, respectively (see Table 3.2). That would corre-

spond to Cu-SA of 18-22 m^2/g and 13-19 m^2/g, if the reaction of N_2O only with Cu-surface atoms could be assumed with a stoichiometry of 1:2. There was no unique relationship of the N_2O capacity with the heating ramp of the samples, but it seemed there was a weak trend pointing to a lower N_2O-capacity for the samples with higher HT-CO_3 content and lower heating ramp. This is slightly counter intuitive as usually a smaller crystallite domain size is expected to yield a higher surface area. This could be a hint that there is a stronger embedment of the Cu particles in the slowly calcined samples. On the other hand, this could also be a result of the higher carbonate content in the samples with lower heating rates, diluting the amount of Cu in the reactor when loading it with a certain amount of calcined sample. However, this effect can only account for a fraction of the trend, as the mass difference is only about 5 % between samples with highest and lowest heating rate, but the differences in N_2O-capacity are about 20-30 %.

Table 3.2: N_2O-capacities and BET surface areas of calcination series

Heating rate	**AU**		**ZM**	
	N_2O-capacity (Cu-SA_{N2O})	**BET-SA**	**N_2O-capacity (Cu-SA_{N2O})**	**BET-SA**
[Kpm]	[μmol^{-1}]([$m^2\,g^{-1}$])	[$m^2\,g^{-1}$]	[μmol^{-1}]([$m^2\,g^{-1}$])	[$m^2\,g^{-1}$]
0.1	218 (18)	30	183 (15)	58
0.2	228 (19)	60±1	164 (13)	51
0.5	261 (21)	80±4	199 (16)	58
1	267 (22)	98	233 (19)	68
2	255 (21)	60±10	222 (18)	82

Activity in methanol synthesis from a 6 % CO / 8 % CO_2 syngas mixture was measured at 30 bar and 503 K (see Figure 3.6). The ZM derived catalysts started showing a high activity of more than 300 $\mu mol\,min^{-1}\,g_{cat}{}^{-1}$ in methanol synthesis. AU derived catalysts started with lower activities between 260 and 300 $\mu mol\,min^{-1}\,g_{cat}{}^{-1}$. A strong deactivation was observed in the first two hours of methanol synthesis. Afterwards a nearly linear deactivation proceeded. For ZM the deactivation proceeded much more rapidly, therefore after 17 h time on stream, activities between 200 and 220 $\mu mol\,min^{-1}\,gcat^{-1}$ were found for both sample series. The observed differences between the least and most active catalysts were then smaller than 10%. There was a weak apparent trend of the activity data (per mass of calcined catalyst), which showed that the samples with slower heating rate were less active, despite their lower crystallinity with smaller domain sizes. So no beneficial effect of a large amount of HT-CO_3 for the catalytic activity in methanol synthesis was

observed. The trend already observed for the N_2O-capacities within each sample series reflects the same trend, although the relative differences in N_2O-capacities were bigger than the differences observed in activity. This trend is reversed when normalizing the activity to the mass of the reduced catalyst (see Figure S.3.2 in section 3.8). As the samples contain different amounts of HT-CO_3, which is released during reduction, the amount of reduced catalyst in the reactor is slightly different for the samples with different heating rates. The higher activity of the ZM series at the very beginning of methanol synthesis cannot be explained by a higher N_2O-capacity as this value was generally lower compared to the AU series. This is another indicator that the N_2O-capacity is not a precise parameter for the activity in methanol synthesis when comparing different catalyst families.[27] Additionally, the rWGS seems to have different active sites than methanol synthesis, as in our previous rWGS study (see chapter 2) the AU derived catalysts were more active in rWGS than the ZM derived catalysts. The faster deactivation of ZM derived samples during catalysis can be explained by a less efficient separation of the Cu particles by ZnO due to the lower content of ZnO in the ZM samples compared to the AU samples.

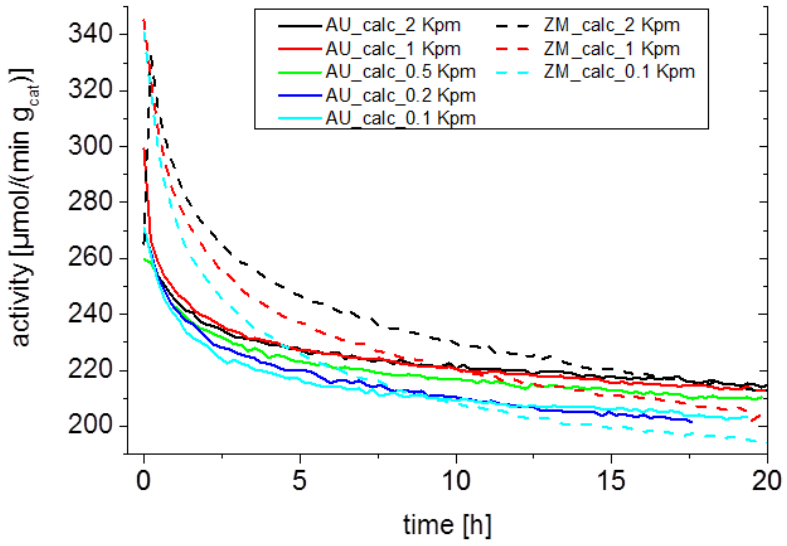

Figure 3.6: Activity of AU_calc_x (solid line) and ZM_calc_x (dotted line) in methanol synthesis at 503 K and 30 bar.

3.5 Conclusion

By varying the heating ramp during calcination, the amount of HT-CO_3 could be adjusted in calcined catalysts prepared from both ZM and AU precursors. Presence of large amounts of HT-CO_3 indicated that no significant segregation and crystallization of CuO and ZnO took place, in line with previous reports associating the HT-CO_3 with a large Cu/Zn interface.[2,10] Residual carbonates after calcination can affect the microstructure and defectivity of the final Cu particles by kinetic hindrance of their crystallization during the reduction. However despite distinct changes in crystallinity, decomposition profile and IR absorption, the differences of the catalytic activity in methanol synthesis were small and did not reveal a beneficial effect of a high HT-CO_3 content. On the contrary, dilution of the active Cu by carbonate, led to a decrease of activity in methanol synthesis per g of calcined catalyst. The different precursor phases AU and ZM yielded catalysts with very similar activities in methanol synthesis after 15 h TOS. Although ZM derived catalysts started with a higher activity, a faster deactivation was observed for the ZM samples and led to matching activities of both series after some reaction time.

3.6 Acknowledgements

The authors thank Maike Hashagen for BET analyses and Jasmin Allan for XRD and TG measurements.

3.7 References

[1] J. B. Hansen, P. E. H. Nielsen, *Handbook of Heterogeneous Catalysis*, chapter Methanol Synthesis, Wiley-VCH, Weinheim, 2nd Edition, **2008**, pp. 2920–2944.

[2] B. Bems, M. Schur, A. Dassenoy, H. Junkes, D. Herein, R. Schlögl, *Chem. Eur. J.* **2003**, *9*, 2039.

[3] C. Baltes, S. Vukojevic, F. Schüth, *J. Catal.* **2008**, *258*, 334.

[4] G. J. Millar, I. H. Holm, P. J. R. Uwins, J. Drennan, *J. Chem. Soc., Faraday Trans.* **1998**, *94*, 593.

[5] D. Waller, D. Stirling, F. S. Stone, M. S. Spencer, *Faraday Discuss. Chem. Soc.* **1989**, *87*, 107.

[6] P. Kowalik, M. Konkol, K. Antoniak, W. Próchniak, P. Wiercioch, *J. Molec. Catal. A: Chem.* **2014**, *392*, 127.

[7] M. Behrens, S. Zander, P. Kurr, N. Jacobsen, J. Senker, G. Koch, T. Ressler, R. W. Fischer, R. Schlögl, *J. Am. Chem. Soc.* **2013**, *135*, 6061.

[8] M. Behrens, R. Schlögl, *Z. anorg. allg. Chem.* **2013**, 2683.

[9] S. Fujita, S. Moribe, Y. Kanamori, M. Kakudate, N. Takezawa, *Appl. Catal., A* **2001**, *207*, 121.

[10] M. Schur, B. Bems, A. Dassenoy, I. Kasatkin, J. Urban, H. Wilmes, O. Hinrichsen, M. Muhler, R. Schlögl, *Angew. Chem. Int. Ed.* **2003**, *42*, 3815.

[11] N. Koga, J. Criado, H. Tanaka, *Thermochim. Acta* **1999**, *341*, 387.

[12] A. Tarasov, J. Schumann, F. Girgsdies, N. Thomas, M. Behrens, *Thermochim. Acta* **2014**, *591*, 1.

[13] S. Fujita, S. Moribe, Y. Kanamori, N. Takezawa, *React. Kinet. Catal. Lett.* **2000**, *70*, 11.

[14] M. Behrens, *J. Catal.* **2009**, *267*, 24.

[15] A. Coelho, *TOPAS: General Profile and Structure Analysis Software for Powder Diffraction Data; Bruker AXS GmbH: Karlsruhe, Germany* **2006**, *version 3.0*.

[16] I. Arkhangelsky, A. Dunaev, I. Makarenko, N. Tikhonov, S. Belyaev, A. Tarasov, *Non-Isothermal Kinetic Methods*, Edition Open Access, Berlin, **2013**.

[17] J. Opfermann, *J. Therm. Anal. Calorim.* **2000**, *60*, 641.

[18] S. Brunauer, P. H. Emmett, E. Teller, *J. Am. Chem. Soc.* **1938**, *60*, 309.

[19] E. P. Barrett, L. G. Joyner, P. P. Halenda, *J. Am. Chem. Soc.* **1951**, *73*, 373.

[20] G. Chinchen, P. Denny, D. Parker, M. Spencer, D. Whan, *Appl. Catal.* **1987**, *30*, 333.

[21] N. A. Tikhonov, I. V. Arkhangelsky, S. S. Belyaev, A. T. Matveev, *Thermochim. Acta* **2009**, *486*, 66.

[22] M. Reading, D. Dollimore, *Thermochim. Acta* **1994**, 117.

[23] M. Behrens, F. Girgsdies, A. Trunschke, R. Schlögl, *Eur. J. Inorg. Chem.* **2009**, *2009*, 1347.

[24] B. Reddy, R. Frost, A. Locke, *Transition Met. Chem.* **2008**, *33*, 331.

[25] M. Schmidt, H. Lutz, *Physics and Chemistry of Minerals* **1993**, *20*, 27.

[26] J. Goldsmith, S. D. Ross, *Spectrochim. Acta A* **1968**, *24*, 2131.

[27] O. Martin, J. Perez-Ramirez, *Catal. Sci. Technol.* **2013**, *3*, 3343.

3.8 Supporting information

Content:

- Additional characterization
- FHI internal sample numbers

Characterization

BET

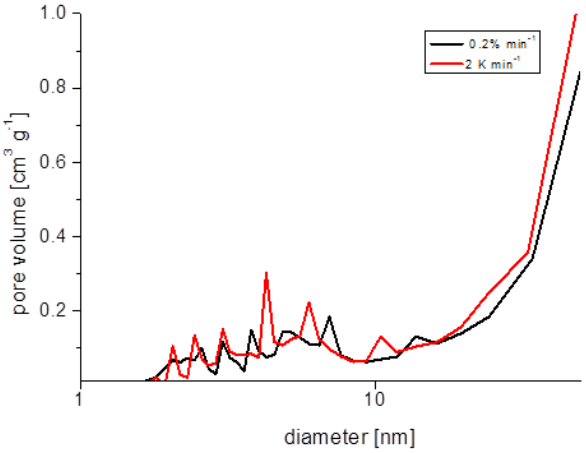

Figure S.3.1: Pore size distribution of AU_calc_2 Kpm (red line) and AU calcined in thermobalance with constant weight loss (black line).

XRD

XRD pattern of the calcined samples were fitted using background order 3, and preferential orientation order 4 for the CuO phase.

Table S.3.1: Domain sizes of calcined AU and ZM.

Calcination cond.	AU		ZM	
	CuO domain size [nm]	ZnO domain size [nm]	CuO domain size [nm]	ZnO domain size [nm]
Static conditions	4.6	5.8	6.0	5.7
2 Kpm	2.1	3.6	3.2	-
1 Kpm	-	-	3.2	-
0.5 kpm	-	-	3.2	-
0.2 kpm	-	-	3.0	-
0.1 kpm	-	-	2.6	-

Activity

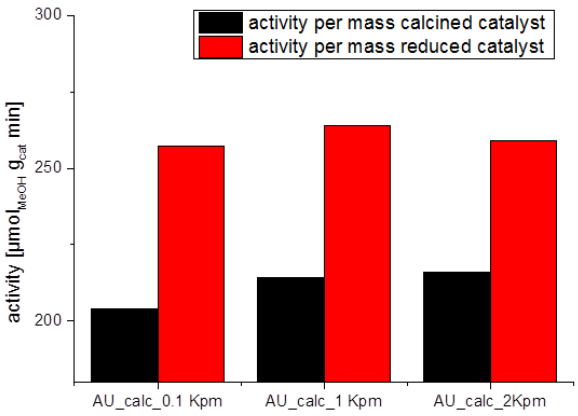

Figure S.3.2: Activity of AU_calc_X normalized per mass of catalysts before reduction (black) and in reduced state (red).

Internal sample numbers

For future reference please refer to the following sample numbers.

Table S.3.2: Internal sample numbers

Precursor	**Calc. sample**	**calc. T**	**heating ramp**	**sample mass**	**#**
ZM (#12716)	ZM_calc_0.1	603 K	0.1 Kpm	0.75 g	14415
	ZM_calc_0.2	603 K	0.2 Kpm	0.75 g	14407
	ZM_calc_0.5	603 K	0.5 Kpm	0.75 g	14391
	ZM_calc_1	603 K	1 Kpm	0.75 g	14397
	ZM_calc_2	603 K	2 Kpm	0.75 g	14429
	ZM_calc_static	603 K	2 Kpm	static conditions	12717
AU (#12630)	AU_calc_0.1	603 K	0.1 Kpm	0.75 g	14100
	AU_calc_0.2	603 K	0.2 Kpm	0.75 g	14274
	AU_calc_0.5	603 K	0.5 Kpm	0.75 g	14279
	AU_calc_1	603 K	1 Kpm	0.75 g	14284
	AU_calc_2	603 K	2 Kpm	0.75 g	14307
	AU_calc_static	603 K	2 Kpm	static conditions	12631

4 The role of the promoter and the influence of calcination temperature for different precursor structures of Cu/Zn based catalysts for methanol synthesis

Julia Schumann, Andrey Tarasov, Robert Schlögl and Malte Behrens

4.1 Abstract

Zincian malachite and aurichalcite precursor phases of Cu/Zn based catalysts for methanol synthesis were investigated. A special focus was put on the effect of Al-promotion on the two precursor compounds. The main effects were morphology alteration resulting in higher surface areas independent of the precursor phase and stabilization of the high-temperature carbonate (HT-CO_3). By varying the calcination temperature of the promoted samples it could be shown that a high amount of high-temperature carbonate (HT-CO_3) led also to a higher amount of oxygen vacancies in the ZnO phase of the catalysts. However, no direct correlations between oxygen vacancies or HT-CO_3 content and activity in methanol synthesis were found. A strong stabilization effect of a small Al amount was found for catalysts prepared from both precursor systems. The deactivation constant decreases by a factor of 10 for power law models applied for the first 10-24 h TOS. The intrinsic activity increases by a factor of 30 to 40 % upon promotion with Al. The activation energy on the other hand is not changed upon promotion.

4.2 Introduction

Methanol is one of the most important bulk chemicals with a growing global demand exceeding 60 million tons in 2013.[1] Its synthesis is performed over $Cu/ZnO/Al_2O_3$ catalysts. The industrially well-established catalyst preparation by co-precipitation leads to a precursor system with a complex phase mixture[2] containing hydroxy-carbonates such as malachite [$Cu_2CO_3(OH)_2$], zincian malachite [$(Cu,Zn)_2CO_3(OH)_2$] (ZM), aurichalcite [$(Cu,Zn)_5(CO_3)_2(OH)_6$] (AU) and hydrotalcite-like phases. The main component of the precursor used in industry is ZM, which was previously identified to be the most desirable precursor, leading to the most active catalysts in methanol synthesis.[3] There is a strong influence of the parameters of early steps in the catalyst synthesis on the activity of the final catalyst, as reported in numerous studies.[2,4–8] A lot of this "black magic" of the catalyst preparation can nowadays be understood and is explained by the formation of the "right" precursor phase with its beneficial microstructure.[9] E.g., a higher zinc ratio in the precursor, than the usually employed 30:70 or 1:2 ratio with respect to Cu, was deemed unfavorable, because it would lead to segregation of Cu and Zn into different phases, hence reducing the optimal mixing between the two metal oxide components in the calcined state of the catalyst.[3] Also many other aspects of the empirically developed multi-step catalyst synthesis like pH-value, temperature and ageing time are now chemically rationalized.[9] But the question, why zincian malachite and not a pure aurichalcite precursor phase should be the best way to prepare highly active catalysts, has not been answered so far. Another question, which was not answered satisfactorily so far concerns the role of the aluminium promoter. It is known, that alumina stabilizes the Cu-catalyst,[10] but recent results also point to an additional electronic promoter effect of the ZnO.[11], [a] The exact role is not yet fully understood. With the recently published surface characterization method H_2-transient adsorption (H_2-TA)[12], which allows the discrimination of metallic Cu sites and oxygen vacancies of the ZnO_x-overlayer as opposed to the N_2O-RFC method used so far for Cu-surface characterization,[12,13] we hope to gain new insight into the promotional effect of Al and a better understanding of what is important for an active methanol synthesis catalyst.

The aim of this study is to investigate the influence of the Al promoter on the properties and catalytic performance of catalysts derived from ZM and AU precursors, which differ in their Cu/Zn-ratio. A concentration of 3 % Al was previously identified as the optimal promoter concentration for ZM[8] and was therefore used in this study. The effect of Al

[a] see also chapter 6

promotion on phase pure ZM and AU is compared in order to shed light on the reason for the different opinions existing about the best precursor phase for methanol synthesis or rWGS. The dominant precursor phase in the industrial system was identified to be ZM,[3] but many academic groups use AU-derived catalysts and found them to be most active.[14] Also our own recent work showed that for the reverse water-gas shift reaction (rWGS) in the case of binary model type precursors, the ZM derived catalysts were not superior over the AU counterpart, on the contrary, aurichalcite displayed both higher BET and copper surface area (Cu-SA), resulting in higher rWGS activity of the ex-AU catalysts (see chapter 2).

In this work we present detailed characterization of the Al promoted and unpromoted ZM and AU precursors. Furthermore, we discuss the characterization of the calcined catalysts as well as activity data for methanol synthesis. Additionally the influence of calcination temperature on the promoted ZM:Al and AU:Al catalysts was investigated.

4.3 Experimental

4.3.1 Sample preparation

Cu/Zn (Al) precursors were prepared by pH-controlled co-precipitation[3] in an automated laboratory reactor (LabMax from Mettler-Toledo). The proper amount of $Cu(NO_3)_2 \cdot 3\,H_2O$, $Zn(NO_3)_2 \cdot 6\,H_2O$ and in case of the promoted samples $Al(NO_3)_3 \cdot 9\,H_2O$ were dissolved in Millipore water and 15 ml of concentrated HNO_3 to obtain 600 mL of a 1 M solution of the metal salts. This solution was added to the reactor containing 400 mL of water at a constant rate of 20 mL min^{-1}. (The ZM:Al sample was prepared in a bigger batch size as described in Ref[15], called FHI-prec therein). The proper amount of Na_2CO_3 solution (1.6 M) was automatically added to keep the pH constant at 6.5, for the AU:Al sample the pH was adjusted to 9. The precipitation temperature was 338 K. Precipitation was followed by ageing for 1 h (338 K, pH=6.5), once the turbidity started to increase. The solid was then filter-collected and washed several times by re-dispersion in water until the conductivity of the washing medium was below 0.5 mS cm^{-1}. Approximately 40 g of the solid hydroxy-carbonate precursors were obtained by spray drying. All samples were calcined in a rotating furnace, (turn number of 3, tube diameter 40 mm and length of sample bed 300 mm) with a flow of 125 mL min^{-1} in 20 % O_2 in Ar. For the calcination study of the binary samples, 0.75 g of the precursor powder were calcined at a maximum temperature of 603 K and a dwell time of 180 min, only the heating rates were varied between 0.1 and

2 K min^{-1}. The ternary samples were calcined in batches of 3 g (unless stated otherwise), using a heating ramp of 2 K min^{-1} and temperatures of 603 - 793 K.

4.3.2 Characterization methods

X-ray diffraction (XRD) data were collected using a STOE STADI P transmission diffractometer equipped with a primary focusing Ge monochromator (Cu $K_{\alpha 1}$ radiation) and a linear position sensitive detector (moving mode, step size 0.5°, counting time 30 s/step). The samples were mounted in the form of a clamped sandwich of small amounts of powder fixed with a small amount of grease between two layers of thin polyacetate film. The phase composition was determined by full pattern refinement in the 2θ range 4-80° according to the Rietveld method using the TOPAS software[16] and crystal structure data from the ICSD database. Summarized refinement parameters are displayed in the Supplementary Information (SI). X-ray fluorescence spectroscopy (XRF) was performed in a Bruker S4 Pioneer X-ray spectrometer. Scanning electron microscopy (SEM) images were taken on a Hitachi S-4800 field emission gun (FEG) system. Thermogravimetric analysis (TG/DSC) was performed on a Netzsch STA449 Jupiter thermoanalyzer (10 K min^{-1}, 100 NmL min^{-1} 21 % O_2 in Ar). Evolution of the gas phase during reaction was monitored with a quadrupole mass spectrometer (Pfeiffer, QMS200 Omnistar). The kinetic data obtained in the TG experiments were processed using Netzsch software and are presented elsewhere.[17] The Thermokinetics program package was used for processing kinetic dependences and for component kinetic analysis. The NETZSCH Procedure is described in Ref.[18,19] Temperature programmed reduction (TPR) of the calcined sample was performed in a fixed bed reactor (TPDRO-1100, CE instruments), in 5 vol% H_2 in argon at a heating rate of 6 K min^{-1} (80 mL min^{-1}, end temperature 573 K, holding time 30 min). The H_2 consumption was monitored with a thermal conductivity detector (TCD). IR spectra of precursors and calcined samples were recorded using an ATR Vario 670 spectrometer, equipped with an MCT detector and diamond as ATR crystal. No pretreatment of the powdered samples was performed. The aperture was set to 0.5 cm^{-1} and the resolution was 4 cm^{-1}. Spectra were recorded using 64 scans. Specific surface areas were determined by N_2 physisorption using the BET method[20] in a Quantachrome Autosorb-1 machine. Prior to analysis, the samples have been degassed for 2 h at 353 K. The mesopore size distribution and pore volume were calculated according to Barrett, Joyner and Halenda modified Kelvin equation.[21] N_2O chemisorption capacity was determined using reactive frontal chromatography (RFC).[22] Approx. 100 mg of calcined sample (100-200 μm parti-

cle size) was placed in a fixed bed reactor. After in-situ reduction, the sample was cooled down in the reducing gas to room temperature, purged with He and then switched to 10 mL min^{-1} of a 1 % N_2O in He mixture. The N_2O chemisorption capacity and resulting Cu surface area (Cu-SA_{N2O}) were calculated from the MS signal of the N_2 trace (m/z =28). Apparent Cu-SA_{N2O} were calculated assuming a stoichiometry of N_2: Cu 1:2, according to the surface reaction $N_2O + 2\,Cu \longrightarrow Cu_2O + N_2$ and an average surface density of $1.47 \cdot 10^{19}$ Cu-atoms per m^2. Recently it was proven, that N_2O also reacts with oxygen vacancies as present in partially reduced ZnO_x.[12,13] H_2-transient adsorption (TA) was performed in the same setup that was used for N_2O-RFC as described in Ref.[12] For approx. 100 mg of sample, H_2-TA was recorded at room temperature in 20 mL min^{-1}, 5 % H_2 in Ar for one hour each, for the calcined sample (CuO), the reduced sample (Cu) and the sample after N_2O-RFC (Cu_2O) (see Figure 4.1) after thorough purging in Argon. Under the assumption that no H_2 is adsorbed on CuO, the difference of the areas between Cu and CuO and between Cu_2O and CuO were calculated and the amount of consumed H_2 was quantified with the help of reference measurements (TPR of CuO).

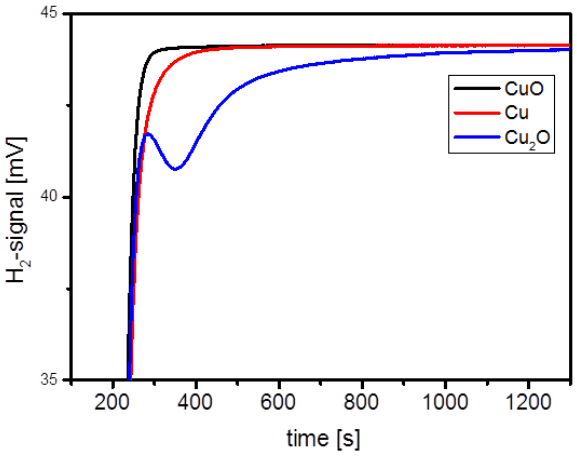

Figure 4.1: H_2-TA measurement of the calcined sample (black line), reduced sample (red line) and sample after N_2O-RFC (blue line).

4.3.3 Catalytic measurements

Methanol synthesis from syngas was tested in a fixed bed flow reactor. 50 mg (100-200 μm particle diameter, diluted with 0.7 g of SiO_2) were loaded into a 6 mm inner diameter stainless steel reactor tube using a bed volume of 1.7 mL, which resulted in a GHSV of

3500 h^{-1}. The catalyst was reduced at 523 K (1 K min^{-1}) for 1.5 hours in 20 % H_2 in Ar. Upon completion of the reduction, the reactor was cooled to 503 K, a syngas mixture with a composition of 6 % CO, 8 % CO_2, 59 % H_2 and balance Ar was introduced into the reactor, and the pressure was raised to 30 bars. Online analysis of products was performed with a gas chromatograph (Agilent 7890A). Methanol synthesis was performed under differential conditions (< 4 % conversion). Activation energies were determined in the temperature range 463 - 523 K.

4.4 Results and discussion

4.4.1 Precursor characterization

Four different precursors were prepared by co-precipitation at constant pH. The preparation protocols of all 4 precursors are shown in Figure S.4.1 in section 4.8. The target precursor structures were ZM, with a high Cu/Zn ratio of 70/30 or 80/20 and AU, with a lower Cu/Zn ratio of 40/60. Each structure was prepared once in the binary form, and once with nominal 3 % Al as promoter, therefore the samples are named ZM, ZM:Al, AU and AU:Al respectively. XRF analysis showed that the nominal composition was close to the actual values in the obtained precipitates (see Table 4.1). Binary ZM was obtained with a Cu/Zn ratio of 80/20, the ternary with 70/28 and slightly less Al than intended, according to XRF with 1.5 instead of 3 % Al. Binary AU was obtained with Cu/Zn ratio of 41/59. AU:Al was obtained with a Cu/Zn ratio of 40/60 with additional 2 % Al. The XRD pattern proved that phase-pure precursor structures were obtained (see Figure 4.2). The ZM derives from the malachite structure, which is the pure copper hydroxy carbonate $Cu_2(OH)_2CO_3$. Upon substitution of Cu with Zn the structure slightly contracts in an anisotropic manner leading to a shift of the d($20\bar{1}$) position.[23,24] The linear relationship of the d($20\bar{1}$) value and the metal composition was used to confirm the full incorporation of the Zn ion into the (zincian) malachite structure. For the binary ZM sample the value of d($20\bar{1}$) of 2.790 Å corresponded to approximately 79 % Cu in cationic positions (for calculation and results of Rietveld refinement refer to Table S.4.1 in section 4.8). For the promoted sample a very high substitution value of Cu by Zn could be achieved without the formation of aurichalcite byphase. A d($20\bar{1}$) value of 2.758 Å, as observed for ZM:Al, corresponds to 70.4 % Cu in cationic positions. It was not possible to achieve such a high substitution level in phase pure ZM for the binary system. Attempts to prepare a binary sample with a Cu/Zn ration of 70/30 do not yield the phase-pure ZM, but usually contain AU as a

by-phase.[4,9,23] For this reason the Cu/Zn ratio of the binary sample was chosen higher with 80/20. Only 3 % Al influence the ZM phase such, that a higher zinc incorporation into the structure becomes favorable. Additionally the XRD peaks of the promoted ZM:Al are significantly broadened. Using a Rietveld-fit this broadening was calculated to be a result decrease of the crystallite size (see Table 4.1). The crystallite size was more than halved from 18 to 7 nm. For the AU samples a proper Rietveld-fit was not possible due to strong anisotropic peak broadening. Therefore the peaks from the PDF-database are shown as reference, which are in an acceptable agreement with the obtained pattern. As for the ZM samples, also for AU the Al promotion led to a significant peak broadening and decrease of crystallinity (see Figure 4.2b and Table 4.1).

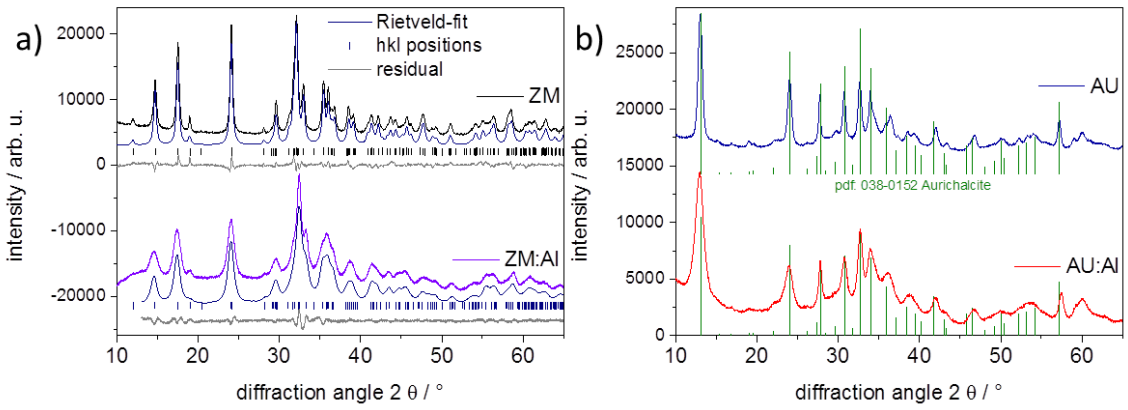

Figure 4.2: XRD pattern of a) zincian malachite and b) aurichalcite precursors.

Table 4.1: Table 1: Precursor characterization.

	XRD domain size [nm]	XRF Cu/Zn/Al [mol %]	BET [$m^2\,g^{-1}$]
AU	11.2 ± 0.1[a]	41/59	55
ZM	17.69 ± 0.08	80/20	43
ZM:Al (FHI-std)	7.26 ± 0.03	70/28/2	122
AU:Al	5.54 ± 0.04[a]	39/58/2[b]	109

[a]estimated from approximated Rietveld fits
[b]indications of small Na contaminations from XRF

The morphology of the precursor samples was investigated using SEM (see Figure 4.3). The AU phase consisted of thin platelets or sheets (Figure 4.3c, d). The Al promoter did not change the morphology significantly, although it is apparent that the dimensions of

the particles decreased, in line with the results from XRD. The morphology of the ZM changed more, rather short, thick rods turned into longer thin needles upon Al promotion. Both binary precursors gained a lot of BET-surface area (SA) upon Al promotion: the SA of AU was doubled and that of ZM nearly tripled in size (see Table 4.1).

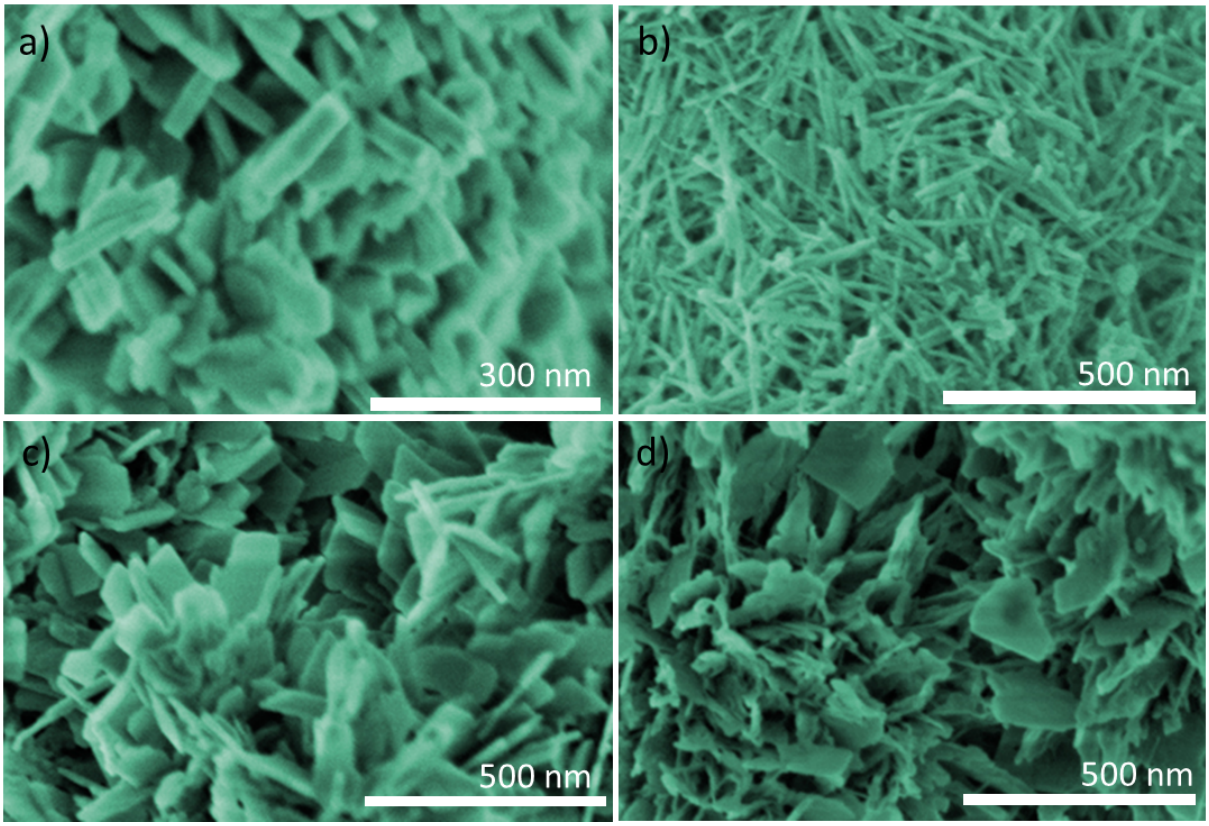

Figure 4.3: SEM images of a) ZM, b) ZM:Al, c) AU and d) AU:Al Precursors.

Thermogravimetric (TG) measurements show, that the decomposition of Cu,Zn hydroxycarbonates during calcination proceeds in two main steps: After the desorption of surface water and carbon dioxide up to 400 K, H_2O and CO_2 are released simultaneously in a first decomposition step. In a second step above 623 K only CO_2 is released.[4] The intermediate is therefore termed "high temperature carbonate" (HT-CO_3).[25] About 20 % of the mass loss upon calcination was associated with the desorption of surface species and the first decomposition step (see Figure 4.4). Another 6 to 8 %, for AU lower than for ZM respectively, were due to the decomposition of HT-CO_3. The amount of the total mass loss was not significantly changed upon promotion of the respective phase with Al, but the stability of the different stages did change. The binary samples displayed higher stability at temperatures below 650 K in the TG. Only above 650 K the promoted samples seemed

to be more stable. The difference between AU and AU:Al was rather small, in contrast ZM:Al showed a significantly higher stability of the intermediate HT-CO_3 than the binary ZM.

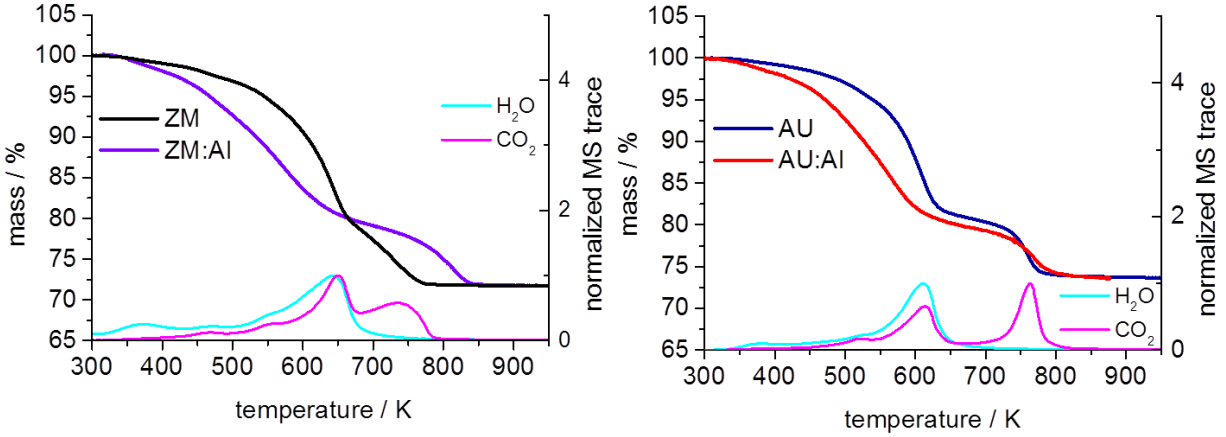

Figure 4.4: TG-MS curves of precursors at dynamic atmosphere 100 NmL min^{-1} 21 % O_2 in Ar, with 10 Kpm. For clarity only MS curves of binary samples are shown.

4.4.2 Characterization of calcined samples

Binary and promoted ZM and AU samples were compared after calcination at 603 K. From a previous study it was known that the binary ZM and AU sample show very sensitive behavior with respect to the calcination conditions.(see chapter 3) Relatively small batches of 0.75 g of ZM and AU were therefore used for calcination. In order to investigate the influence of different calcination conditions on the promoted samples, a similar study was performed with ZM:Al. The response of different calcination batch sizes with constant gas flow is presented in section 4.8. The promoted sample proved to be much less sensitive towards humidity in the gas phase. As a result we chose batch sizes of 3 g for the following study to compare promoted with the binary samples. The promoted ZM:Al and AU:Al precursors were additionally calcined at 693 and 793 K. The samples will be referred to as ZM(:Al)_X and AU(:Al)_X, with X corresponding to the calcination temperature 603 K, 693 K or 793 K in Kelvin. Calcination at 603 K yielded for both ZM:Al and AU:Al fairly amorphous materials as shown by X-ray diffraction (see Figure 4.5). The unpromoted samples were much more crystalline after calcination under even milder conditions (smaller batch size). Even a 90 K higher calcination temperature for the promoted samples, still

yielded less crystalline oxides. The pattern of ZM:Al_693 was dominated by broad CuO signals, with an estimated domain size of 2 nm. The residual curve still showed weak peaks that seemed similar to the near amorphous phase present in the ZM:Al_603 sample. Only after calcination at 793 K crystallinity of CuO and ZnO was higher than that of ZM_603 with calculated domain sizes of around 7 nm and 5 nm, respectively (see Figure 4.5a and Table 4.2). On the other hand, the XRD pattern of AU:Al_693 was dominated by ZnO and showed only very weak and broad CuO signals resulting in domain sizes of around 5 and 2 nm. Calcination up to 793 K caused the features in the pattern to sharpen and yielded domain sizes between 6 and 7 nm (see Figure 4.5b and Table 4.2).

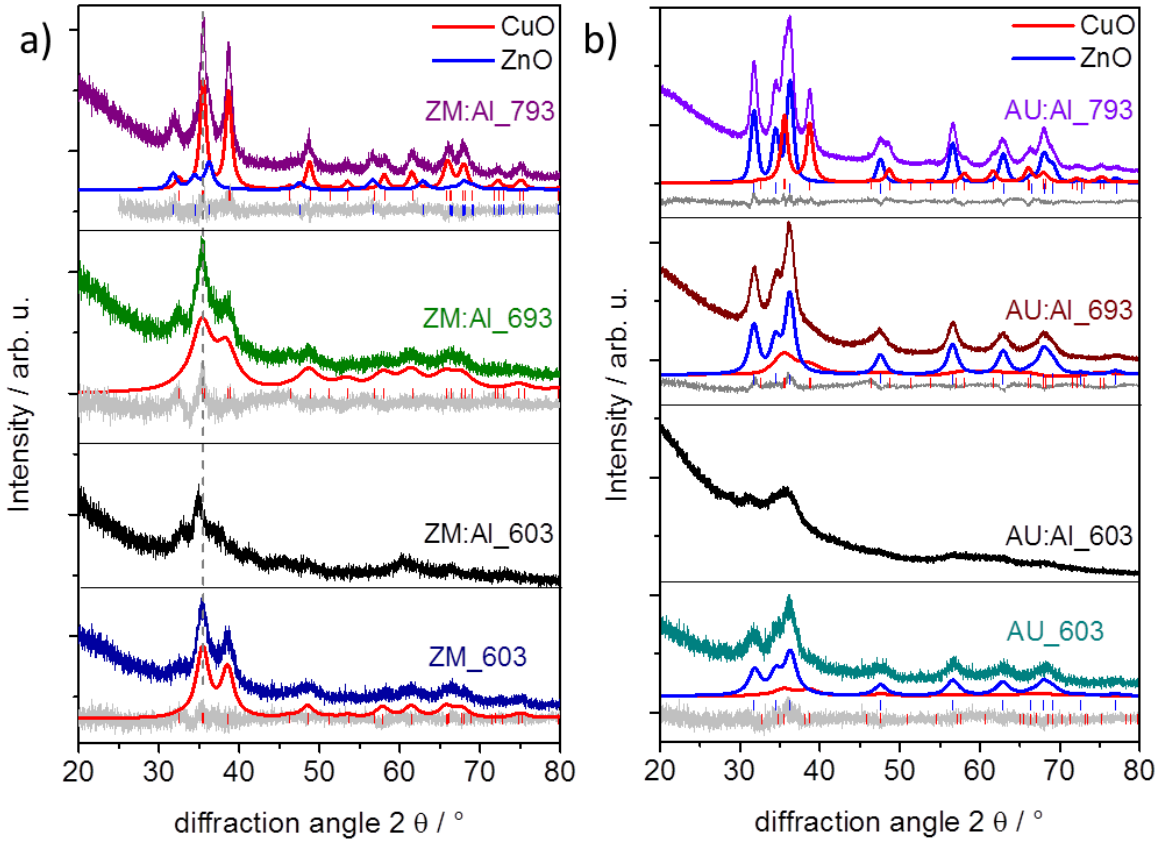

Figure 4.5: XRD pattern of a) ZM_603 and ZM:Al_X and b) AU_603 and AU:Al_X after calcination at different temperatures.

As assumed from the differences of the precursor phases, the unpromoted samples showed smaller BET-SA compared to the promoted ones, although the differences were much smaller (Table 4.2). With increasing calcination temperature the specific SA of the pro-

moted samples decreased (see Table 4.2). Thereby the SA of AU:Al_X are bigger (119 - 70 $m^2 g^{-1}$) than those of ZM:Al_X (96 - 64 $m^2 g^{-1}$), respectively. This was not expected as the order was the other way around for the precursors: ZM:Al with a BET-SA of 122 $m^2 g^{-1}$ vs. AU:Al with 109 $m^2 g^{-1}$. With increasing calcination temperature the difference got less. TG measurements showed that the amount of HT-CO_3 in the calcined samples was higher for the promoted samples than for the unpromoted ones. Additionally the decomposition was earlier and the fraction of species decomposing at temperature below 600 K was larger for unpromoted ZM_603 and AU_603 (Figure 4.6). With increasing calcination temperature the amount of HT-CO_3 decreased, as could be expected. ZM:Al_603 had the highest amount of HT-CO_3 (corresponding to a sample weight loss of 10.1 %), and after calcination at 793 K no more HT-CO_3 species were present. AU:Al_603 contained less HT-CO_3 in agreement with the difference seen in the precursors. As for the ZM:Al series, AU:Al_693 contains significantly less HT-CO_3 and upon calcination at 793 K temperature, AU:Al_793 did not contain significant amounts of HT-CO_3.

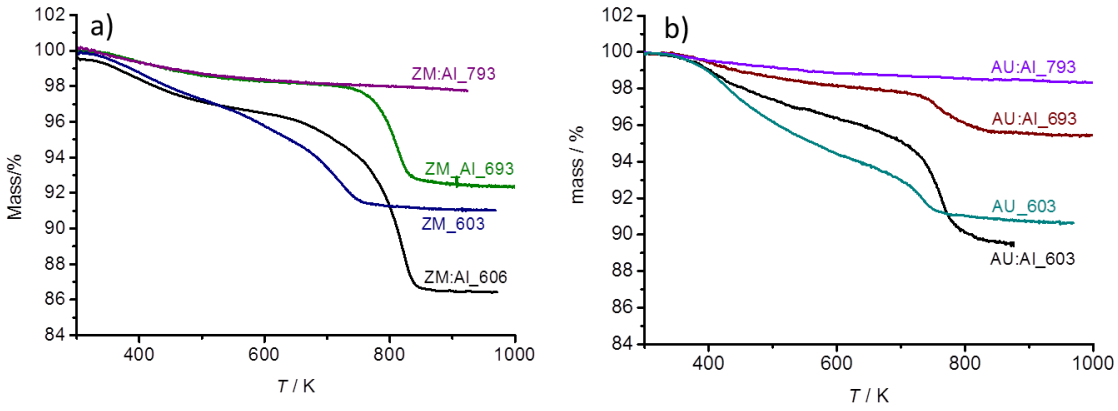

Figure 4.6: TG curves of calcined catalysts a) ZM_603 and ZM:Al_X and b) AU_603 and AU:Al_X.

For a deeper insight in to the carbonate structure of the calcined samples IR spectroscopy was employed. The results of the binary samples are already shown in chapter 3, selected regions of the IR spectra of the Al promoted samples are shown in Figure 4.7. As a comparison also the precursors ZM:Al and AU:Al were investigated. Both promoted precursors were very similar to the unpromoted ZM and AU precursors, respectively and are therefore also in good agreement with the published data of the synthetic zincian malachite and aurichalcite phases.[6,25,26] The small amount of trivalent promoter Al^{3+} did not seem to cause any changes in the vibrational spectra of the carbonate and hydroxyl groups

Table 4.2: Characterization of calcined binary catalysts and promoted catalysts with different calcination temperatures.

	CuO domain size [nm]	**ZnO domain size [nm]**	**HT-CO3 [%]**	**BET-SA [$m^2 g^{-1}$]**	**CuO-content measured by TPR [%]**
ZM_603	3.2	-	3	82	76
ZM:Al_603	-	-	10.1	96	61
ZM:Al_693	1.9	-	5.8	85	66
ZM:Al_793	6.7	5.2	0.4	64	71
AU_603	2.1	3.6	3	60 ± 10	38
AU:Al_603	-	1.4	6.0	119	36
AU:Al_693	1.5	4.7	2.3	112	37
AU:Al_793	6.3	6.9	0.2	70	38

of the precursor. The spectra of the samples after calcination on the other hand showed stronger differences. Despite the high intensity in the region of the asymmetric stretching vibration of the carbonate compared to the precursors, the fine structure got lost and only broad features could be observed for the samples with the lower calcination temperatures. Between 603 and 693 K only intensity of the signals decreased, but no shift of the peaks was observed. After calcination at 793 K the carbonate vibrations were only very weak (in the region 1200 -1700 cm^{-1}) or completely vanished (837 or 818 cm^{-1}). Below 650 cm^{-1} a steep increase of intensity was observed in all calcined samples, which was ascribed to the metal-oxygen skeleton vibrations.[27] A shoulder around 600 cm^{-1} seemed to be specific for the samples calcined at 793 K.

TPR profiles yielded insights into the reduction process of CuO to Cu metal. Reduction peak maxima ranged from 481 K for AU:Al_603 to 496 K for ZM:Al_793, that means they varied in a quite narrow range (see Figure 4.8). A trend was observed for samples with higher calcination temperature giving rise to higher reduction peak temperatures. Thereby the change of the profile between 603 K and 693 K calcination temperature was very small and more pronounced for the highest calcination temperature 793 K, for both sample series ZM:Al and AU:Al. Although the samples calcined at 793 K displayed the highest reduction peak maximum temperatures, the onset temperature was lowest. ZM:Al_603, ZM:Al_693 and ZM:Al_793 were all reduced at slightly higher temperatures compared to the respective AU:Al sample. The slow rise of H_2-consumption at low-temperatures is

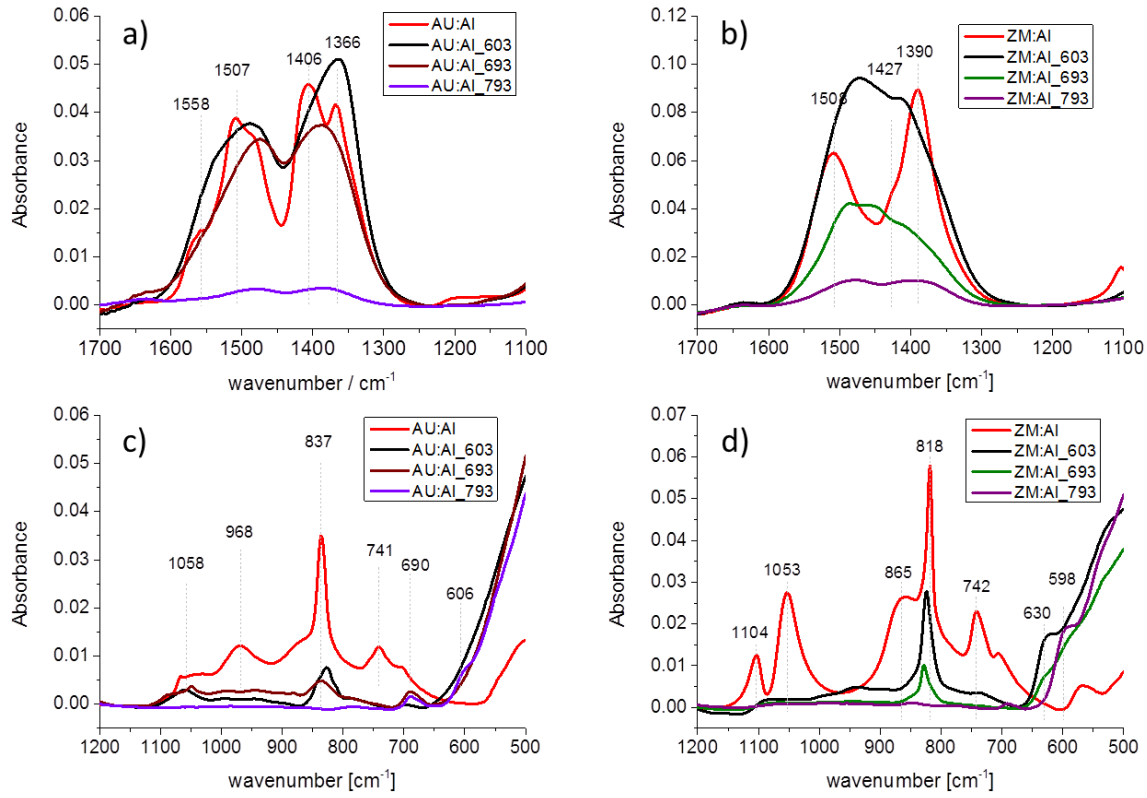

Figure 4.7: IR spectra of AU:Al series (a,c) and ZM:Al series (b,d)

ascribed to the first step of the reduction of CuO to Cu metal via a Cu(I) intermediate in the literature.[15,28] It seems as reported earlier, that HT-CO_3 species lead to a slight retardation of the reduction,[15] as both samples without any HT-CO3 (ZM:Al_793 and AU:Al_793) show a lower onset temperature of the reduction process. Other explanations suggested for the low temperature shoulder of the reduction signal, as the reduction of residual hydroxy carbonate species[29] or the reduction of highly dispersed or amorphous CuO-species,[29,30] could be ruled out because the investigated samples contained very different amounts of residual HT-CO_3 and differences in crystallinity and domain sizes of Cu, but there was little or no change observed in the low temperature shoulder. The main reduction signal was observed in a temperature region often reported for the reduction of CuO particles.[28–31] The small shift of the position of the main signal towards higher temperatures can be related to the slightly increasing crystallinity for the samples calcined at higher temperatures.

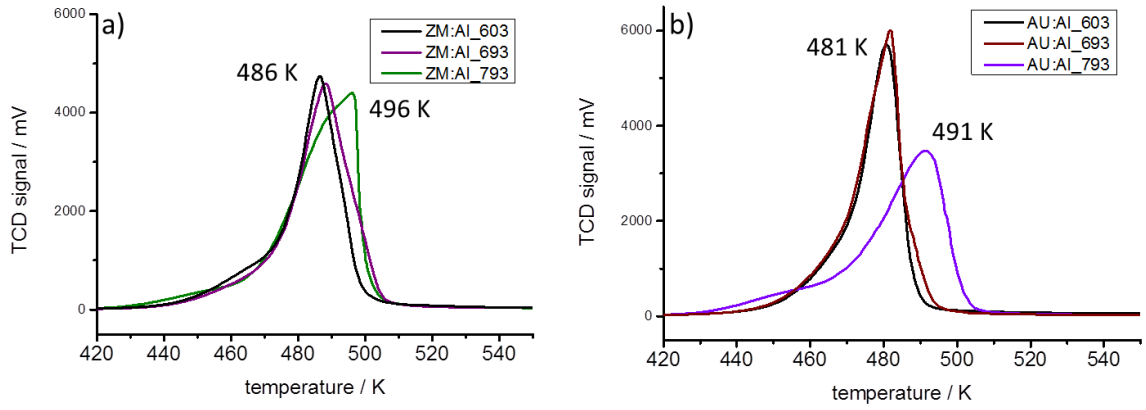

Figure 4.8: TPR profiles of a) ZM:Al_calc and b) AU:Al_calc.

After reduction up to 523 K, when all Cu^0 was converted to metallic Cu, the surface was characterized by two different methods. N_2O reactive frontal chromatography (N_2O-RFC)[22] yielded the N_2O-chemisorption capacity. Using this methods values from 470-225 μmol g^{-1} for ZM(:Al)_X and 330-160 μmol g^{-1} for AU(:Al)_X were obtained, with decreasing values for increasing calcination temperature and lowest values for the binary samples (with the exception of AU:Al_793, see Table 4.3). Upon Al promotion of ZM the N_2O-capacity nearly doubles and that of AU still increases by approximately 30 %. Recently it has been published, that these values represent a sum of Cu-SA and oxygen vacancies of ZnO.[12,13] That is why we have given the N_2O-chemisorption capacity and put the theoretical calculated Cu-SA_{N2O} values only in brackets. An alternative method probing

Table 4.3: Surface characterization of reduced catalysts.

	N_2O-capacity [μmol g^{-1}] (**Cu-SA_{N2O}** [m^2 g^{-1}])	**Cu-$SA_{H2\text{-}TA}$** [m^2 g^{-1}] (μmol g^{-1})	**Oxygen vacancies** [μmol/g]
ZM_603	225 (18.5)[a]	10.3 (126)	99
ZM:Al_603	473 (38.7)	16.4 (200)	273
ZM:Al_693	426 (34.9)	18.4 (225)	201
ZM:Al_793	239 (19.6)	12.3 (150)	89
AU_603	255 (20.9)[a]	12.4 (151)	104
AU:Al_603	330 (27.1)	12.3 (150)	180
AU:Al_693	317 (26.0)	13.3 (162)	155
AU:Al_793	161 (13.2)	9.8 (120)	41

[a]A decrease of 2 m^2 g^{-1} Cu-SA_{N2O} within the first week after calcination was observed for the binary ZM_603 and AU_603 sample. Given are the equilibrated values after 1 week.

the metallic Cu-SA is hydrogen temperature programmed desorption (H_2-TPD),[32] as was shown by comparative measurement with ZnO free samples.[13] A presumably proportional value is obtained by hydrogen transient adsorption (H_2-TA),[12] where after a N_2O-RFC measurement selectively only the Cu(I)-surface oxide is reduced back to the metal at room temperature. These values deviate from the N_2O consumption significantly. Using the H_2-TA method, Cu-SA between 18.4 and 10.3 m^2 g^{-1} were obtained for the ZM(:Al)_X series and 13.3 to 9.8 m^2 g^{-1} for AU(:Al)_X (Table 4.3). For both unpromoted samples the lowest value of each series, approx. 10 m^2 g^{-1} was obtained (with the exception of AU:Al_793). No longer did the increasing calcination temperature lead to a continuous decrease of the Cu-$SA_{H2\text{-}TA}$, but in fact a calcination temperature of 693 K led to the highest Cu-SA for both precursor systems. These results lead to the conclusion that a significant fraction of the measured high N_2O-capacity was due to the reaction of N_2O with oxygen vacancies in ZnO. The amount of oxygen vacancies decreased with increasing calcination temperature. Especially between 603 and 693 K the decrease of oxygen vacancies was significant, as the Cu-$SA_{H2\text{-}TA}$ even increased. This could be explained either by a less covered Cu-surface, or by the higher Cu content per calcined mass in the sample with the lower HT-CO_3 content (Table 4.2). The smallest difference between Cu-SA_{N2O} and Cu-$SA_{H2\text{-}TA}$ existed for the samples of both series with the highest calcination temperature, indicating a low amount of vacancies. From the TG measurements (Figure 4.6) it was shown that those two samples also did not contain any HT-CO_3, suggesting a relationship between HT-CO_3 and oxygen

vacancies in the resulting ZnO (Figure 4.9). This could also explain the finding of other authors, that a high HT-CO_3 content is responsible for a high Cu-SA_{N2O},[7] as the N_2O-RFC method is the most common method to determine Cu-SA, but in reality they mean the N_2O-capacity which represents a sum of oxygen vacancies of ZnO and Cu-SA.

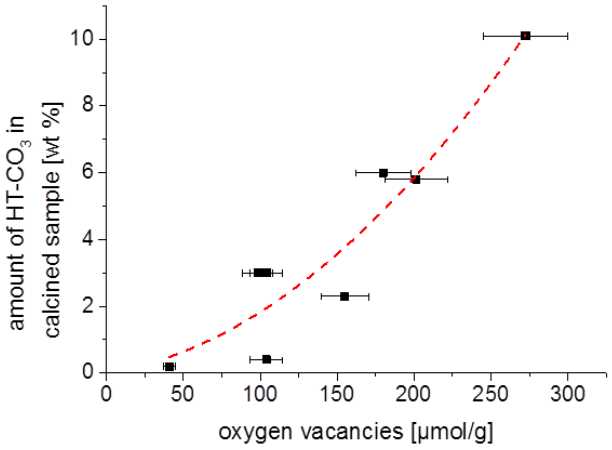

Figure 4.9: Relationship between the amount of HT-CO_3 and oxygen vacancies of the ZnO component after reduction, determined from the difference between Cu-SA_{N2O} and Cu-$SA_{H2\text{-}TA}$.

4.4.3 Activity tests

All eight catalysts were tested in methanol synthesis at 30 bar. The activities per mass of calcined catalyst at 503 K versus time on stream (TOS) are shown in Figure 4.10. In both series the samples calcined at 603 K and 693 K were very similar in activity, and the sample calcined at 793 K was significantly less active, about 20 %. The binary ZM_603 and AU_603 catalysts were least active, as could be expected from their model type character and low Cu-SA. The differences between the unpromoted samples were only small and equalized after few hours TOS, whereas all promoted ZM:Al_X samples were more active than any of the AU:Al_X series. Activation energies were around 53 kJ mol^{-1} ± 3 kJ mol^{-1} for all catalysts indicating that the type of active site did not change, only the number of active sites led to different activities.

What on the other hand differed remarkably, was the deactivation behaviour of the samples. Several reasons for deactivation of copper catalysts in methanol synthesis have been discussed in literature so far, most often sintering and poisoning.[10] Recently also

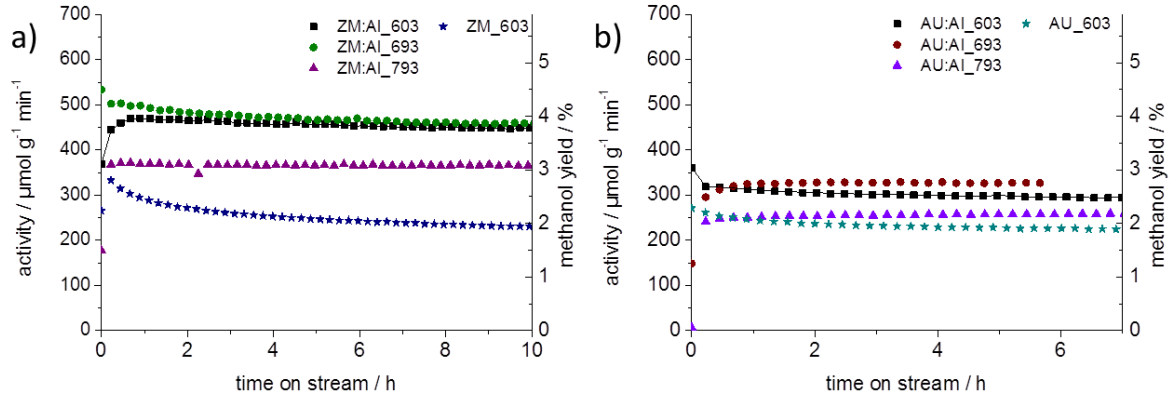

Figure 4.10: Activity in methanol synthesis at 503 K and 30 bar vs. time on stream (TOS) of a) ZM:Al_X and ZM_603 and b) AU:Al_X and AU_603.

loss of SMSI was discussed as a reason for deactivation. A comprehensive longterm deactivation study on several industrial-like catalysts revealed local depletion of ZnO and crystallisation of ZnO as well as $ZnAl_2O_4$ as one major deactivation pathway, despite their much higher Tamman temperature (T_{Tamman}^{ZnO}=1160 K), compared to copper (T_{Tamman}^{Cu}=670 K).[33,34] In the literature a power law model (PLM) was often used to describe the deactivation of copper catalysts by sintering.[35]

$$\frac{da}{dt} = -k * a^n \tag{4.1}$$

Deactivation orders of 1 to 16 have been reported, usually higher orders at the initial phase of deactivation and lower after the initial phase.[36] In order to model the deactivation relative activities $a_{rel} = \frac{a(t)}{a(0)}$ were calculated (Figure 4.11). To model the deactivation of the ZM_603 sample within the first 24 h TOS, a deactivation order n of 10 had to be used (Table 4.4). This agrees reasonably well with the assumption of sintering as main deactivation mechanism and seems plausible when considering the high copper content of this sample. ZM_603 is the catalyst with the strongest deactivation, nearly 40 % within the first 24 h TOS. The other binary sample, AU_603 has a much slower deactivation, only about 20 % within the first 24 h TOS. But the order n is much higher with 23, meaning that the slope of the deactivation is steeper in the beginning and then levels out quickly. The high reaction order cannot be explained by pure sintering but should be the result of a different deactivation mechanism. This suggestion seems feasible due to the much higher ZnO content in the AU_603 sample compared to the ZM_603 sample, which should enable

a much better separation of the Cu particles and make sintering less likely. We propose this is an indication for the main deactivation mechanism beeing the decrease of SMSI. The promotion with small amounts of Al stabilized the catalysts strongly. Although the ZM:Al_603 and _693 samples could still be fitted with a deactivation order n=10, they fit less good, seen at the smaller R^2 value. Nevertheless the deactivation constant k decreased strongly, by more than one order of magnitude and the catalysts showed a much slower deactivation. It is very interesting to note, that the sample ZM:Al_603, is despite the very high activity and similar compared to ZM:Al_693, much more stable within the studied time frame. Only sample ZM:Al_793, which was calcined a much higher temperature and also is significantly less active, is more stable than ZM:Al_603. For the ZM:Al_693 catalyst a model with a reaction order of n=23 fits much better indicating that here, sintering is much less probable the dominant deactivation mechanism. The same reaction order was used to fit the zinc richer AU:Al_603 sample. For AU the same was observed as for the ZM samples, promotion with small amount of Al decreased the deactivation constant k by more than one order of magnitude. The AU:Al samples prepared with higher calcination temperatures even showed an induction period with an increas in activity during the first hours TOS, so they could not be fitted by a simple PLM.

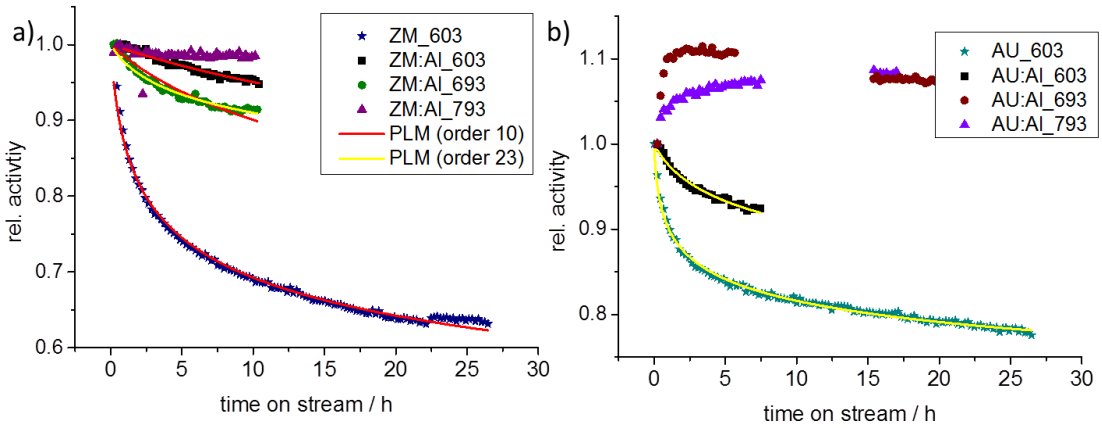

Figure 4.11: Deactivation of catalysts, relative activity ($a_{rel}(t) = \frac{a(t)}{a(0)}$) vs. TOS with fit according to power law model.

Strangely, upon calculation of the intrinsic activity for the samples with increasing calcination temperature an increase of intrinsic activity was observed, if the activity was normalized to the N_2O-capacity (see Figure 4.12, black columns). This is somewhat counter intuitive, as it is expected, that defects, associated with high activity, should decrease with

Table 4.4: Results of power rate law model fit for deactivation.

	Order of deactivation	Deactivation constant	R^2
ZM_603	10	0.29	0.99
ZM:Al_603	10	0.006	0.95
ZM:Al_693	10	0.017	0.92
	23	0.032	0.97
AU_603	23	0.39	0.99
AU:Al_603	23	0.032	0.98

higher calcination temperature. If however, the intrinsic activity was calculated using the Cu-$SA_{H2\text{-}TA}$, the intrinsic activities were more similar for especially the promoted samples, within the margin of error (see Figure 4.12, red columns). The unpromoted samples were now a bit lower in intrinsic activity, which might be due to the strong deactivation within the first 10 h TOS. This led to the conclusion that, in agreement with the results obtained for binary catalysts in the previous chapter, the HT-CO_3 is not the origin or booster of catalytic active sites. Because of the very high number of oxygen vacancies in ZnO, the Cu-SA, which is gernerally regarded as a value proportional to the number of active sites, was strongly overestimated by the N_2O-RFC method in ZM:Al_603 and ZM:Al_693 compared to ZM:Al_793 and analogous for AU:Al. A high number of oxygen vacancies in ZnO alone does not seem important for a high activity. That can also explain the already previously observed effect, that Al promoted samples despite their high absolute activity, show a very similar or even decreased intrinsic activity (normalized by Cu-SA_{N2O}) compared to unpromoted catalysts.[8] The intrinsic activity normalized by Cu-$SA_{H2\text{-}TA}$, on the other hand, showed a strong increase upon promotion as was intuitively expected. The density of active sites per Cu-$SA_{H2\text{-}TA}$ was the same for all promoted catalysts, independent from their precursor phase and calcination temperature within the studied range.

4.5 Summary and conclusions

Zincian malachite (ZM) and Aurichalcite (AU) precursors with different Cu/Zn ratios were each prepared without and with 3% of Al promoter. For both precursor phases a significant increase in surface area and decrease of crystallite size was observed upon promotion, proving that already small amounts of Al act as an efficient structural promoter, disturbing large crystallite growth. Promotion with 3% Al led also to a significant stabilization of

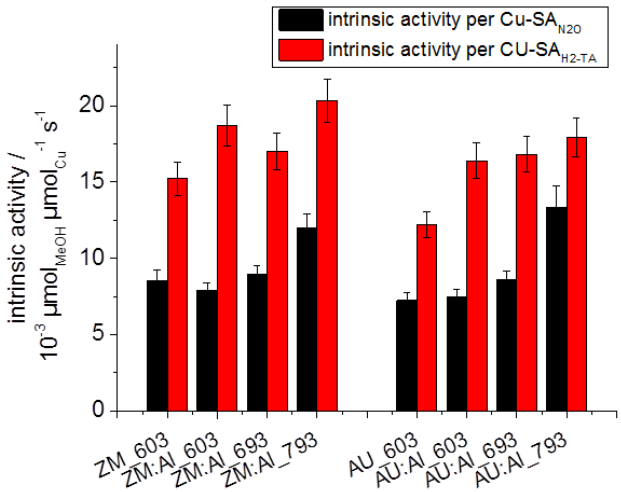

Figure 4.12: Different intrinsic activities after 7-10 h TOS in methanol synthesis at 503 K and 30 bar calculated from N_2O chemisorption (black bars) and H_2-TA (red bars).

HT-CO_3 and thus to a restraint of crystallization during the calcination procedure. In the unpromoted samples a significant amount of HT-CO_3 already decomposed upon mild calcination conditions at 603 K, whereas calcination of the promoted samples at 603 K led to conservation of the HT-CO_3, if a sufficiently small batch size was used. After calcination at 793 K negligible HT-CO_3 was present in both AU:Al_793 and ZM:Al_793 samples. It could be shown that within the two sample series with different calcination temperatures the activity in methanol synthesis was not proportional to the Cu-SA_{N2O} (measured by N_2O-RFC), which also includes the oxygen vacancies in ZnO, but rather proportional to the number of sites measured by the H_2-TA method introduced by Kuld et al.[12] To conclude, the amount of HT-CO_3 in the calcined sample did not lead to a high intrinsic activity in methanol synthesis but it acted as a structural stabilizer, leading to high surface areas and resulted in a high number of oxygen vacancies in the ZnO component of the catalysts. With this result we do not want to question the earlier observation that precursors with high amounts of HT-CO_3 give active catalysts. This does only mean that there is no direct need for HT-CO_3 in the calcined or active catalyst, but on the other hand the amount of HT-CO_3 in the calcined catalysts is a good probe for mild calcination conditions ensuring no strong sintering due to high water content in the atmosphere during calcination. (see chapter 3) Al promotion seemed more effective for ZM derived samples leading to much more active catalysts, compared to AU, which is probably the reason for the reported superiority of ZM precursor phase. Where the deactivation of ZM_603 followed a 10th order power law

model (PLM) in agreement with sintering behavior as described in literature,[10] the other samples were closer to a 23rd order deactivation within the first 10-20 h TOS, assumed to derive from a decrease of SMSI. Stability during methanol synthesis increased by an order of magnitude upon promotion with small amounts of Al for catalysts derived from both ZM and AU and is assumed to derive from Al doping of ZnO keeping the ZnO in the slightly reduced state with a high Cu/Zn interface and preventing it from dewetting and recrystallization. Activities normalized by Cu-SA were comparable for both sample series, indicating that the differences originate only from the lower availability of Cu in the AU precursor.

4.6 Acknowledgements

The authors thank Nygil Thomas for the activity measurement of the binary catalysts, Stefanie Kühl and Elias Frei for the preparation of the AU:Al precursor, Jasmin Allan for XRD and TG measurements, Gisela Weinberg and Wiebke Frandsen for SEM measurements, Maike Hashagen for BET measurements and Frank Girgsdies for discussion. Matthias Fichtl is acknowledged for discussion of deactivation behavior.

4.7 References

[1] M. Bertau, H. Offermanns, L. Plass, F. Schmidt, H.-J. Wernicke, *Methanol:The Basic Chemical and Energy Feedstock of the Future*, Springer-Verlag, Berlin Heidelberg, **2014**.

[2] C. Baltes, S. Vukojevic, F. Schüth, *J. Catal.* **2008**, *258*, 334.

[3] M. Behrens, *J. Catal.* **2009**, *267*, 24.

[4] B. Bems, M. Schur, A. Dassenoy, H. Junkes, D. Herein, R. Schlögl, *Chem. Eur. J.* **2003**, *9*, 2039.

[5] G. J. Millar, I. H. Holm, P. J. R. Uwins, J. Drennan, *J. Chem. Soc., Faraday Trans.* **1998**, *94*, 593.

[6] D. Waller, D. Stirling, F. S. Stone, M. S. Spencer, *Faraday Discuss. Chem. Soc.* **1989**, *87*, 107.

[7] P. Kowalik, M. Konkol, K. Antoniak, W. Próchniak, P. Wiercioch, *J. Molec. Catal. A: Chem.* **2014**, *392*, 127.

[8] M. Behrens, S. Zander, P. Kurr, N. Jacobsen, J. Senker, G. Koch, T. Ressler, R. W. Fischer, R. Schlögl, *J. Am. Chem. Soc.* **2013**, *135*, 6061.

[9] M. Behrens, R. Schlögl, *Z. anorg. allg. Chem.* **2013**, 2683.

[10] J. B. Hansen, P. E. H. Nielsen, *Handbook of Heterogeneous Catalysis*, chapter Methanol Synthesis, Wiley-VCH, Weinheim, 2nd Edition, **2008**, pp. 2920–2944.

[11] M. Behrens, G. Lolli, N. Muratova, I. Kasatkin, M. Hävecker, R. N. d'Alnoncourt, O. Storcheva, K. Kohler, M. Muhler, R. Schlögl, *Phys. Chem. Chem. Phys.* **2013**, *15*, 1374.

[12] S. Kuld, C. Conradsen, P. G. Moses, I. Chorkendorff, J. Sehested, *Angew. Chem. Int. Ed.* **2014**, *53*, 5941.

[13] M. B. Fichtl, J. Schumann, I. Kasatkin, N. Jacobsen, M. Behrens, R. Schlögl, M. Muhler, O. Hinrichsen, *Angew. Chem. Int. Ed.* **2014**, *53*, 7043.

[14] T. Fujitani, J. Nakamura, *Catal. Lett.* **1998**, *56*, 119.

[15] J. Schumann, T. Lunkenbein, A. Tarasov, N. Thomas, R. Schlögl, M. Behrens, *ChemCatChem* **2014**, *6*, 2889.

[16] A. Coelho, *TOPAS: General Profile and Structure Analysis Software for Powder Diffraction Data; Bruker AXS GmbH: Karlsruhe, Germany* **2006**, *version 3.0*.

[17] A. Tarasov, J. Schumann, F. Girgsdies, N. Thomas, M. Behrens, *Thermochim. Acta* **2014**, *591*, 1.

[18] I. Arkhangelsky, A. Dunaev, I. Makarenko, N. Tikhonov, S. Belyaev, A. Tarasov, *Non-Isothermal Kinetic Methods*, Edition Open Access, Berlin, **2013**.

[19] J. Opfermann, *J. Therm. Anal. Calorim.* **2000**, *60*, 641.

[20] S. Brunauer, P. H. Emmett, E. Teller, *J. Am. Chem. Soc.* **1938**, *60*, 309.

[21] E. P. Barrett, L. G. Joyner, P. P. Halenda, *J. Am. Chem. Soc.* **1951**, *73*, 373.

[22] G. Chinchen, C. Hay, H. Vandervell, K. Waugh, *J. Catal.* **1987**, *103*, 79.

[23] M. Behrens, F. Girgsdies, *Z. anorg. allg. Chem.* **2010**, *636*, 919.

[24] P. Porta, S. De Rossi, G. Ferraris, M. Lo Jacono, G. Minelli, G. Moretti, *J. Catal.* **1988**, *109*, 367.

[25] M. Behrens, F. Girgsdies, A. Trunschke, R. Schlögl, *Eur. J. Inorg. Chem.* **2009**, *2009*, 1347.

[26] B. Reddy, R. Frost, A. Locke, *Transition Met. Chem.* **2008**, *33*, 331.

[27] J. Goldsmith, S. D. Ross, *Spectrochim. Acta A* **1968**, *24*, 2131.

[28] S. Kühl, A. Tarasov, S. Zander, I. Kasatkin, M. Behrens, *Chem. Eur. J.* **2014**, *20*, 3782.

[29] J. P. Breen, J. R. Ross, *Catal. Today* **1999**, *51*, 521.

[30] M. Shimokawabe, H. Asakawa, N. Takezawa, *Appl. Catal.* **1990**, *59*, 45.

[31] J. Sloczynski, R. Grabowski, A. Kozlowska, P. K. Olszewski, J. Stoch, *Phys. Chem. Chem. Phys.* **2003**, *5*, 4631.

[32] M. Muhler, L. P. Nielsen, E. Tornqvist, B. S. Clausen, H. Topsoe, *Catal. Lett.* **1992**, *14*, 241.

[33] M. B. Fichtl, D. Schlereth, N. Jacobsen, I. Kasatkin, J. Schumann, M. Behrens, R. Schlögl, K.-O. Hinrichsen, Kinetics of deactivation on cu/zno/al2o3 methanol synthesis catalysts, submitted to Appl. Catal. A.

[34] M. B. Fichtl, J. Schumann, N. Jacobsen, W. Busser, I. Kasatkin, F. Girgsdies, S. Zander, M. Muhler, M. Behrens, R. Schlögl, K.-O. Hinrichsen, Deactivation mechanisms on cu/zno/al2o3 methanol synthesis catalysts, unpublished results.

[35] I. Lovik, *Modelling, Estimation and Optimization of the Methanol Synthesis with Catalyst Deactivation.*, PhD thesis, Department of Chemical Engenieering, Norwegian University of Science and Technology, **2001**.

[36] M. Sahibzada, D. Chadwick, I. S. Metcalfe, *Natural Gas Conversion Iv* **1997**, *107*, 29.

4.8 Supplementary information

Content:

- Preparation
- Results from Rietveld-fit of zincian malachite
- Calcination series of ZM:Al - variation of batch size
- Internal sample numbers

Preparation

The preparation protocols of the precursors are displayed in Figure S 1.

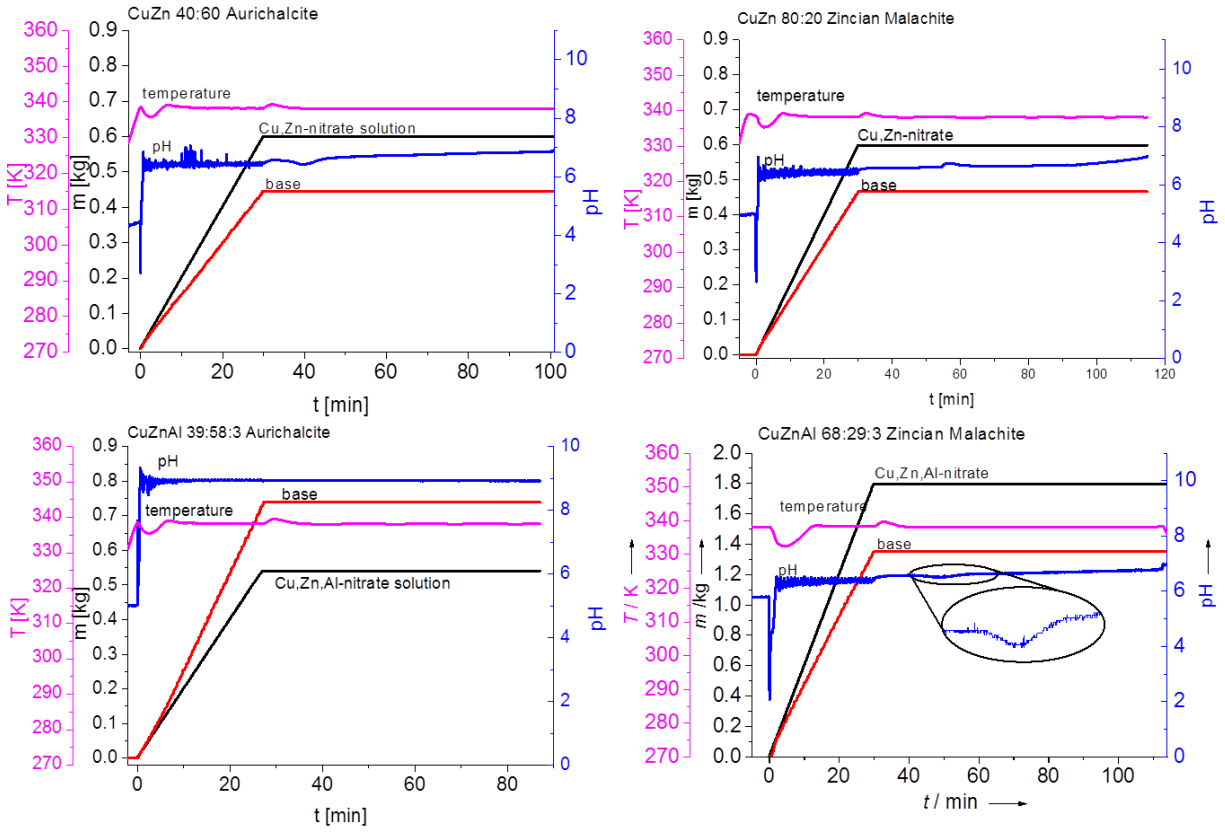

Figure S.4.1: Preparation protocols of labmax.

XRD

The amount of Cu on cationic positions in the zincian malachite structure was calculated according to the following formula: $Y=2.50752 + 0.00356 \cdot X$, with Y being the $d(20\bar{1})$ value and X the relative content of Cu atoms in the structure. This equation was determined from 4 phase pure (zincian) malachite structures with Cu/Zn ratios of 100/0 to 85/15 and verification of the Cu content by XRF.

Calcination series of promoted ZM

In order to compare the stability of the HT-CO_3 in the promoted samples with the binary samples a calcination series was prepared starting from the precursor ZM:Al. The gas flow/sample mass ratio during calcination was varied from 10 to 67 $mL\,min^{-1}\,g^{-1}$, corresponding to sample masses of 1.5 to 10 g in our setup. Thus, conditions were changed in a complementary manner as for the binary sample series reported in chapter 3 and

Table S.4.1: Parameters of Rietveld fit of zincian malachite.

	ZM	**ZM:Al**
Rwp	2.55	1.11
background order	3	3
spacegroup	P121/a1	P121/a1
preferred orientation	4	4
a [Å]	9.42402(58)	9.3917(11)
b[Å]	12.05554(71)	12.1087(15)
c [Å]	3.20215(14)	3.18275(25)
β [°]	96.9145(29)	96.0151(50)
d($20\bar{1}$)	2.790	2.758

different water levels in the atmosphere during calcination were realized. XRD and TG data showed that the stability of the HT-CO_3 was much higher in the promoted samples (see Figure S.4.2). After calcination of 1.5 g ZM:Al precursor (ZM:Al_calc_1.5 g) under mildest conditions (most comparable with the binary sample ZM_603), still the complete amount of around 9 % HT-CO_3 was present. No crystalline phase can be attributed to the diffraction pattern. The binary sample ZM_603 contained after similar or even milder calcination conditions only around 3 % HT-CO_3 and the resulting CuO was crystalline. Increasing the sample mass during calcination further, led to a continuous decrease of the residual carbonate and water content present in the calcined material. Above a batch size of 5 g also the HT-CO_3 content decreased, but even a 10 g batch size still yielded 6.5 % HT-CO_3 and the XRD-pattern did not show crystalline CuO or ZnO. As a comparison, a small batch size that was calcined under static conditions (ZM:Al_calc_static) contained only 2.5 % HT-CO_3 and crystalline CuO with a domain size of 3.1 nm (see Figure S.4.2). This showed the strong influence of a dry gas flow during calcination on the decomposition and the extent of crystallization. Never the less, the promoted sample showed a much higher resistance against decomposition of the HT-CO_3 and crystallization of the oxides compared to the unpromoted ZM samples. Consistent with the TG experiments, results were obtained from quantification of the temperature programmed reduction (TPR) signal. The amount of reduced CuO decreased with increasing HT-CO_3 content from 65.8 to 61.6 % CuO (see Table S.4.2). The Cu-SA of all the samples resulting from ZM:Al was very high (see Table S.4.2). Compared to the unpromoted samples, the value roughly doubled. But no clear trend was observed with respect to the HT-CO_3 content. This indicates competing effects influencing the Cu-SA. On the one hand a high amount of carbonate and water led to a slightly lower amount of Cu per calcined catalysts mass, which led to a lower Cu-SA (ZM:Al_calc_1.5g). On the other hand also a very high amount of CuO could be compensated by a higher crystallinity and particle size and could thus lead to a lower Cu-SA in the case of ZM:Al_calc_static. The samples in between show the highest Cu-SA values of 38-39 $m^2\,g^{-1}$ (see Table S.4.2).

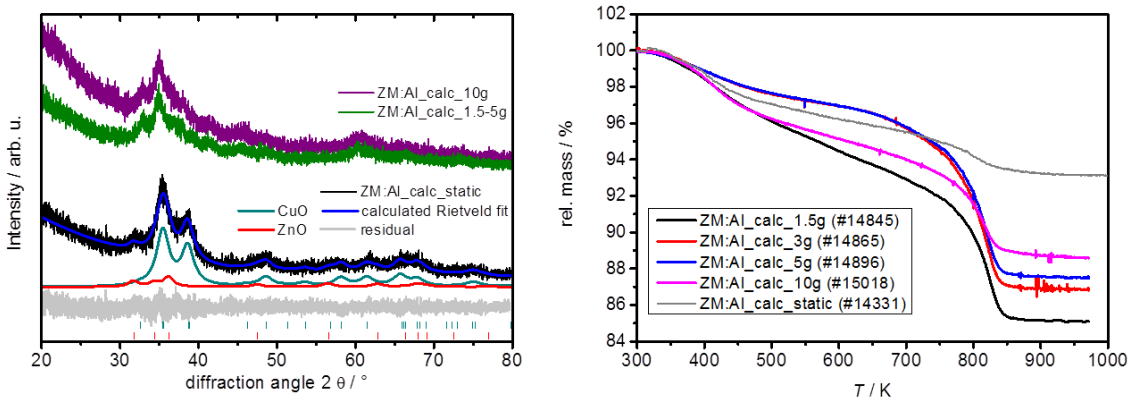

Figure S.4.2: XRD and TG data of ZM:Al_calc series calcined at 603 K.

Table S.4.2: Characterization data of ZM:Al_calc series.

Sample	**HT-CO_3 content [wt %]**	**BET-SA [$m^2\ g^{-1}$]**	**Cu-SA_{N2O} [$m^2\ g^{-1}$]**	**CuO-content [wt %]**
ZM:Al_calc_1.5g	9.2	n.a.	35.3	61.6
ZM:Al_calc_3g	10.0	96	38.7±1.1	62.0 ± 0.6
ZM:Al_calc_5g	9.4	n.a.	38.9	62.2
ZM:Al_calc_10g	6.5	118	37.6	64.2
ZM:Al_calc_static	2.5	107	34.1	65.8

Internal sample numbers

For future reference please refer to the following sample numbers.

Precursor	**Calc. sample**	**Calcination conditions**	**#**
ZM (#12716)	ZM_603	603 K / 2 Kpm / 0.75 g	14429, 19936
AU (#12630)	AU_603	603 K / 2 Kpm / 0.75 g	14307, 19937
ZM:Al (#14328)	ZM:Al_calc_1.5g	603 K / 2 Kpm / 1.5 g	14845
	ZM:Al_603/calc_3g	603 K / 2 Kpm / 3 g	14865
	ZM:Al_calc_5g	603 K / 2 Kpm / 5 g	15896
	ZM:Al_calc_10g	603 K/ 2 Kpm / 10 g	15018
	ZM:Al_693	693 K / 2 Kpm / 3 g	16070
	ZM:Al_793	793 K / 2 Kpm / 3 g	16136
AU:Al (#18147)	AU:Al_603	603 K / 2 Kpm / 3 g	18172
	AU:Al_693	693 K / 2 Kpm / 3 g	18302
	AU:Al_793	793 K/ 2 Kpm / 3 g	18335

5 Synthesis and Characterization of a Cu/ZnO based catalyst[a]

Julia Schumann, Thomas Lunkenbein, Andrey Tarasov, Nygil Thomas, Robert Schlögl and Malte Behrens

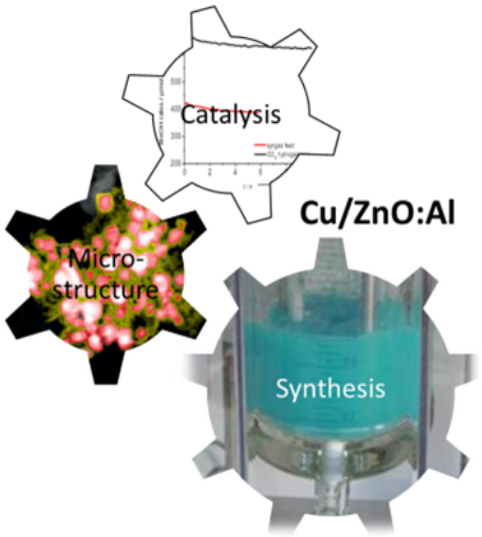

5.1 Abstract

We report the application of an optimised synthesis protocol of a Cu/ZnO:Al catalyst. The different stages of synthesis are all well-characterised by using various methods with regard to the (micro-)structural, textural, solid-state kinetic, defect and surface properties. The low amount of the Al promoter (3%) influences but does not generally change the phase evolution known for binary Cu/ZnO catalysts. Its main function seems to be the introduction of defect sites in ZnO by doping. These sites as well as the large Cu surface

[a]This chapter is already published and adapted from [1]

area are responsible for the large N_2O chemisorption capacity. Under reducing conditions, the Al promoter, just as Zn, is found enriched at the surface suggesting an active role in the strong metal–support interaction between Cu and ZnO:Al. The different stages of the synthesis are comprehensively analysed and found to be highly reproducible in the 100 g scale. The resulting catalyst is characterised by a uniform elemental distribution, small Cu particles (8 nm), a porous texture (pore size of approximately 25 nm), high specific surface area (approximately 120 m^2g^{-1}), a high amount of defects in the Cu phase and synergetic Cu–ZnO interaction. A high and stable performance was found in methanol synthesis. We wish to establish this complex but well-studied material as a benchmark system for Cu-based catalysts.

5.2 Introduction

$Cu/ZnO/Al_2O_3$ catalysts have been applied for nearly 50 years in methanol synthesis, a large-scale industrial process of still growing importance with a current demand of more than 60 million metric tons per year. Especially in the context of a sustainable future energy system, methanol produced from CO_2 and H_2 is believed to play a key role as an energy storage molecule.[2] Furthermore, Cu/ZnO-based catalysts are also active in the low-temperature water gas shift reaction and in the steam reforming of methanol.

Because of the multi-tasking ability of this class of catalysts, they are used in many applications and different scientific questions are currently studied based on Cu/ZnO-based materials. The range spans from investigations of reaction mechanisms[3–5] and metal-support interaction,[6–9] over catalyst stability[10] to new synthesis methods[11–14] and attempts to find alternatives to Cu/ZnO.[15–17] Usually, the progress made in the individual studies is well documented, but — as a general problem of catalysis research — a meaningful comparison of the model catalysts or newly developed materials of different reports is often rather difficult. This is a result of the various reaction conditions, reactor types, evaluation methods and benchmark systems used in the different laboratories.

The most reliable way to compare catalytic performances is still to run the samples under study against a well-characterised benchmark in the same reactor under identical reaction conditions. For Cu/ZnO-based catalysts, this is often achieved by comparison with commercially available catalysts or with a self-prepared “conventional” catalyst synthesised according to recipes available in the literature. Either of these methods works but is related to disadvantages. In the case of a commercial reference, the full structural

characterisation is often not disclosed that would allow for a better interpretation of the catalytic results and/or the catalytic performance is only presented in a semi-quantitative manner as normalised data.

A drawback of self-prepared catalysts is that the particular synthesis of $Cu/ZnO/(Al_2O_3)$ catalysts is very complex and highly sensitive to even small changes of the synthesis parameters.[18,19] The industrial catalyst is prepared by co-precipitation. The recipe with constant-pH co-precipitation, ageing, washing, drying and calcination has been developed and improved by empirical methods over the last decades and is in itself a subject of ongoing research. Unfortunately, its reproducibility and the comprehensive characterisation of the resulting samples require semi-automatic synthesis equipment and a variety of different analytical tools that is often not available in academic laboratories. Thus, there is the need for a fully characterised, reproducible catalyst as a reference material to reliably compare activity data. Over the last years our group has gained some experience in this particular catalyst synthesis and we have recently reported on the effects of co-precipitation temperature,[20] ageing pH,[21] Cu:Zn ratio[22] and the Al_2O_3 promoter.[23]

Herein, we present full details of an optimised synthesis recipe for a Cu/ZnO:Al catalyst, its reproducibility and provide a comprehensive characterisation of the physical properties and quantitative catalytic activity in methanol synthesis of the resulting material. We label the resulting Cu/ZnO:Al catalyst "FHI standard" as we intend to use it as a benchmark reference in our future work and encourage other groups to do the same in their studies. Therefore, we will provide aliquots of this catalyst free of charge to interested academic groups (see the Supporting Information). In the long term, we hope that this strategy does not only contribute to a better comparability of the results reported in the literature, but we also envision that feedback from the different laboratories will lead to an increasing pool of freely available reactivity data from different reactions and setups that might help to further unravel the last secrets of this complex composite catalyst.[24]

The FHI-standard precursor and its calcined and reduced stages will be abbreviated throughout this paper as FHI-prec, FHI-calc and FHI-red, respectively.

5.3 Results and discussion

Based on the result of previous studies,[22,23] the metal ratio of the best catalysts prepared in our laboratory was identified as Cu:Zn=70:30 with additional 3% of Al, resulting in an overall molar metal composition of 68:29:3 (Cu/Zn/Al). This composition aims at a high

substitution level of Zn in the zincian malachite precursor, $(Cu,Zn)_2(OH)_2CO_3$, to allow for an intimate mixing of Cu and ZnO particles in the reduced catalyst. Promotion by 3% of Al^{3+} was shown to structurally and electronically promote the catalyst most likely by effective doping of the ZnO:Al component.[23,25] The nominal metal composition was adjusted in the stock solution for the co-precipitation experiment, which was conducted three times in a 6 L reactor. The reactor was equipped with an automated pH feedback loop to adjust a constant pH during the co-precipitation process yielding 135 g of the catalyst precursor FHI-prec per batch.

In the following, the different steps of catalyst synthesis and characterisation will be described in detail based on a 6 L batch experiment. The reproduced experiments are reported in detail in the Supporting Information and are presented here only to highlight the reproducibility of the synthesis and to estimate standard deviations of the characterisation methods.

5.3.1 Co-precipitation

A zincian malachite precursor with a Cu:Zn ratio of 70:30 and 3 mol% (metal base) Al was synthesised by co-precipitation from a Cu,Zn,Al nitrate solution (Σ 1 M metal-based), which was acidified by addition of 15 mL concentrated HNO_3, and a 1.6 M Na_2CO_3 solution as a basic precipitating agent in an automated lab reactor. While stirring at 300 rpm, the metal nitrate solution (1800 g) was dosed at 60 g min^{-1} into deionised water (1200 mL) at a controlled temperature of 338 K (Figure Figure 5.1). The pH was controlled by a feedback loop through simultaneous addition of the Na_2CO_3 solution at pH 6.5. Dosing of the acidic metal solution started at $t = 0$ min, and the pH of the solution immediately dropped. To achieve pH 6.5, addition of the base also began at $t = 0$. This addition of base led to the immediate formation of a blue precipitate. The temperature inside the reactor dropped by approximately 5 K because the added solutions had room temperature, but was controlled within ± 2 K after approximately 10 min. After the first pH drop, the fluctuations of the pH were ± 0.5 with decreasing amplitude during addition. After 30 min the dosing was complete. In total, masses of 1800 g metal solution and approximately 1400 g Na_2CO_3 solution were added to the reactor volume. The pH was stabilised. At approximately 20 min after the end of dosing, the colour of the slurry changed from blue to greenish, accompanied by the typical pH drop, indicating the crystallisation of the zincian malachite phase.[18,26] After an ageing time of additional 60 min after the pH drop, the slurry was filtrated and the precipitate was washed 5 times with deionised water until the conductivity

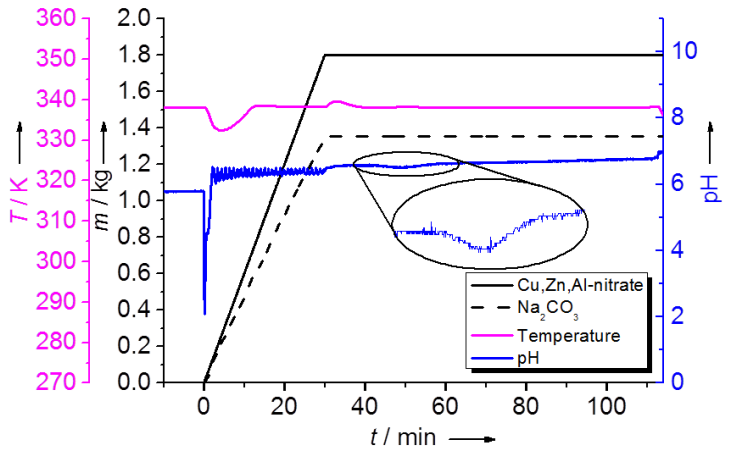

Figure 5.1: Synthesis protocol of FHI-prec preparation. Temperature (pink line), pH (blue line), masses of dosed solutions of metal nitrate (black solid line) and base (dotted line) profiles are plotted. The inset gives an enlargement of the pH negative peak ("drop") at 20 min after end of dosing.

of the filtrate was below 0.5 mS cm^{-1} and no residual Na could be detected by chemical analysis (see section 5.8, Table S.5.1). Spray drying with a Niro minor mobile (T_{inlet}=448 K, T_{outlet}=343 K, pumping speed 30 mL min^{-1}) resulted in a yield of approximately 135 g of a greenish-blue-coloured powder. To demonstrate the reproducibility of the synthesis, three consecutive batches were prepared (see section 5.8).

5.3.2 Precursor

The finely powdered FHI-prec was identified as pure zincian malachite (ZM, see Figure 5.2) phase as expected for this Cu/Zn composition, but exhibited only low crystallinity in the powder XRD pattern. Rietveld refinement yielded a domain size smaller than 10 nm and a low d$(2\,0\,\bar{1})$ of 2.759 Å(Table 5.1).

For comparison, the pure copper malachite has a d$(2\,0\,\bar{1})$ of 2.863 Å. For binary, phase-pure ZM samples with low Zn content, the d$(2\,0\,\bar{1})$ scales linearly with the amount of Zn incorporated into the ZM lattice.[21] This relationship was used to estimate the cationic composition of FHI-prec by extrapolation to a Cu content of $70.6 \pm 0.5\%$. In addition, no indication of a zinc-rich by-phase was found by XRD or scanning electron microscopy energy-dispersive X-ray spectroscopy, demonstrating the successful incorporation of the complete amount of zinc into the malachite lattice.[27] The metal composition determined

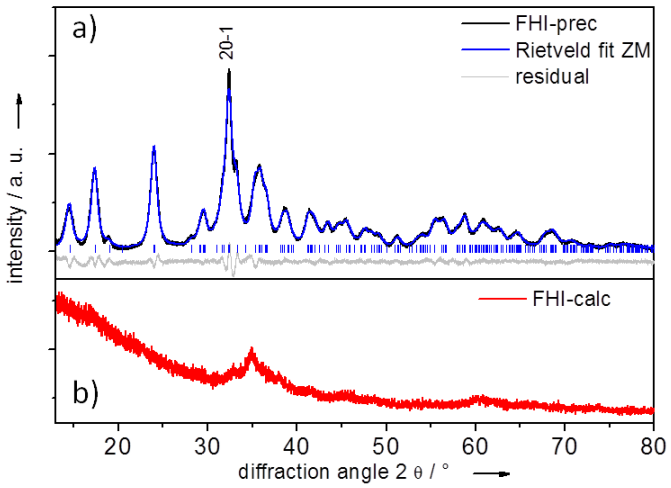

Figure 5.2: Powder XRD pattern of a) FHI-prec (black line) with Rietveld-fit (dark blue line) and b) FHI-calc.

Table 5.1: FHI-prec characterisation by XRD, BET analysis and XRF[a]

	FHI-prec
d($20\bar{1}$) [Å][b]	2.759 ± 0.002
domain size[b] [nm]	9.2 ± 0.6
BET-surface area [m^2g^{-1}]	122± 8
XRF metal-based atom % Cu:Zn:Al	70.3 ± 0.3 : 28.2 ± 0.3 : 1.53 ± 0.05

[a]Standard deviations were determined from measurements of the three individual batches.
[b]As determined by Rietveld refinement.

by X-ray fluorescence (XRF) of FHI-prec corroborates the Cu content as determined by the XRD calibration curve and is close to the nominal value, only the Al content is slightly lower than expected (see Table 5.1). This demonstrates the successful precipitation of the metal ions.

SEM images of FHI-prec are shown in Figure 5.3 a and b. The precursor self-assembles into nanorods (Figure 5.3b). Upon drying, these nanorods form porous non-woven spheres (Figure Figure 5.3a), which is typical for spray-dried materials. The rod-like morphology is a result of the Al^{3+} incorporation into the crystal structure.[22] This preparation method leads to a porous material with a high specific surface area of $122\,m^2\,g^{-1}$ (Table 5.1) as determined by the BET method[28] from N_2-physisorption. According to the Barrett–Joyner–Halenda (BJH) method,[29] the average pore size was determined to be 25.8 nm and likely corresponds to inter-rod pores (see Figure S.5.3 in section 5.8).

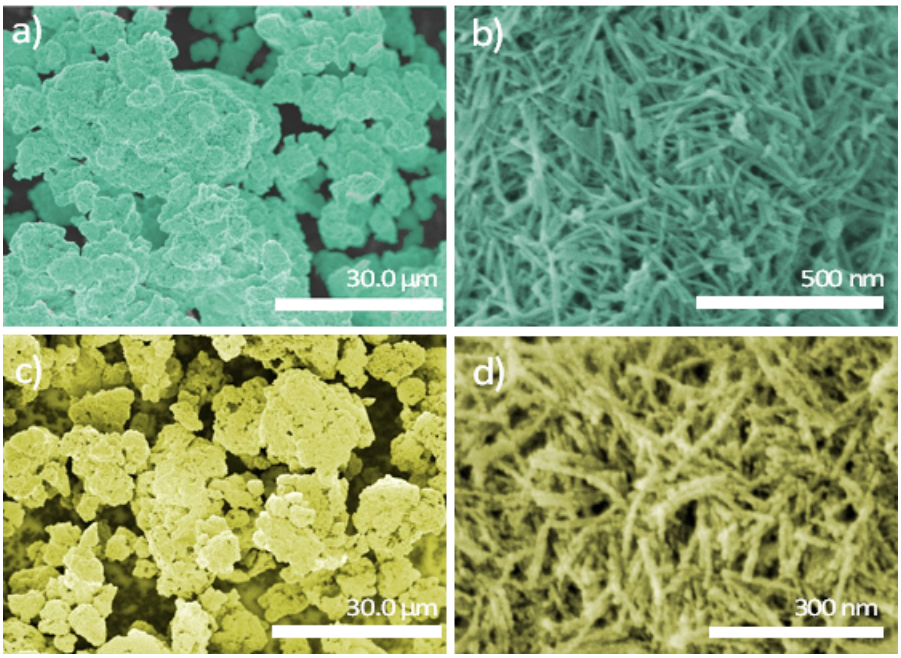

Figure 5.3: SEM images of a,b) FHI-prec and c,d) FHI-calc at different magnifications (for uncoloured images, see the Supporting Information

The thermogravimetry (TG) analysis of FHI-prec in 21 % O_2/Ar-atmosphere (Figure 5.4) reveals the typical two-main-step decomposition of ZM often described in the literature for binary Cu–Zn hydroxy carbonates with Cu contents ranging from 20 % to 80 %.[26,30] After the desorption of physisorbed water and carbon dioxide, in the first main step at

approximately 550 K, H_2O and CO_2 desorb simultaneously, formally corresponding to the formation of an intermediate phase:

$$2(Cu, Zn)_2(OH)_2CO_3 \longrightarrow (Cu, Zn)_4O_3CO_3 + 2\,H_2O + CO_2 \tag{5.1}$$

In the second step, after 750 K, only CO_2 is evolving (see Figure 5.4), corresponding to the formation of the metal oxide

$$(Cu, Zn)_4O_3CO_3 \longrightarrow 4\,(\,Cu, Zn)O + CO_2 \tag{5.2}$$

The intermediate phase is called high-temperature carbonate (HT-CO_3) or sometimes also anion-modified mixed metal oxide.[30,31] This intermediate stage is thought to still conserve the atomically intermixed nature of the precursor to a large extent, whereas upon Reaction 5.2 macroscopic segregation and crystallization can occur. The elaborative thermokinetic analysis of the decomposition TG profiles revealed no significant difference in the kinetic parameters between the current sample and the binary ZM (Cu/Zn 80/20).[32] However, the addition of Al results in a stronger separation of the mentioned thermal events, shifting the decomposition of the ZM phase to lower temperatures and stabilising the intermediate HT-CO_3. We have recently demonstrated that the absolute amount of HT-CO_3 species depends strongly on the mass-transfer conditions in the calcination vessel.[32] Previous results by Fujita et al.[33,34] demonstrated that a slow heating rate, sufficient gas flow and a final temperature between 603 and 623 K prevent the formation of CuO and ZnO macrophase segregated agglomerates. In addition, the resulting calcined material has higher porosity and a high CuO dispersion. Therefore, we chose a calcination temperature of 603 K in this study.

5.3.3 Calcined material

Samples of 10 g of FHI-prec were calcined in a rotary furnace with a flow of 125 mL min^{-1} of 20 % O_2 in Ar at 603 K for 3 h and a heating ramp of 2 K min^{-1}. The calcination parameters have proven to ensure optimum mass-transfer conditions and assure fast removal of the evolved gas products. SEM confirmed that the nanorod morphology of the precursor phase is maintained (see Figure 5.3d). A roughening of the formerly smooth surface happened during calcination. This roughening probably derives from some nanoscale segregation of the non-mixing Cu and Zn oxides. TEM images also reveal the rod-like structure of the

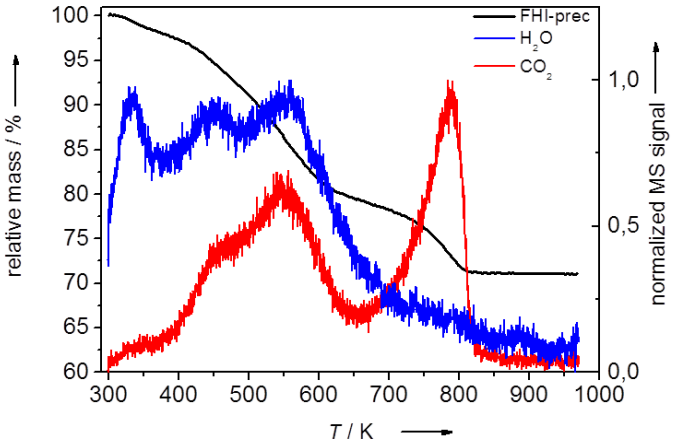

Figure 5.4: TGMS data of FHI-prec with mass curve (black line), evolution of H_2O (m/z 18, blue line) and CO_2 (m/z 44, red line) trace; heating rate is 2 K min^{-1} in O_2/Ar gas flow.

oxide aggregates (Figure 5.5). The calcined material maintains the high BET surface area of approximately 120 m^2 g^{-1} that was already observed in the FHI-prec. The crystallinity of the calcined sample is very low (see Figure 5.2b). No macro-crystalline copper oxide can be identified, only a fine-structured, broad peak at $2\theta = 35°$. TG experiments of the already calcined material reveal the decomposition of a substantial amount of HT-CO_3 evolving at elevated temperatures above 770 K (Table 5.2). The presence of this carbonate species in the calcined material signifies the fact that no strong segregation of CuO took place, which is known to be of beneficial influence for the catalytic activity of the resulting catalyst.[35]

Table 5.2: Characterisation of FHI-calc

	FHI-calc
BET surface area [m^2 g^{-1}]	117.8
average BJH pore size [nm]	26.6
amount of HT-CO_3[a]	5 mass%
TPR_{max} [K][b]	484
integrated TPR signal	63.3 mass% CuO (62.6 %)[a]

[a]Mass loss upon decomposition, determined by TG analysis of FHI-calc.
[b]For TPR with heating rate of 6 Kpm^{-1} in 5% H_2 in Ar.
[c]Nominal value, as determined by combination of XRF analysis and mass loss during TG of FHI-calc.

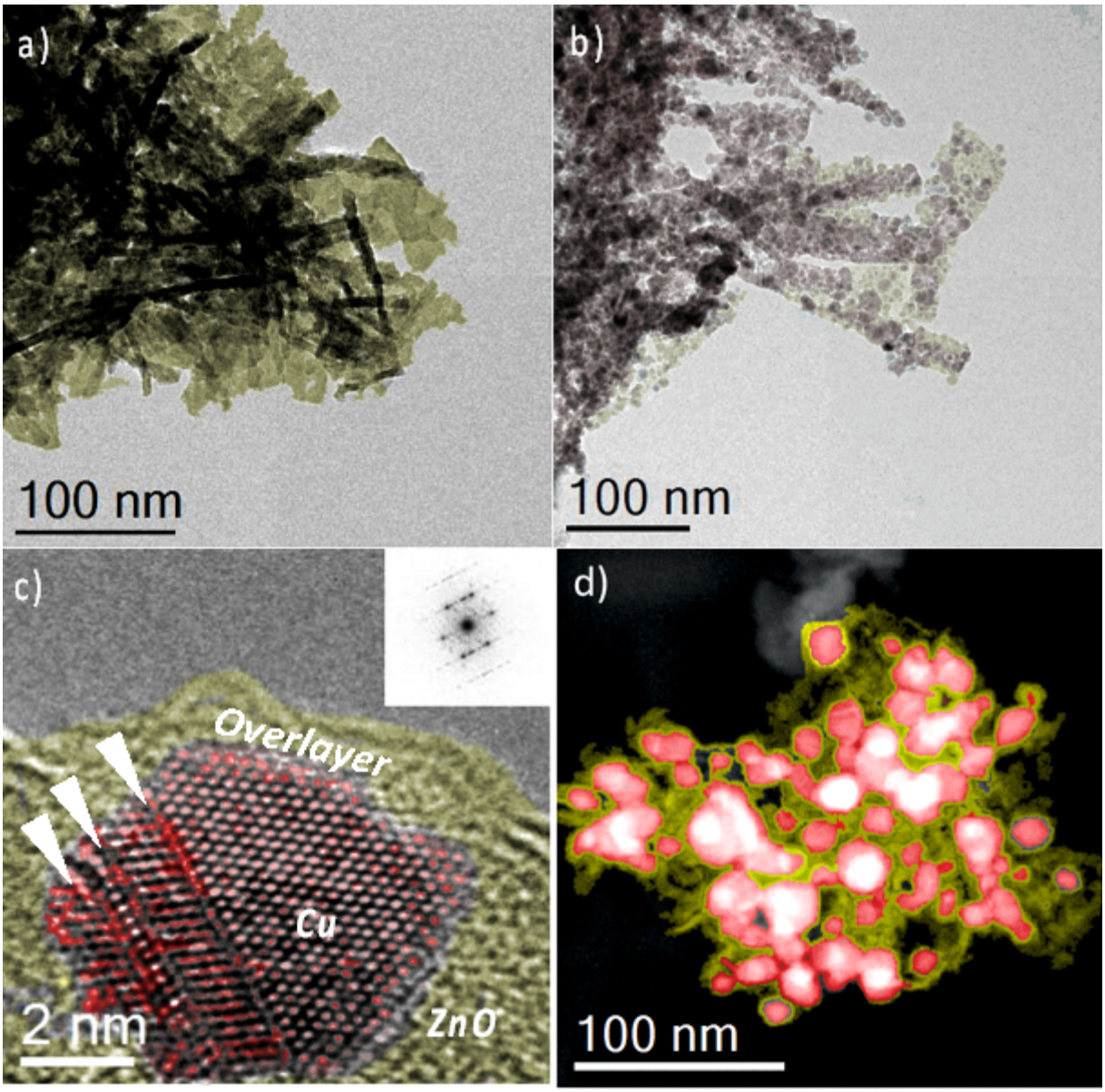

Figure 5.5: TEM micrographs of a) FHI-calc and b-d) FHI-red. c) HRTEM image of a Cu nanoparticle with defects, arrowheads indicate twin formation. d) HAADF-STEM image, red and yellow colours represent Cu and Zn, respectively (for uncoloured versions of the images, see the Supporting Information.

The reducibility of FHI-calc preparation was investigated by temperature-programmed reduction (TPR) in an H_2-containing feed. The TPR profile exhibits a relatively sharp peak with a maximum at a temperature of 484 K if using a heating rate of 6 K min^{-1} (Figure 5.6). This temperature is in line with previously reported reduction temperatures of Cu catalysts starting from CuO nanoparticles and reducing them to Cu metal.[36–38] A small shoulder at the lower temperature side is typical for copper-containing supported systems. On one hand, the shoulder could be ascribed to the reduction of finely dispersed CuO,[37,38] on the other hand the reduction of undecomposed (hydroxy) carbonate species is discussed as the reason for the low-temperature shoulder.[37] Upon increasing the heating rate of the TPR experiment, the shoulder does not vanish but shifts towards higher temperatures along with the peak position. This indicates that the reduction process includes at least two linked subsequent steps (in the studied heating rate range). The second step follows the first one but not vice versa.[39] Mass spectrometry (MS) data recorded during TPR cycles reveal that the beginning of the reduction is accompanied by CO_2 evolution. The second and third TPR performed after subsequent oxidation (TPO) cycles do not lead to more CO_2 evolution and yield a reduction peak that is shifted to lower temperature than that of the first reduction of the carbonate-containing fresh catalyst (see Figure S.5.8 a). These results indicate that the residual carbonate content retards the reduction of CuO. However, the reduction of the uncalcined pure hydroxy carbonate precursor FHI-prec only starts at even higher temperatures (see Figure S.5.8 b) demonstrating the different type of the carbonate species. Our recent thermokinetic study revealed that the reduction of Al-richer Cu/Zn precursors is most reliably described by two autocatalytic consecutive steps. The reduction runs through the formation of the kinetically stabilized, amorphous Cu(I) oxide (1st step) and leads to the subsequent formation of nanocrystalline Cu0 in the 2nd step.[40,41] Also in this case, the reduction of CuO is limited by the carbonate decomposition. The stability of the intermediate Cu_2O species depends on the precursor's microstructure, which in turn can be influenced by the calcination temperature.[40] The experimental TPR profiles in Figure 5.6 are adequately described by applying a two consecutive autocatalytic reaction model[39] with the activation energies of approximately 45 kJ mol^{-1} for the Cu_2O formation and approximately 30 kJ mol^{-1} for the subsequent reduction of Cu_2O to Cu. Detailed information about the thermokinetic analysis can be found in section 5.8. In comparison with the Al-richer hydrotalcite-derived Cu/ZnO system,[41] FHI-calc has a considerably lower activation barrier and faster course of reaction. Higher values of activation energies

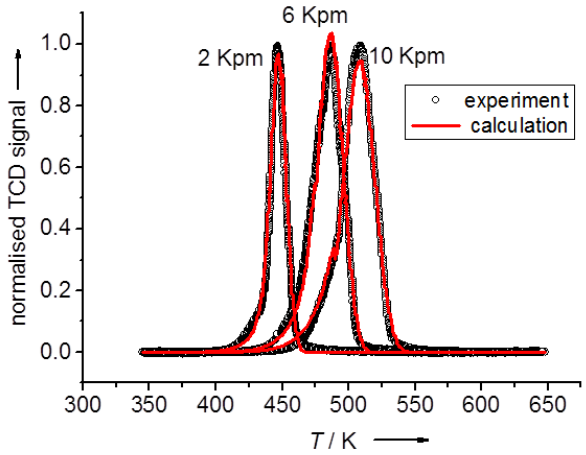

Figure 5.6: TPR profiles of FHI-calc in 80 mL min^{-1}, 5% H_2/Ar with heating rates of 2, 6 and 10 K min^{-1} and the fitting results of non-linear regression.

of approximately 60–80 kJ mol^{-1} have been reported previously for pure CuO as well as for supported systems.[36,42,43]

5.3.4 The reduced catalyst

To obtain the catalytically active state, the calcined material was reduced at 523 K in hydrogen. For catalytic testing and N_2O chemisorption, reduction is usually performed directly in the reactor, but to further characterise the active state, we reduced the calcined sample in a separate step and transferred it under inert-gas conditions in a glove box. The N_2O chemisorption capacity is usually used as an indicator for the catalytic activity, assuming that it is proportional to the copper surface area.[44] Recently it has been shown that also defective ZnO in close contact with copper contributes to a significant N_2O consumption[45,46] likely by the oxidation of oxygen vacancies in ZnO_x. Still it remains valid, that the N_2O chemisorption capacity is a coarse indicator for methanol synthesis activity in CO_2-containing feed gas, because N_2O seems to probe the important Cu-ZnO synergy as well as the Cu surface area. FHI-red exhibits an exceptionally high N_2O chemisorption capacity of 459 μmol g_{calc}^{-1}. If used for the calculation of the Cu surface area, a high value of 38 m^2 g_{calc}^{-1} is obtained. However, upon comparing the N_2O capacity to the H_2 chemisorption capacity, it was recently found for a different batch of FHI-red (labelled CZA3 therein) that the true Cu surface area amounts to only approximately 16 m^2 g^{-1}, and the residual N_2O is rather decomposed on defect sites of ZnO_x.[45] The FHI-red catalyst

exhibits an exceptional high amount of these defect sites likely as a result the efficient doping of ZnO with Al^{3+} residing on Zn^{2+} sites.[23]

Table 5.3: Characterisation of FHI-red

	FHI-red
N_2O chemisorption capacity[a] [μmol g_{cat}^{-1}]	459
Cu surface area$_{N_2O}$ [m^2 g_{cat}^{-1}][a]	37.6
Cu surface area$_{H_2}$ [m^2 g_{cat}^{-1}][b]	15.6
Cu domain size [nm][c]	4.47(7)
ZnO domain size [nm][c]	3.06(4)
d(200) shoulder [Å][d]	1.822
stacking fault probability α	0.023
TEM mean particle size [nm]	8.09 ± 2.62

[a]Determined by N_2O-reactive frontal chromatography (RFC).
[b]Determined from H_2-chemisorption, literature value taken from Ref.[45].
[c]Determined from Rietveld fit of neutron diffration pattern.
[d]Determined from pattern decomposition of neutron diffration pattern.

Surface composition

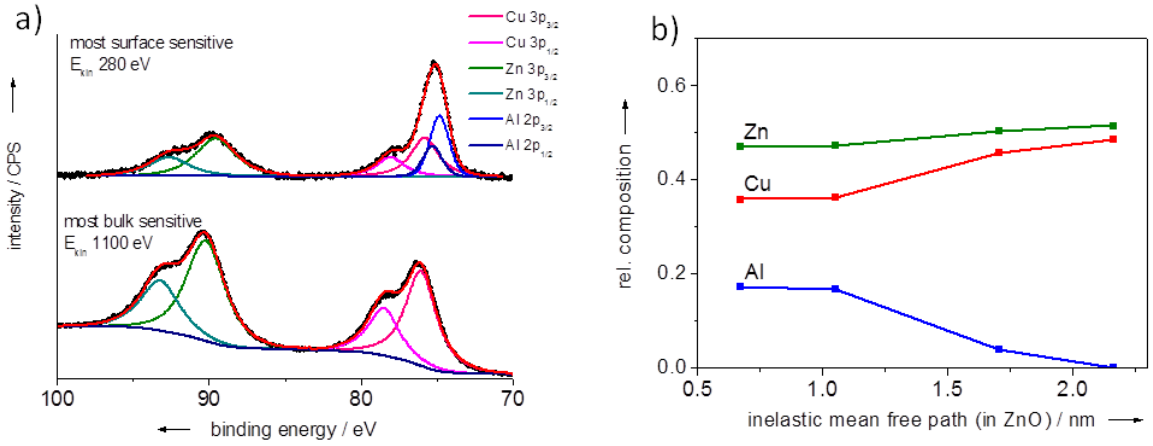

Figure 5.7: a) Cu 3p, Zn 3p, Al 2p XPS region with different excitation energy of incident X-ray beam; b) metal surface composition with different depth as determined by XPS.

We performed near-ambient-pressure X-ray photoelectron spectroscopy (NAP–XPS) measurements of FHI-red (Figure 5.7) to determine the depth profile of the surface composition under reducing conditions similar to those of the feed gas. A gas mixture of H_2 and CO_2

was introduced into the XPS chamber and the sample was heated to 523 K. The amount of zinc at the surface is strongly increased and that of copper depleted relative to the element amounts in the bulk material. Furthermore, aluminium is strongly enriched at the surface whereas for the most bulk-sensitive measurement no more aluminium was distinguishable (see Figure 5.7). It was observed before that under reducing conditions, zinc oxide species creep over the copper surface.[47–49] This phenomenon is also referred to as strong metal–support interaction.[50] An aluminium enrichment at the surface was also observed for a doped ZnO:Al (3 %) sample without copper upon heating in H_2 atmosphere,[25] which is an indication that the Al promoter is situated in the surface-decorating ZnO_x phase also for the copper containing catalyst. Near-edge X-ray absorption fine-structure spectra of Cu L and Zn L edge were recorded under the same *in situ* conditions as for the XPS spectra. The Cu L spectrum showed no indication of oxidised Cu species in the active state and agrees well with that of the metallic Cu reference (see Figure S.5.7). The Zn L edge exhibits similar features to that of the ZnO wurtzite reference sample.

Microstructure

TEM reveals insights into the micro- and nanostructure of the reduced material. Therefore, a series of TEM images using different TEM techniques were recorded to visualise structural features of FHI-calc and FHI-red. The images are shown in Figure 5.5. FHI-calc (Figure 5.5a) and FHI-red (Figure 5.5b) bear a rod-like microstructure indicating that after reduction the morphology is conserved. Furthermore, the appearance of nanoparticles on the outside of the nanorods renders the impression of a salty pretzel stick like morphology. A high-resolution (HR)TEM micrograph of this particle is given in Figure 5.5c. It shows a defective Cu particle viewed along [1 0 1] on the ZnO support. The Cu particle is traversed by twins (Figure 5.5c) and is enriched with high-energy surface steps. These steps were previously identified to be important for high-performance catalysts.[47,51] Equally in agreement with previous observations[47] is the overlayer on the Cu particles that can be attributed with the creeping of ZnO_x during reduction onto the metal because of the strong metal–support interaction. In addition, high-angle annular dark-field scanning TEM (HAADF–STEM) micrographs were collected (Figure 5.5d), which provide detailed insight in the microstructure of Cu/ZnO based catalysts. Apparently, the Cu nanoparticles are homogeneously distributed over the porous ZnO matrix. A more detailed investigation of the ZnO component can be found elsewhere.[52] This beneficial morphology allows the formation of a porous network maintaining the high BET surface area of the precursor.

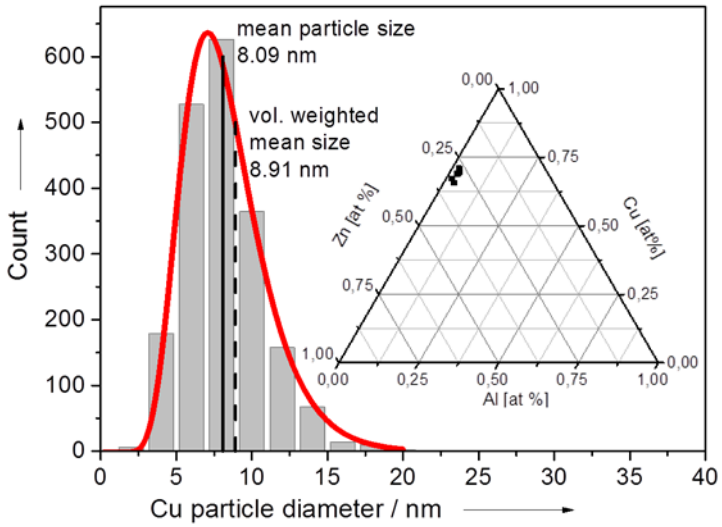

Figure 5.8: Particle-size distribution as determined by TEM and the catalyst composition obtained by EDX measurements (inset).

The particle sizes of approximately 2000 particles were evaluated from TEM micrographs recorded at moderate resolution, and particle-size distribution with the mean particle size of 8.09 nm and a standard deviation of 2.62 nm were found (Figure 5.8). Energy-dispersive X-ray (EDX) spectroscopy of different Cu/ZnO:Al aggregates revealed that the a homogeneous distribution of the elements throughout the precursor was conserved during the thermal treatments (Figure 5.8 inset).

Defect analysis of copper

In Figure 5.9, the neutron diffraction pattern of a different batch of FHI-red is plotted. Clearly visible are contributions from Cu metal and ZnO. Because of the defective structure of the Cu nanoparticles, the pattern cannot be fitted satisfactorily with a conventional Rietveld fit [53] (Figure 5.9a). The systematic deviations between experimental and theoretical intensity can be related to the effect of stacking faults on characteristic peak profiles, for example, a particular broadening and thus over-estimation of the 2 0 0 and 4 0 0 peaks. One phenomenological possibility to minimise these deviations is to introduce an additional peak to compensate for the shifted and broadened contribution of the d(2 0 0) reflex (Figure 5.9b). With this fit, a pseudo-Cu-domain size of approximately 4.5 nm is obtained (Table 5.3). This size is significantly smaller than the particle size determined by TEM, which might be caused by stacking faults and twin boundaries [51,54] (see also Figure 5.5c)

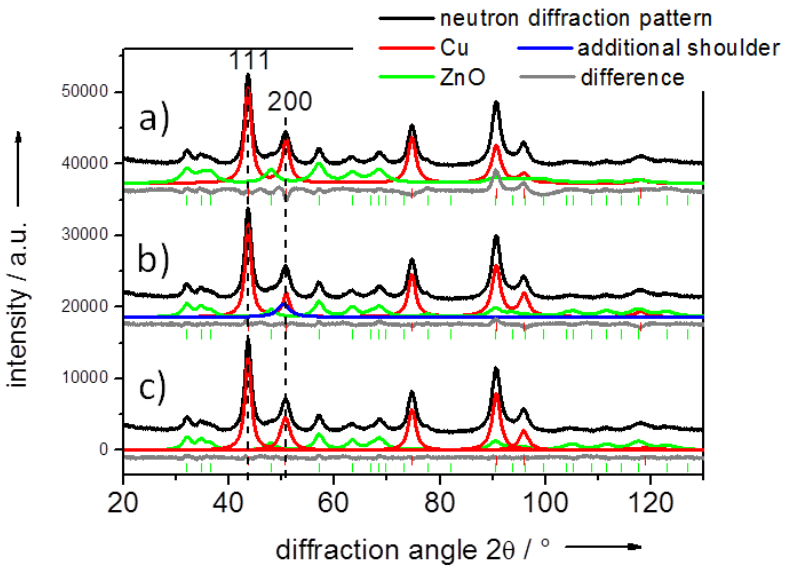

Figure 5.9: Neutron diffraction pattern of FHI-red with a) unmodified Rietveld fit, b) modified Rietveld fit and c) pattern decomposition of Cu phase.

making the particles polycrystalline. Another possibility to obtain more information about the stacking faults, which is hidden in the peak profiles of the diffraction pattern, is the calculation of the stacking fault probability α. This can be calculated from the positions of the 1 1 1 and 2 0 0 reflections using equations derived by Warren:[54]

$$\alpha = 8.3 \left(\frac{2}{\sqrt{3}} - \frac{sin\theta(200)}{sin\theta(111)} \right) \tag{5.3}$$

The positions can be obtained by pattern decomposition of the copper phase, without using a structural model (Figure 5.9c, the Rietveld results for the ZnO phase were untouched). The distance between these two peaks is different from that for a "perfect" fcc lattice, as a result of stacking faults. The more stacking faults are present, the closer the 1 1 1 and 2 0 0 reflection shift together. Using this method, we determined a stacking-fault probability α of 0.023 for our catalyst, which is in the order of the stacking-fault probability of other high-performance catalysts determined by the same method.[47] This value means that 2.3% of the (1 1 1) planes are faulted corresponding to an average of approximately one fault per particle based on the average particle diameter and the 1 1 1 spacing of Cu.

5.3.5 Activity

The final catalyst was tested in methanol synthesis from a CO_2-rich syngas mixture as well as in CO_2 hydrogenation and in the reverse water gas shift (rWGS) reaction. The catalyst was previously reported to exhibit high performance in methanol synthesis from syngas,[23] which was approximately 30 % higher than the performance of a similarly synthesized catalyst with the industrial-like Al-richer composition. During the first two hours on stream, a significant deactivation of approximately 10 % was observed, which levelled off to show a steady-state activity. After 6 h at 503 K a rate of 387 μmol g_{cat}^{-1} min^{-1} was observed in syngas conditions as described in the Experimental Section 5.5 (at 3.4 % conversion). At near-differential conditions in CO_2 hydrogenation, the activity is even higher with 624 μmol g_{cat}^{-1} min^{-1} at a conversion of 3.1 %.

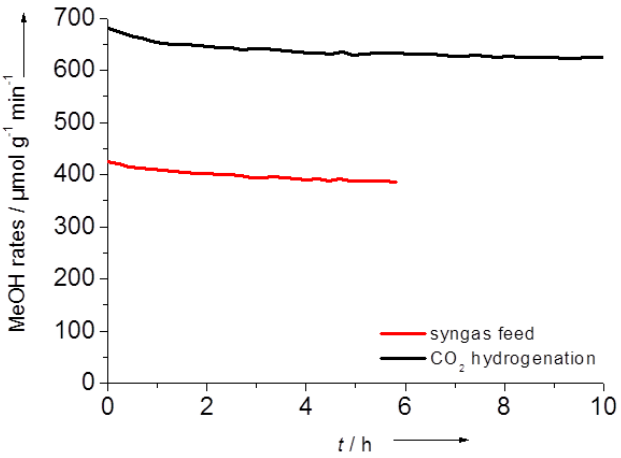

Figure 5.10: Activity measurements in methanol synthesis with different feed gases: CO_2/H_2 3:1 (black line) and $CO_2/CO/H_2$ 8:6:59 (red line).

Apparent activation energies are the same for both feed gases, approximately 57 kJ mol^{-1} (see Figure S.5.10 for Arrhenius plots). The rate of methanol synthesis is very sensitive to the conversion, probably as a result of product inhibition by water (see also section 5.8), a fact that should be kept in mind if comparing rates of different catalysts. For CO_2 hydrogenation in the absence of extra CO that might scavenge water, this effect is described, e.g., in Ref.[55] and[56]. No dimethyl ether was detected as a by-product during the methanol synthesis experiments. The activity in the rWGS reaction at ambient pressure, 503 K and in a CO_2/H_2 mixture with a low CO_2/H_2 ratio after 6 h time on stream (TOS) is approximately 400 μmol g_{cat}^{-1} min^{-1} (Figure 5.10). The yield is approximately 1.1 % and

the selectivity towards CO at this conditions is 97 %. The only by-product observed is methanol, but the conversion is limited by the unfavourable equilibrium at ambient pressure. With higher reaction temperature, the selectivity towards CO therefore increases. The activation energy for CO formation is determined to be 111 kJ mol^{-1}. Compared to the H_2 rich gas mixture and high pressure, for which the rate is 260 μmol g_{cat}^{-1} min^{-1} after 6 h TOS and the activation energy is 126 kJ mol^{-1}, the rWGS reaction is favoured under this hydrogen-depleted conditions.

5.4 Conclusions

A highly active Cu/ZnO:Al-based catalyst for methanol synthesis is presented, which was prepared by an optimised variant of the well-established co-precipitation method at constant pH. In-depth characterisation at various stages of catalyst preparation gives a comprehensive picture of the preparation process and the evolution of the catalyst's microstructure. In the end, a uniform nano- and mesostructured composite material with small copper particle size, very high N_2O chemisorption capacity and high defect density enables high activity in methanol synthesis from CO_2-containing feed gases. The reproducibility, the known preparation history and the beneficial properties of this material renders it a promising benchmark system for studies of Cu/ZnO-based catalysts also in other reactions.

5.5 Experimental section

5.5.1 Raw materials

For the co-precipitation, the following raw materials were used: zinc nitrate hexahydrate (Sigma–Aldrich), copper(II) nitrate trihydrate ($\leq$ 99 % p.a., ACS, Carl Roth GmbH), aluminium nitrate nonahydrate ($\leq$ 98 % p.a., Carl Roth GmbH), nitric acid (ROTIPURAN® $\leq$ 65 % p.a., ISO, Carl Roth GmbH) and sodium carbonate ($\leq$ 99 %, water free, Carl Roth GmbH). Deionised water was used from a Millipore system.
The co-precipitation was performed in an automated laboratory reactor system called Labmax (from Mettler Toledo). It consisted of a double-walled glass reactor with an oil bath for temperature control. Two membrane pumps were used for pumping the solutions into the reactor. Temperature and dosing were controlled from a PC station. Several parameters such as temperature, stirring speed, pH and conductivity were monitored simultaneously.

The dosing speed of the metal solution was kept constant at 60 g min^{-1}, the dosing of the base was controlled such that a constant pH of 6.5 was reached.

5.5.2 Characterisation

Powder XRD patterns were recorded on a STOE Stadi-P diffractometer equipped with a primary focusing Ge monochromator (CuKα_1 radiation) and a linear-position-sensitive detector. The samples were mounted in the form of a clamped sandwich of small amounts of powder fixed with a small amount of grease between two layers of thin polyacetate film. The precursor pattern for Rietveld refinement was recorded on a STOE theta/theta diffractometer in Bragg–Brentano geometry by using a DECTRIS MYTHEN1K position-sensitive detector (Ni-filtered CuKα radiation). Pattern fitting and phase analysis were performed by using the Rietveld method as implemented in the TOPAS software package.[57] XRF spectroscopy was performed of the precursor powder in a Bruker S4 Pioneer X-ray spectrometer.
Thermogravimetric analysis (TG/DSC) was performed on a Netzsch STA449 Jupiter thermoanalyser (2 and 10 K min^{-1}, 21 % O_2 in Ar). Evolution of the gas phase during reaction was monitored with a quadrupole mass spectrometer (Pfeiffer, QMS200 Omnistar).
TPR of the calcined sample was performed in a fixed-bed reactor (TPDRO-1100, CE instruments), in 5 vol % H_2 in Argon at a heating rate of 6 K min^{-1} (80 mL min^{-1}, end temperature 573 K, holding time 30 min). The H_2 consumption was monitored with a thermal conductivity detector. Additionally, for a kinetic TPR study TPR profiles with different heating rates were recorded: 2 K min^{-1}, 6 K min^{-1}, 10 K min^{-1}. The TPR profiles were evaluated by applying the Netzsch Thermokinetics 3 software to the TPR data of the present system. This software was described by Opfermann[58] and is typically used for the analysis of thermoanalysis data of gas–solid reactions.[59,60]
SEM images were taken in a Hitachi S-4800 field-emission gun system. HRTEM images were taken on a FEI Titan 80-300 equipped with a Cs corrector at 300 kV. For the determination of the particle-size distribution, images were recorded by using a Philips CM200FEG microscope at 200 kV with a magnification of 72,000. Prior to TEM investigation, the sample was reduced at 523 K and transferred to the microscope with a vacuum transfer holder under inert atmosphere.
The reduced catalyst was characterised by near-ambient-pressure X-ray photoelectron and near-edge X-ray absorption fine-structure spectroscopy at the ISISS beam line of the synchrotron facility BESSY-II of the Helmholtz-Zentrum Berlin. A depth profiling experiment

was performed in CO_2/H_2 at 523 K (250 °C), 0.5 mbar, to estimate the distribution of the metals as a function of information depth under conditions similar to catalyst working conditions. Cu 3p, Zn 3p and Al 2p core levels were recorded at various photon energies yielding electron kinetic energies of 180, 400, 800 and 1100 eV.
For neutron diffraction, approximate sample amounts of 4 g were reduced in 20 % H_2 in Ar up to a final temperature of 515 K. The reduced sample was transferred inside a glove box into a 6 mm vanadium cuvette and sealed with indium without contact to air. The measurements were conducted at FRM-II at the beam line SPODI.[61] The neutron wavelength was 1.549 Å. The neutron diffraction pattern was refined by using the Topas software package. Pattern decomposition of the copper phase was performed by fitting each reflex with a pseudo-Voigt function, without a structural model.
Specific surface areas were determined by N_2 physisorption in a Quantachrome Autosorb-1 machine. Prior to analysis, the samples were degassed for 2 h at 353 K. N_2O chemisorption capacity was determined by using reactive frontal chromatography.[44] An approximate amount of 100 mg of calcined sample (sieve fraction) was placed in a fixed bed reactor. After *in situ* reduction, the sample was cooled down in the reducing gas to RT, purged with He and switched to 10 mL min^{-1} of a 1% N_2O in He mixture. The N_2O chemisorption capacity and Cu surface area were calculated from the mass spectrometry signal of the N_2 trace (m/z=28).
Methanol synthesis from syngas and CO_2 hydrogenation were tested in a fixed-bed flow reactor. Samples of 50 mg (100–200 μm particle diameter, diluted with 0.7 g of SiO_2) were loaded into a 6 mm inner diameter stainless-steel reactor tube using a bed volume of 4.5 mL. The catalyst was reduced at 523 K (1 K min^{-1}) for 1.5 h in 20% H_2 in Ar. Upon completion of the reduction, the reactor was cooled to 503 K, a 3:1 H_2/CO_2 mixture (100 mL min^{-1}) containing 4% Ar (as an internal standard) was introduced into the reactor, and the pressure was raised to 30 bar. Online analysis of products was performed with a gas chromatograph (Agilent 7890A). Performance under syngas conditions was tested at the same T and p in the same setup. The feed gas contained 6% CO, 8% CO_2, 59% H_2 and balance Ar. The rWGS reaction was tested in the same setup at ambient pressure. Flows of 47 mL min^{-1} CO_2, 34 mL min^{-1} H_2 and 20 mL min^{-1} argon were used.

5.6 Acknowledgements

The authors thank Stefan Zander (help with catalytic measurements), Frank Girgsdies (XRD), Jasmin Allan (XRD, TG), Gisela Weinberg (SEM), Norbert Pfänder and Igor Kasatkin (TEM), Michael Hävecker (NAP-XPS) Maike Hashagen (BET), Achim Klein (XRF), Timur Kandemir and Markus Hölzel and Anatoliy Senyshyn (neutron diffraction) and Stefanie Kühl (help with synthesis). FRM-II is acknowledged for the allocation of neutron scattering beam time and BESSY-II for synchrotron beam time. We thank Martin Muhler, Olaf Hinrichsen and Clariant Produkte (Deutschland) GmbH, BU Catalysts, for long-standing collaboration and fruitful discussions.

5.7 References

[1] J. Schumann, T. Lunkenbein, A. Tarasov, N. Thomas, R. Schlögl, M. Behrens, *ChemCatChem* **2014**, *6*, 2889.

[2] G. A. Olah, A. Goeppert, G. K. Surya Prakash, *Beyond Oil and Gas: The Methanol Economy*, Wiley-VCH, Weinheim, **2006**.

[3] L. C. Grabow, M. Mavrikakis, *ACS Catal.* **2011**, *1*, 365.

[4] Y. Yang, C. Mims, D. Mei, C. Peden, C. Campbell, *J. Catal.* **2013**, *298*, 10.

[5] F. Studt, F. Abild-Pedersen, J. B. Varley, J. K. Norskov, *Catal. Lett.* **2013**, *143*, 71.

[6] V. Schott, H. Oberhofer, A. Birkner, M. Xu, Y. Wang, M. Muhler, K. Reuter, C. Wöll, *Angew. Chem. Int. Ed.* **2013**, *52*, 11925.

[7] W. Tong, A. West, K. Cheung, K.-M. Yu, S. C. E. Tsang, *ACS Catal.* **2013**, *3*, 1231.

[8] S. Zander, E. L. Kunkes, M. E. Schuster, J. Schumann, G. Weinberg, D. Teschner, N. Jacobsen, R. Schlögl, M. Behrens, *Angew. Chem. Int. Ed.* **2013**, *52*, 6536.

[9] Z. Liu, A. Rittermeier, M. Becker, K. Kähler, E. Löffler, M. Muhler, *Langmuir* **2011**, *27*, 4728.

[10] G. Prieto, K. P. de Jong, P. E. de Jongh, *Catal. Today* **2013**, *215*, 142.

[11] G. Simson, E. Prasetyo, S. Reiner, O. Hinrichsen, *Appl. Catal., A* **2013**, *450*, 1.

[12] S. Kaluza, M. Behrens, N. Schiefenhövel, B. Kniep, R. Fischer, R. Schlögl, M. Muhler, *ChemCatChem* **2011**, *3*, 189.

[13] S. Kühl, M. Friedrich, M. Armbrüster, M. Behrens, *J. Mater. Chem.* **2012**, *22*, 9632.

[14] F. Liao, Z. Zeng, C. Eley, Q. Lu, X. Hong, S. C. E. Tsang, *Angew. Chem. Int. Ed.* **2012**, *51*, 5832.

[15] K. Föttinger, J. A. van Bokhoven, M. Nachtegaal, G. Rupprechter, *J. Phys. Chem. Lett.* **2011**, *2*, 428.

[16] L. Li, B. Zhang, E. Kunkes, K. Föttinger, M. Armbrüster, D. S. Su, W. Wei, R. Schlögl, M. Behrens, *ChemCatChem* **2012**, *4*, 1764.

[17] Q. Wu, W. L. Eriksen, L. D. L. Duchstein, J. M. Christensen, C. D. Damsgaard, J. B. Wagner, B. Temel, J.-D. Grunwaldt, A. D. Jensen, *Catal. Sci. Technol.* **2014**, *4*, 378.

[18] C. Baltes, S. Vukojevic, F. Schüth, *J. Catal.* **2008**, *258*, 334.

[19] M. Behrens, R. Schlögl, *Z. anorg. allg. Chem.* **2013**, 2683.

[20] M. Behrens, D. Brennecke, F. Girgsdies, S. Kißner, A. Trunschke, N. Nasrudin, S. Zakaria, N. F. Idris, S. B. A. Hamid, B. Kniep, R. Fischer, W. Busser, M. Muhler, R. Schlögl, *Appl. Catal., A* **2011**, *392*, 93.

[21] S. Zander, B. Seidlhofer, M. Behrens, *Dalton Trans.* **2012**, *41*, 13413.

[22] M. Behrens, *J. Catal.* **2009**, *267*, 24.

[23] M. Behrens, S. Zander, P. Kurr, N. Jacobsen, J. Senker, G. Koch, T. Ressler, R. W. Fischer, R. Schlögl, *J. Am. Chem. Soc.* **2013**, *135*, 6061.

[24] J. B. Hansen, P. E. H. Nielsen, *Handbook of Heterogeneous Catalysis*, chapter Methanol Synthesis, Wiley-VCH, Weinheim, 2nd Edition, **2008**, pp. 2920–2944.

[25] M. Behrens, G. Lolli, N. Muratova, I. Kasatkin, M. Hävecker, R. N. d'Alnoncourt, O. Storcheva, K. Kohler, M. Muhler, R. Schlögl, *Phys. Chem. Chem. Phys.* **2013**, *15*, 1374.

[26] B. Bems, M. Schur, A. Dassenoy, H. Junkes, D. Herein, R. Schlögl, *Chem. Eur. J.* **2003**, *9*, 2039.

[27] M. Behrens, F. Girgsdies, A. Trunschke, R. Schlögl, *Eur. J. Inorg. Chem.* **2009**, *2009*, 1347.

[28] S. Brunauer, P. H. Emmett, E. Teller, *J. Am. Chem. Soc.* **1938**, *60*, 309.

[29] E. P. Barrett, L. G. Joyner, P. P. Halenda, *J. Am. Chem. Soc.* **1951**, *73*, 373.

[30] G. J. Millar, I. H. Holm, P. J. R. Uwins, J. Drennan, *J. Chem. Soc., Faraday Trans.* **1998**, *94*, 593.

[31] T. Yurieva, *React. Kinet. Catal. Lett.* **1995**, *55*, 513.

[32] A. Tarasov, J. Schumann, F. Girgsdies, N. Thomas, M. Behrens, *Thermochim. Acta* **2014**, *591*, 1.

[33] S. Fujita, S. Moribe, Y. Kanamori, N. Takezawa, *React. Kinet. Catal. Lett.* **2000**, *70*, 11.

[34] S. Fujita, S. Moribe, Y. Kanamori, M. Kakudate, N. Takezawa, *Appl. Catal., A* **2001**, *207*, 121.

[35] M. Schur, B. Bems, A. Dassenoy, I. Kasatkin, J. Urban, H. Wilmes, O. Hinrichsen, M. Muhler, R. Schlögl, *Angew. Chem. Int. Ed.* **2003**, *42*, 3815.

[36] J. Sloczynski, R. Grabowski, A. Kozlowska, P. K. Olszewski, J. Stoch, *Phys. Chem. Chem. Phys.* **2003**, *5*, 4631.

[37] J. P. Breen, J. R. Ross, *Catal. Today* **1999**, *51*, 521.

[38] M. Shimokawabe, H. Asakawa, N. Takezawa, *Appl. Catal.* **1990**, *59*, 45.

[39] E. Moukhina, *J. Therm. Anal. Calorim.* **2012**, *109*, 1203.

[40] A. Tarasov, S. Kühl, J. Schumann, M. Behrens, *High Temp.-High Press.* **2013**, *42*, 377 .

[41] S. Kühl, A. Tarasov, S. Zander, I. Kasatkin, M. Behrens, *Chem. Eur. J.* **2014**, *20*, 3782.

[42] A. Boyce, S. Graville, P. Sermon, M. Vong, *React. Kinet. Catal. Lett.* **1991**, *44*, 1.

[43] J. Y. Kim, J. A. Rodriguez, J. C. Hanson, A. I. Frenkel, P. L. Lee, *J. Am. Chem. Soc.* **2003**, *125*, 10684.

[44] G. Chinchen, C. Hay, H. Vandervell, K. Waugh, *J. Catal.* **1987**, *103*, 79.

[45] M. B. Fichtl, J. Schumann, I. Kasatkin, N. Jacobsen, M. Behrens, R. Schlögl, M. Muhler, O. Hinrichsen, *Angew. Chem. Int. Ed.* **2014**, *53*, 7043.

[46] S. Kuld, C. Conradsen, P. G. Moses, I. Chorkendorff, J. Sehested, *Angew. Chem. Int. Ed.* **2014**, *53*, 5941.

[47] M. Behrens, F. Studt, I. Kasatkin, S. Kühl, M. Hävecker, F. Abild-Pedersen, S. Zander, F. Girgsdies, P. Kurr, B. L. Kniep, M. Tovar, R. W. Fischer, J. K. Nørskov, R. Schlögl, *Science* **2012**, *336*, 893.

[48] J.-D. Grunwaldt, A. Molenbroek, N.-Y. Topsøe, H. Topsøe, B. Clausen, *J. Catal.* **2000**, *194*, 452.

[49] Y. Kanai, T. Watanabe, T. Fujitani, M. Saito, J. Nakamura, T. Uchijima, *Catal. Lett.* **1994**, *27*, 67.

[50] R. Naumann d'Alnoncourt, X. Xia, J. Strunk, E. Löffler, O. Hinrichsen, M. Muhler, *Phys. Chem. Chem. Phys.* **2006**, *8*, 1525.

[51] I. Kasatkin, P. Kurr, B. Kniep, A. Trunschke, R. Schlögl, *Angew. Chem.* **2007**, *119*, 7465.

[52] T. Lunkenbein, J. Schumann, M. Behrens, R. Schlögl, M. Willinger, *Angew. Chem. Int. Ed., accepted* .

[53] T. Kandemir, I. Kasatkin, F. Girgsdies, S. Zander, S. Kühl, M. Tovar, R. Schlögl, M. Behrens, *Top. Catal.* **2014**, *57*, 188.

[54] B. E. Warren, *X-ray diffraction*, Dover Publications, New York, **1990**.

[55] E. Kunkes, M. Behrens, *Chemical Energy Storage*, De Gryter, Berlin/Boston, **2013**.

[56] M. Sahibzada, I. S. Metcalfe, D. Chadwick, *J. Catal.* **1998**, *174*, 111.

[57] A. Coelho, *TOPAS: General Profile and Structure Analysis Software for Powder Diffraction Data; Bruker AXS GmbH: Karlsruhe, Germany* **2006**, *version 3.0*.

[58] J. Opfermann, *J. Therm. Anal. Calorim.* **2000**, *60*, 641.

[59] N. A. Tikhonov, I. V. Arkhangelsky, S. S. Belyaev, A. T. Matveev, *Thermochim. Acta* **2009**, *486*, 66.

[60] I. Arkhangelsky, A. Dunaev, I. Makarenko, N. Tikhonov, S. Belyaev, A. Tarasov, *Non-Isothermal Kinetic Methods*, Edition Open Access, Berlin, **2013**.

[61] M. Hoelzel, A. Senyshyn, N. Juenke, H. Boysen, W. Schmal, H. Fuess, *Nucl. Instr. A* **2012**, *667*, 32.

5.8 Supplementary information

Contents:

- Catalyst preparation protocols of reproduced samples
- Characterisation of reproduced samples
- Uncolored versions of microscopy images
- Results of the formal thermokinetic analysis of the reduction process
- Catalytic data: Flow dependence of methanol rate, activation energies of methanol synthesis and rWGS reaction

- FHI internal sample numbers

To use the FHI-standard catalyst in your lab, please send your request to **FHIstd@fhi-lists.de**. The catalyst will be shipped in small aliquots in the calcined form. The reduction protocol can be found in the main article and will be provided with the catalyst. The use is free of charge provided adequate reference is made to this article and the results are shared, e.g. in a publication. Direct feedback of all measurements to the above mentioned e-mail address is highly desired to collect a wide comparative data basis, which is planned to be subject of a forthcoming paper.

Catalyst preparation protocols of reproduced samples

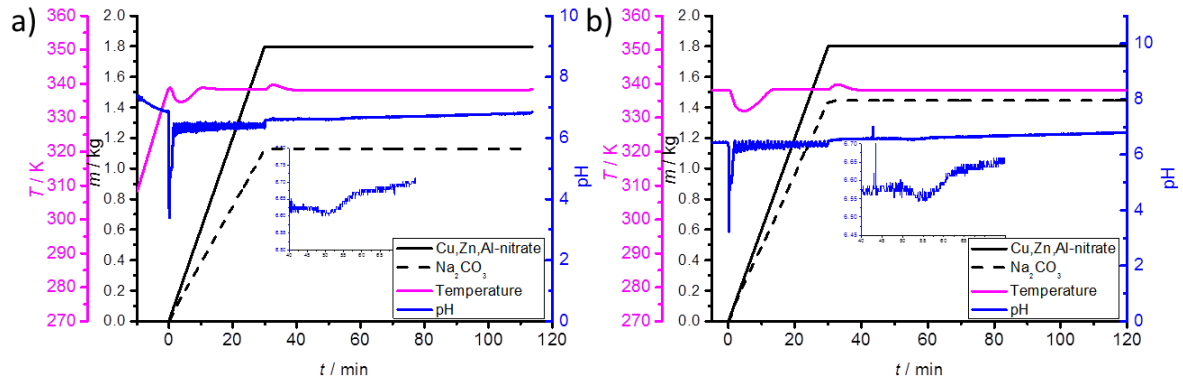

Figure S.5.1: Preparation protocols of reproduced samples with temerpature (pink), pH (blue) and masses of dosed solution (metal nitrate: black; base: dotted) develpoment. Inset shows the pH drop after 20 min after end of dosing.

Characterisation of reproduced samples

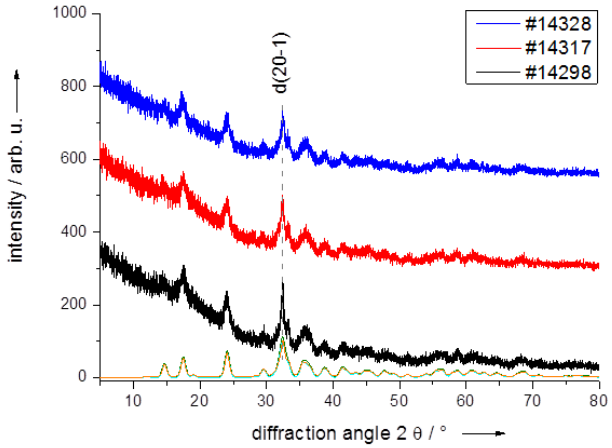

Figure S.5.2: XRD pattern of reproduced samples, with Rietveld-fits (bottom) starting from zincian malachite (icsd-code: 260813)

Table S.5.1: Characterisation of reproduced samples

#SN	BET / m^2g^{-1}	Average pore size / nm	Cu[a] / mol%	Zn[a] / mol%	Al[a] / mol%	Na[a] / mol%
14298	115	25	70.4	28.0	1.6	BDL[b]
14317	130	23	70.5	28.0	1.5	BDL[b]
14328	122	26	69.9	28.6	1.5	BDL[b]

[a] determined from XRF, metal based; [b] below detection limit

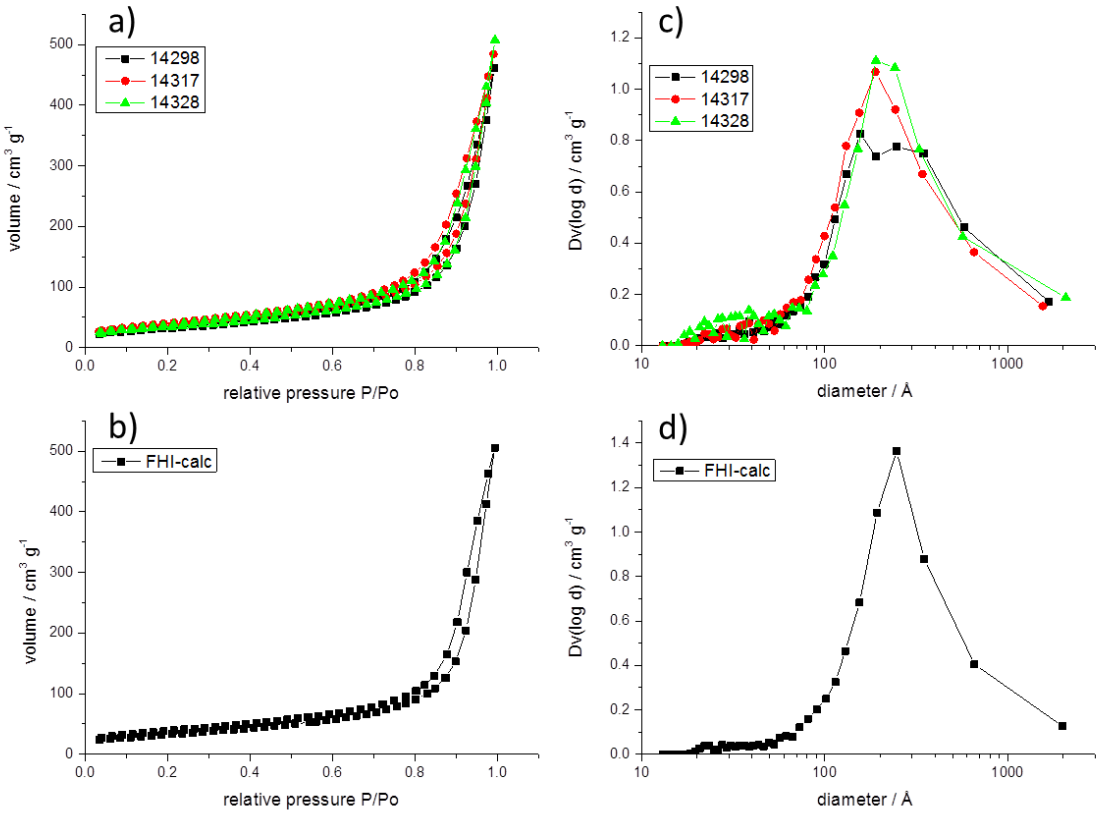

Figure S.5.3: N_2-physisorption isotherms of a) FHI-prec and b) FHI-calc. c), d) BJH-pore size distributions calculated from desorption branch of BET isotherm.

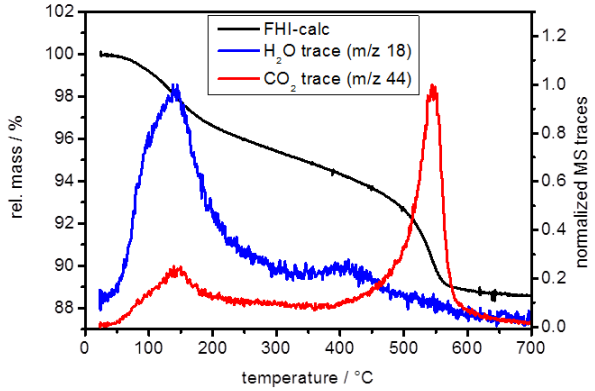

Figure S.5.4: TGMS curve of FHI-calc: mass loss (black), H_2O (blue) and CO_2-evolution (red).

Uncolored versions of microscopy images

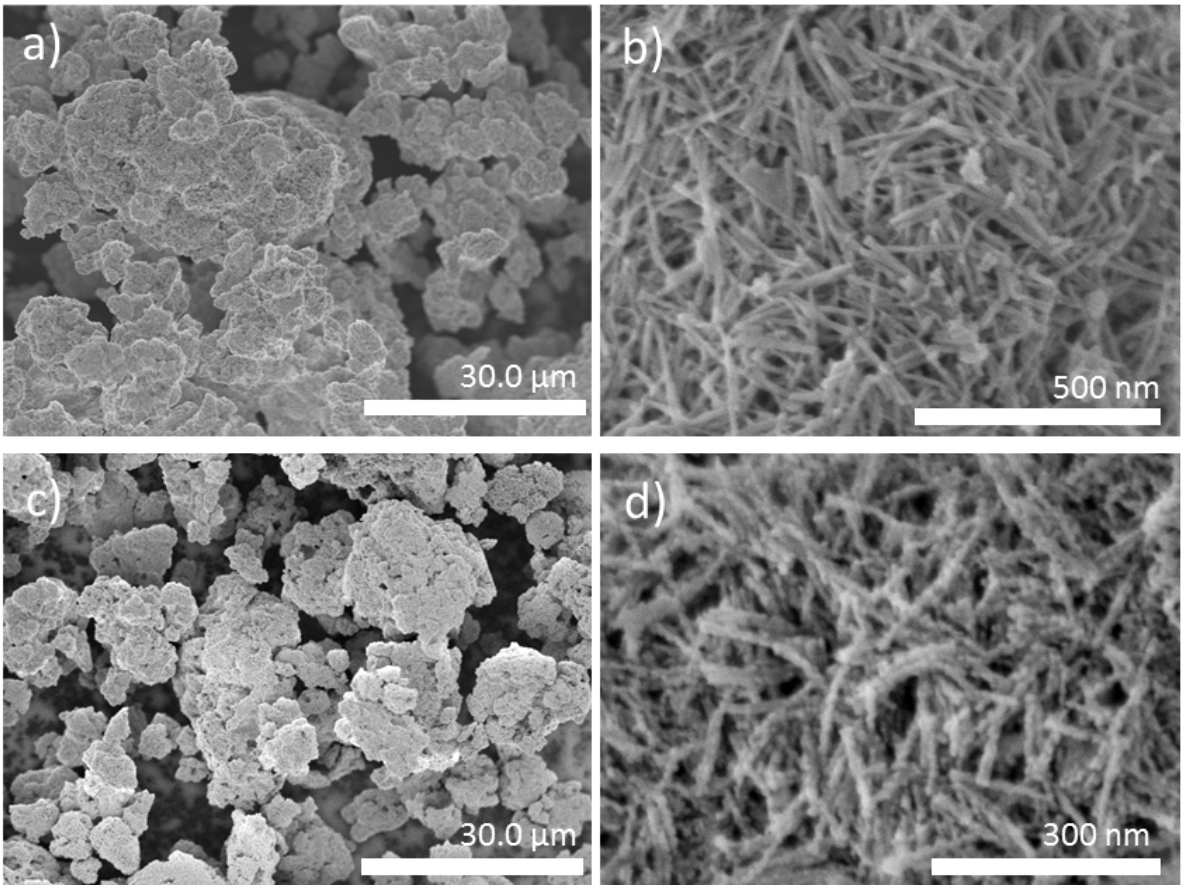

Figure S.5.5: SEM images of FHI-prec (a,b) and FHI-calc (c,d) at different magnification (uncoloured version).

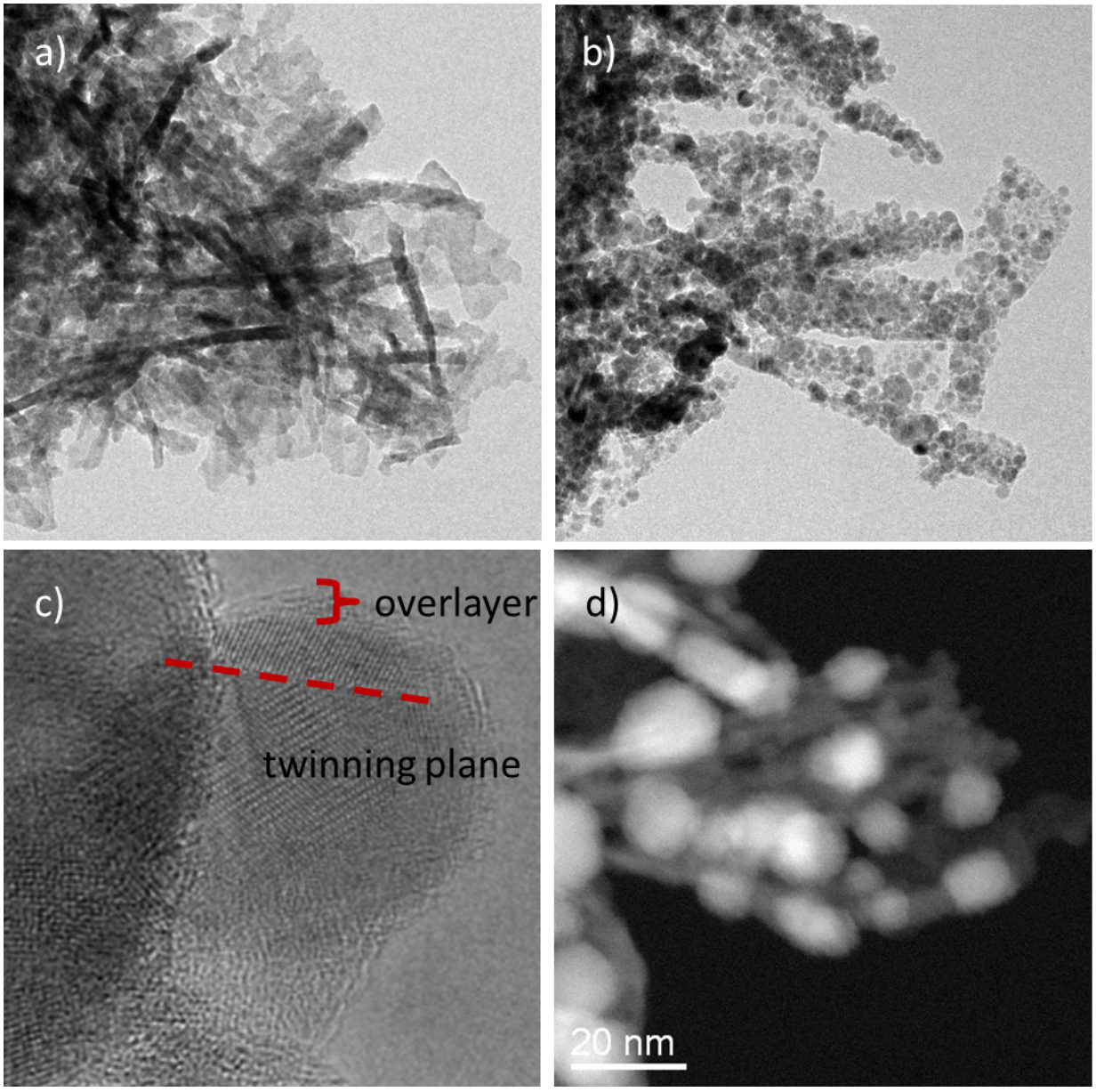

Figure S.5.6: TEM micrographs of FHI-calc (a) and FHI-red (b-c). HRTEM of a Cu nanoparticle with defects (c) and HAADF-STEM image (d) (uncoloured version).

NEXAFS spectra

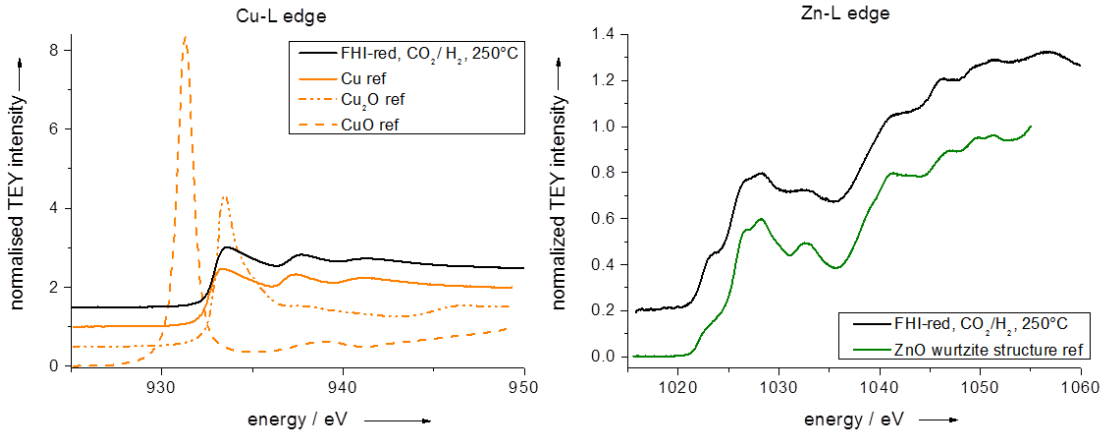

Figure S.5.7: NEXAFS spectra of FHI-red under rWGS in situ conditions (black) at 523 K and reference spectra.

Results of the formal thermokinetic analysis of the reduction process

The kinetic parameters of each step were determined using the model-free isoconversional Osawa-Flynn-Wall method and refined using a non-linear regression (NLR) least-squares procedure for different types of conversion functions f(α). The change in the reduction rate as a function of temperature can be described with Arrhenius non-isothermal equation (5.4) as follows:

$$-\frac{d\alpha}{dT} = \frac{A_0}{\beta} e^{-E_a/RT} f/(\alpha) \tag{5.4}$$

where A_0 is the preexponential factor s^{-1}, E_a is the apparent Activation energy in kJ mol^{-1}, T is the temperature in Kelvin, $\beta = dT/dt$ is the heating rate in K/min, and f(α) is some function of the conversion of the reaction characterising its mechanism. The conversion α, is defined as the fraction of the initial reagent A that has reacted by time t and changes from 0 to 1. The process is represented by two consecutive step model reaction model A $\longrightarrow$ B $\longrightarrow$ C, where both stages are adequately described by autocatalytic Prout-Tompkins equation f(α)=$(1-\alpha)^n \cdot \alpha^a$, a is the product reaction order and n is the reagent reaction order. Contribution of reaction A in the whole process is approx. 40%. Kinetic parameters for each stage of the whole process are listed in Table S.5.2.

Table S.5.2: Kinetic parameters and standard deviation

Stage	Log A	Ea / kJ mol^{-1}	n	a
1	3.1 ±1.0	45.2 ±8.4	1	0.9
1	1.7±0.5	29.9±5.1	1.5	0.7

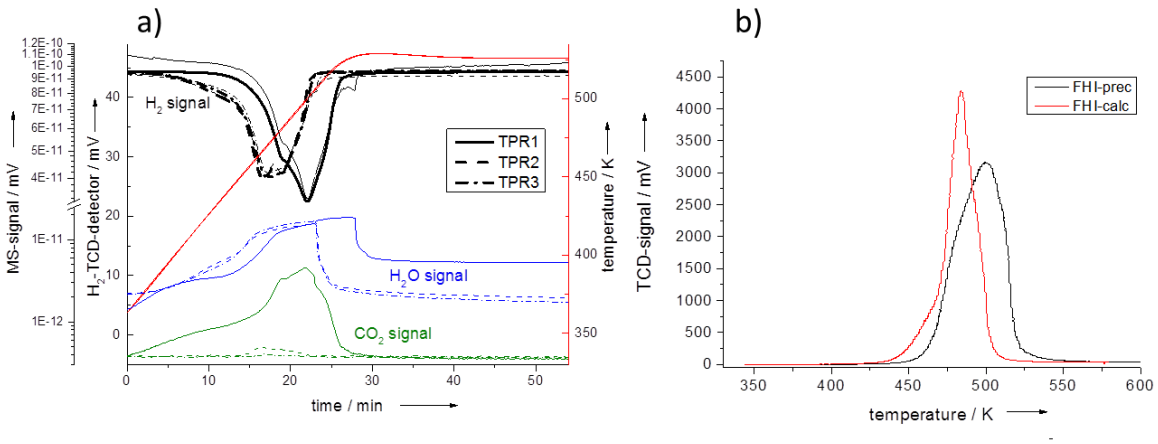

Figure S.5.8: a) *Effluent gas composition obtained from 3 subsequend TPR cycles with H_2-consumption (thin black lines: MS, thick black lines: TCD), H_2O evolution (blue: m/z 18), CO_2 evolution (green: m/z 44), Temperature (red); b) comparison of TPR-profiles of FHI-prec (black) and FHI-calc (red).*

Activity tests

The catalysts were tested in a plug-flow reactor under conditions ensuring no diffusion limitations. Nevertheless, the rate of methanol synthesis changed upon changes of the flow rate. For methanol synthesis from CO_2 it is known that product inhibition occurs (see Figure S.5.9, lower part), but also for syngas feed, there is a significant product inhibition, resulting in different methanol production rates for different feed flows (Figure S.5.9 upper part). The data reported in the main article were recorded at flow of 100 ml/min resulting in a conversion below 3.5% close to differential conditions.
Activation energies were determined from activities measured in a temperature range from 463 to 523 K. For the CO_2/H_2-feed, the activity at 523 K was deviating in the Arrhenius plot from the expected linear trend, and was therefore not included for the determination of the apparent activation energy. The deviation derives from some kind of limitation, probably from the stronger product inhibition at the higher conversion (although still low at 4%).

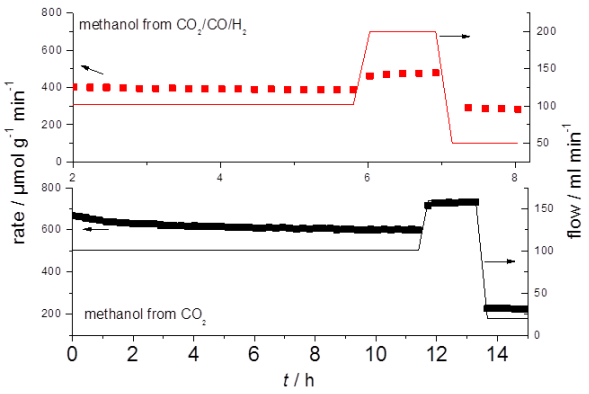

Figure S.5.9: Methanol rate at different flows and with different feed gases: CO_2/H_2 3:1 (black) and $CO_2/CO/H_2$ 8/6/59 (red).

Table S.5.3: Apparent activation energies for methanol determined for different feed gas compositions

	Activation energy / kJ mol^{-1}	
	$CO_2/CO/H_2/Ar$	**CO_2/H_2**
Methanol synthesis	56.7 ±2	57.3±3.1
RWGS		126±1

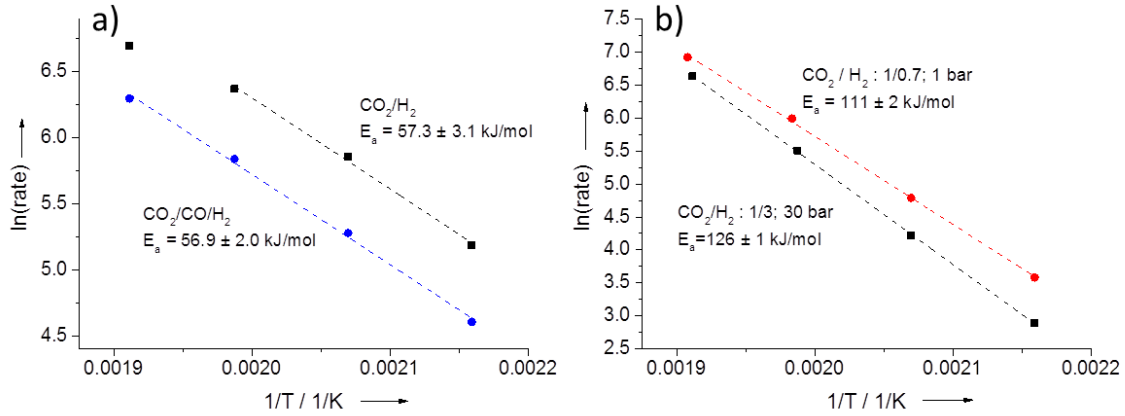

Figure S.5.10: Arrhenius plots for the different feed gases and products: a) methanol from CO_2/H_2 3:1 (black) and $CO_2/CO/H_2$ 8/6/59 (blue); b) CO from CO_2/H_2 at p=1 bar (red) amd p=30 bar (black).

FHI internal sample numbers

Table S.5.4: Internal sample numbers

		Reproductions
FHI-prec	# 14328	# 14298, # 14317
FHI-calc	# 15018	
FHI-red	# 14810 (neutron), # 15962, #15802 (TEM), # 15364 (BESSY)	

6 Promoting strong metal support interaction: doping ZnO for enhanced activity of Cu/ZnO:M (M = Al, Ga, Mg) catalysts

Julia Schumann, Maik Eichelbaum, Thomas Lunkenbein, Nygil Thomas, Consuelo Álvarez Galván, Robert Schlögl and Malte Behrens

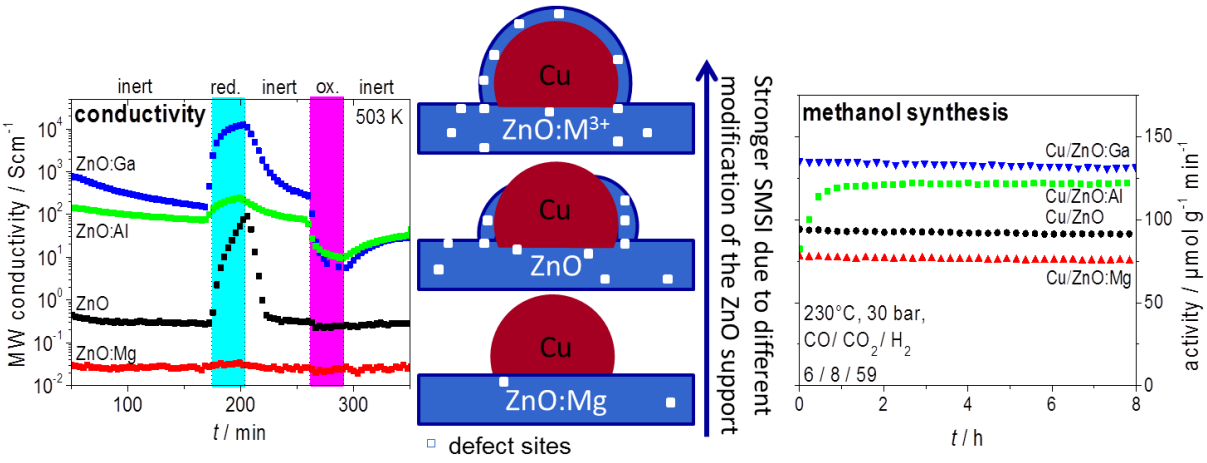

6.1 Abstract

The promoting effect of Al, Ga and Mg on the support in Cu/ZnO catalyst for methanol synthesis has been investigated. Different unpromoted and promoted ZnO supports have been synthesized and impregnated with Cu metal in a subsequent step. All materials, supports, calcined and activated catalysts have been characterized by various methods including contactless (microwave) conductivity measurements in different gas atmospheres.

Small amounts of promoters were found to have significant influence on the properties of the oxide support, concerning textural as well as electronic properties. We found correlations between the conductivity of the ZnO support and the activity of the catalyst in the reverse water gas shift reaction (rWGS) as well as in methanol synthesis. In rWGS the activation energy and reaction order in H_2 are decreased upon promotion of the ZnO support with the tri-valent promoters Al^{3+} and Ga^{3+} indicating an electronic promotion. In methanol synthesis, results point to a structural promotion by Al^{3+} and Ga^{3+}. A detrimental effect of Mg^{2+} doping was observed in both reactions. This effect is discussed in the context of the reducibility of ZnO under reaction conditions, which can be tuned by the promoter in different ways and are likely to affect the strong metal-support-interaction known to prevail in this catalyst.

6.2 Introduction

$Cu/ZnO/Al_2O_3$ catalysts are used industrially for methanol synthesis, one of the most important industrial processes in syngas chemistry. Cu is commonly regarded as the active phase, but the role of ZnO and Al_2O_3 is more than that of an inert support.[1–3] For a long time a synergistic effect of Cu and ZnO has been debated and different origins of the synergy have been discussed.[4] A hydrogen spillover mechanism, where ZnO acts as a reservoir for hydrogen facilitating the hydrogenation over adjacent Cu surfaces,[5,6] or the so-called strong metal support interaction (SMSI) which leads to a wetting of the ZnO under reducing atmosphere, covering the Cu particles, leading either to morphology changes[3,7,8] or supply of Zn atoms to the copper surface,[9,10] were considered. Recently the Cu/ZnO synergy has been proven by microscopical and theoretical studies to result from reduced Zn species being an integral part of the active site in methanol synthesis, sitting on highly active Cu steps.[1] Less has been reported about the promotional effect of Al, which is still not very well understood. In general, small amounts of substances added to a catalyst, are called promoters if they beneficially affect the activity by modifying the physical structure, like crystallinity, surface or pore size, or the electronic structure of the catalyst.[11] We assume that structural promoters increase the number of active sites but only electronic promoters would have an influence on the activation energy and reaction order of a catalytic reaction. In Cu/ZnO catalyst preparation alumina was found to be a component, which improves the morphology and stability of the catalysts as a structural promoter.[12] On the other hand, small amounts of Al^{3+} also change the metal surface area-normalized or intrinsic activity

of Cu/ZnO catalysts in methanol synthesis.[13] NMR spectroscopy revealed that small amounts of Al^{3+} are actually incorporated into the ZnO lattice, occupying tetrahedrally coordinated sites,[14] similar as in doped semiconductors for optical applications and are thus not assumed to modify the active copper part of the catalyst. The popularity of ZnO in semiconductor applications derives from its convenient properties as the direct wide band gap (3.3 eV) and large exciton energy (60 mV) which make ZnO especially promising for optoelectronic applications.[15] For the preparation of n-type ZnO, doping with Group XIII elements as Al3+ and Ga3+ is commonly applied in order to increase conductivity and alter the electronic structure.[15] The effect of these doped ZnO species on the above mentioned SMSI effect in Cu/ZnO is still not unambiguously resolved. Herein, we report a model study to better understand, whether the electronic structure of ZnO altered by promoters such as Al^{3+} or Ga^{3+} influences the extent of the SMSI with Cu for the reverse water-gas-shift (rWGS) or methanol synthesis. Therefore we have decoupled the promotion from the typical hydroxy-carbonate precursor chemistry commonly applied for the preparation of industrial-like Cu/ZnO:Al catalysts and synthesized doped model supports ZnO:M (M = Al, Ga, Mg) without Cu. These supports were thoroughly characterized before and after loading with the copper phase in a subsequent step by impregnation. By contactless conductivity measurements and UV-visible spectroscopy, amongst other characterization techniques, insights into the electronic structure of the support and the role of different promoters were gained. The impregnated support was tested in the rWGS reaction and methanol synthesis and the catalytic data were correlated with the electronic properties.

6.3 Experimental

Sample preparation: Differently promoted ZnO supports (3 mol % M: Al, Ga, Mg) were prepared by (co-) precipitation of the appropriate amount of metal nitrates (1 M) and Na_2CO_3 solution (1.6 M) in an automated reactor (Labmax). The precipitate was aged, washed, spray dried and calcined at 603 K (2 K min^{-1}, dwell time 180 min). The promoter amount of 3 % based on $[M^{2/3+}]/([M^{2/3+}]+[Zn])$ was shown previously to lead to a significant change in structural and catalytic properties.[13,14] Copper was impregnated on the ZnO samples using the copper citrate route: Cu-citrate was dissolved in an ammonia-containing solution, 2 mL of copper containing solution were added to 1 g of support, the slurry was stirred and dried overnight and calcined at 603 K under static environment

(2 K min^{-1} heating ramp, 180 min) resulting in a Cu loading of 10%. In case of unpromoted ZnO also 5 and 15% Cu loading were prepared.

Characterisation methods: Powder X-ray diffraction (XRD) patterns of the calcined samples were recorded on a STOE Stadi-P diffractometer equipped with a primary focusing Ge monochromator (Cu $K_{\alpha 1}$ radiation) and a linear-position-sensitive detector. The sample was mounted in the form of a clamped sandwich of small amounts of powder fixed with a small amount of grease between two layers of thin polyacetate film. Pattern fitting and phase analysis were carried out using the Rietveld method as implemented in the TOPAS software package.[16] X-ray fluorescence spectroscopy (XRF) was performed in a Bruker S4 Pioneer X-ray spectrometer.

Temperature programmed reduction (TPR) of the calcined sample was performed in a fixed bed reactor (TPDRO-1100, CE instruments), in 5 vol% H_2 in Argon at a heating rate of 6 K min^{-1} (40 mL min^{-1}, end temperature 623 K, holding time 30 min). The H_2 consumption was monitored with a thermal conductivity detector. Specific surface areas were determined by N_2 physisorption in a Quantachrome Autosorb-1 machine. Prior to analysis, the samples were degassed for 2 h at 353 K. N_2O chemisorption capacities were determined using the N_2O-reactive frontal chromatography (RFC) method.[17] Approx. 100 mg of calcined sample (sieve fraction) was placed in a fixed bed reactor, after in-situ reduction, 10 mL min^{-1} of a 1 % N_2O in He mixture used at room temperature. The N_2O-capacity and the apparent Cu-SA_{N2O} were calculated from the MS signal of the N_2 trace (m/z = 28). H_2-transient adsorption (TA) was performed in the same setup that was used for N_2O-RFC and performed similar as described in Ref.[18] For approx. 100 mg of sample, H_2-TA was recorded at room temperature in 20 ml min^{-1} 5 % H_2 in Ar for one hour each, for the calcined sample (CuO), the reduced sample (Cu) and the sample after N_2O-RFC (Cu_2O) after thorough purging in argon. Under the assumption that H_2 reacts only with surface Cu_2O, the area between the Cu and Cu_2O transient adsorption branch was integrated and the amount of consumed H_2 was quantified to deduce the Cu-SA_{H2TA}.

Scanning electron microscopy (SEM) images were taken on a Hitachi S-4800 field emission gun (FEG) system. High angle annular darkfield- scanning transmission electron microscopy (HAADF-STEM) images were taken on a FEI Titan 80-300 equipped with a Cs corrector at 300 kV. Prior to TEM investigation, the sample was reduced up to 523 K and transferred with a vacuum transfer holder (GATAN) under inert conditions to the microscope.

UV-vis-NIR spectroscopy was performed under in-situ conditions. UV-vis spectroscopy was recorded on a Perkin-Elmer Lambda 650 High Performance Spectrometer equipped with a Harrick Praying Mantis diffuse reflectance attachment and a high temperature (up to 923 K) in situ cell, which was connected to a gas delivery system. The band gap energy was calculated by linear extrapolation of the function $[F(R)\ h\nu]^{1/2}$ versus $h\nu$ to 0, as suggested by Weber[19] and Iglesia and co-workers.[20–22] This procedure results from a linearization of the theory of direct and indirect band gap transitions in semiconductors[23] and is explained in detail by Barton et al.[22] The reduced catalyst was characterized by X-ray photoelectron spectroscopy (XPS) at the ISISS beamline of the synchrotron facility BESSY-II of the Helmholtz-Zentrum Berlin (HZB). The samples were mounted in the glovebox and transferred under inert conditions. A depth profiling experiment was performed to estimate the distribution of the metals as a function of information depth. To do so, Cu 3p, Zn 3p and Al 2p, Mg 2p, Ga 3d core levels were recorded at various photon energies yielding electron kinetic energies of 180, 400, 800 and 1100 eV.

Methanol synthesis from syngas- and CO_2/H_2-feed was tested in a fixed bed flow reactor. 50 mg (100-200 μm, diluted with 0.7 g of SiO_2) were loaded into a 6 mm inner diameter stainless steel reactor tube. The catalysts were reduced at 523 K (1 K min^{-1}) for 1.5 hours in 20 % H_2 in Ar. Upon completion of the reduction, the reactor was cooled to 503 K, and a 3:1 H_2/CO_2 mixture (100 mL min^{-1}) containing 4 % Ar (as internal standard) was introduced into the reactor. Online analysis of products was performed with a gas chromatograph (Agilent 7890A). Performance under syngas conditions was tested in the same set up after increasing the pressure to 30 bars. The feed gas contained 6 % CO, 8 % CO_2, 59 % H_2 and balance inert gas. RWGS was carried out also under a H_2/CO_2 1/1 gas mixture in an 8-fold parallel reactor setup. Tubular quartz glass reactors with an inner diameter of 6 mm were used. Each reactor was placed inside a programmable furnace and the temperatures were measured using type K thermocouples placed in the catalyst beds. 20 mg catalyst was diluted with SiC, to improve heat transport and prevent hotspot formation. Prior to the activity tests, the samples were reduced in situ in a 5% H_2 in N_2 flow (30 mL min^{-1}) with a heating ramp of 1 K min^{-1} to 523 K and a holding time of 30 min.

Conductivity measurements were performed by applying the contact-free and noninvasive microwave cavity perturbation technique. The newly developed conductivity setup and the measurement principle were described in detail recently[24,25] and allow the investigation of the charge transport at microwave frequencies in catalysts in a fixed bed reactor at elevated temperatures. As resonator a cylindrical X-band TM110 silver-plated brass cavity

(ZWG Berlin-Adlershof; resonance frequency: 9.2 GHz) with a height of 19.5 mm and a diameter of 38.5 mm was used. A quartz tube reactor with 4 mm outer and 3 mm inner diameter containing the sample under investigation (100-200 μm sieve fraction of pressed and sieved ZnO powder samples, catalyst bed length: 10 mm, fixed with quartz wool plugs), surrounded by a 10 mm outer diameter double-walled evacuated quartz dewar mantle to protect the resonator from convection heat, was directly placed in the center of the cavity. This quartz tube flow through reactor was connected upstream to a gas delivery manifold equipped with mass flow controllers (Bronkhorst El-Flow) to supply the different gas mixtures with a total flow of 20 mL/min. Heating of the reactor was performed by preheating a stream of 8 L/min N_2 gas in a resistive furnace consisting of a Sylvania tungsten series I heater. Downstream of the heater, the N_2 stream was flowing between the quartz dewar mantel and the outer wall of the reactor tube. The temperature at the catalyst was controlled by a type K thermocouple inside the reactor and a PID controller (Eurotherm 3216) regulating the furnace. The cavity was connected via a W90 waveguide and a flexible SMA coaxial cable with a vector network analyzer (Agilent PNA-L N5230C-225) in order to record resonance spectra of S11-parameters in reflection mode (microwave power attenuation: 11 dBm). With a Smith chart analysis of the complex reflection factor and by applying transmission line theory the unloaded quality factor and resonance frequency were deduced for every measurement point. From the change of the quality factor with and without sample the imaginary part of the effective permittivity was calculated. After applying the Landau-Lifshitz-Looyenga effective medium theory the permittivity of the solid and finally the conductivity was calculated.[25]

Continuous-wave EPR spectra were recorded on a Bruker ESP 300 E spectrometer operating at the X-band frequency range and equipped with a Bruker ER 4116 DM (TE102 mode) resonator and a Bruker ER 042 MRH E microwave bridge. Samples were measured in Wilmad® quartz (CFQ) EPR tubes (o.d. 4 mm) at 293 K using a microwave frequency of ca. 9.64 GHz, microwave power of 20 mW, a modulation frequency of 100 kHz and a modulation amplitude of 0.95 G. The microwave frequency was measured with an Agilent 20 GHz Microwave Frequency Counter 53150A. For a quantitative comparison of the signal intensities of the different samples an external Cr^{3+}/MgO standard (in a thin capillary) was introduced into the resonator in addition to the sample tube. The shown and evaluated EPR spectra were normalized to the maximum of the Cr^{3+} signal (at a g-factor of 1.9796) of this standard.

6.4 Results and discussion

6.4.1 Sample characterization

Zinc-hydroxy carbonate precursor phases with and without 3 mol % (based on $M^{3+/2+}$ + Zn^{2+}) of Al^{3+}, Ga^{3+} or Mg^{2+} promotors were synthesized by co-precipitation. Calcination at 603 K yielded nano-crystalline ZnO (see Figure 6.1a). In XRD no crystalline minor phases were observed, which indicates that the added promoters do not form crystalline segregated by-phases, and should be incorporated into the ZnO crystal lattice. The calculated lattice parameters from Rietveld refinement are given in the supporting information (see Table S.6.1 in section 6.8). Various effects of promoter incorporation were observed for different promoting ions. Incorporation of Al^{3+} led to a contraction of the unit cell, which agrees with the assumption that Al^{3+}, with a smaller effective ionic radius (IR = 0.39 Å)[26], replaces Zn^{2+} (IR = 0.60 Å)[26] on tetrahedral sites. It was also shown before by solid state NMR, that at an Al content of 3 % a substantial fraction of Al^{3+} ions occupy tetrahedrally coordinated sites in the ZnO structure.[14] Similar solubility limits of Al^{3+} in ZnO were reported by other groups,[27,28] although also much lower limits have been reported using different preparation routes.[29] On the contrary, for Ga incorporation into ZnO an expansion of the lattice parameter a was observed. Ga^{3+} (IR = 0.47 Å)[26] has a larger ionic radius than Al^{3+} (0.39 Å) and thus might occupy the larger octahedral sites.[30] In literature values as high as 20 % Ga incorporation into ZnO without byphase formation have been reported.[31] ZnO:Mg displayed the lattice constants closest to the unpromoted sample as Mg^{2+} also is most similar with respect to size (IR = 0.57 Å)[26] and valency to Zn^{2+}. It was reported, that MgO forms a separate phase at 10 % but for 5 % Mg, a single phase ZnO was reported.[32] A significant influence of the promoter onto the ZnO morphology was observed. Calculated ZnO domain sizes were between 7 and 13 nm, with the unpromoted ZnO having the largest domain size, Mg and Al-promoted ZnO having slightly decreased domain sizes and Ga promoted ZnO having the smallest domain size, decreased by 50 % compared to the unpromoted sample (see Figure 6.1, Table 6.1). The promoter-induced defects seem to hinder large particle growth or destroy the long-range crystallographic order.

After the impregnation with 10 % of Cu and a further calcination step, the samples showed only small differences in the XRD pattern, compared to the state before the impregnation with CuO (see Figure 6.1). Only very weak broad signals can be seen, where the CuO (111) reflection is expected at around $38.6° = 2\theta$, which proved that the copper

oxide is finely dispersed. Rietveld fitting resulted in small CuO domain sizes of 2 - 5 nm. ZnO domain sizes were slightly increased with values between 8 and 13 nm (see Figure 6.1b, Table 6.1).

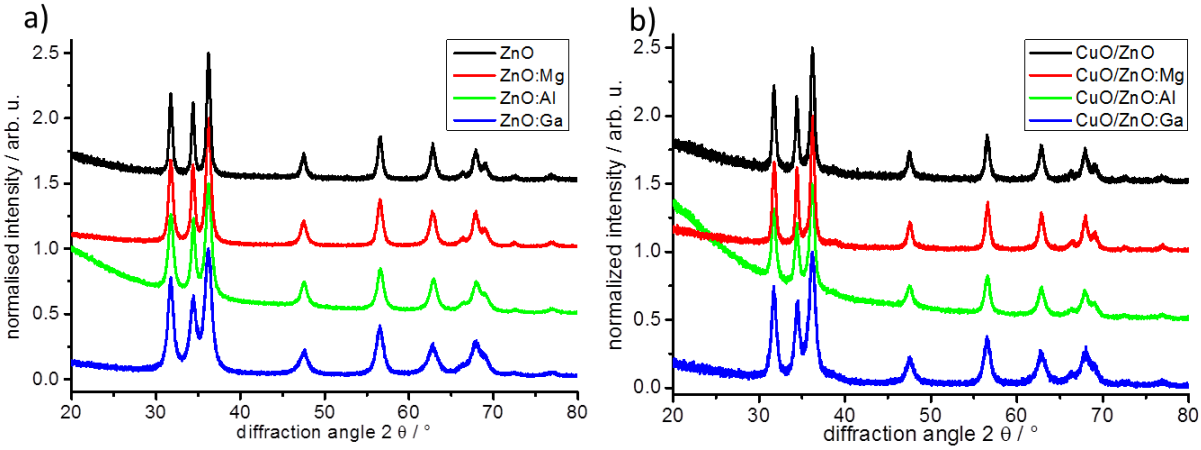

Figure 6.1: XRD pattern of a) ZnO:M and b) CuO/ZnO:M (M=Mg, Al, Ga).

Table 6.1: Sample characterization of bare supports and impregnated catalysts.

	Domain size ZnO[a](pure support) [nm]	**BET of support [m^2g^{-1}]**	**Domain size ZnO[a] after impreg. [nm]**	**BET after impreg. [m^2g^{-1}]**
ZnO	12.9	41	13.0	34±2
ZnO:Mg	9.9	60	12.7	47±5
ZnO:Ga	6.7	95	7.9	52±4
ZnO:Al	9.5	89	10.5	45±2

[a] L_{vol}-IB value as determined from Rietveld-fit.

The accessible surface area (SA), measured by N_2-physisorption (BET) well reflects the trend already observed for the ZnO domain sizes. The unpromoted sample with the largest domain sizes exhibited the smallest surface area, whereas ZnO:Ga had the largest surface area (see Table 6.1). Doping with Mg^{2+} increased the SA a bit compared to the unpromoted sample, and promotion with Ga^{3+} and Al^{3+} more than doubled the SA. After impregnation with CuO the BET surface area was reduced for all samples and the differences between the differently promoted samples were not that big any more. The amount of Cu loaded onto the support was checked with XRF measurements and found to be close to the nominal value (Table 6.2). The small deviations in Cu loading probably

originate from different uptake of physisorbed humidity and CO_2 of the supports leading to weighing errors during catalyst preparation. The N_2O-chemisorption capacity measured by the N_2O-RFC method,[17] was between 50 and 85 μmol g^{-1} (corresponding to apparent Cu-SA_{N2O} of 4-7 m^2 g^{-1}) for the different samples (see Table 6.2). Different loadings from 5 to 15 % Cu on the unpromoted sample showed, that the N_2O capacity scales linear with the amount of Cu within the uncertainty of the measurement, thus indicating that the impregnation was not limited by the available support SA within the loading regime studied here.

As the N_2O-RFC method does not only probe the Cu-surface atoms, but also oxygen vacancies or partly reduced Zn species,[18,33] the Cu-SA was measured with a method called H_2-transient adsorption (TA). The number of sites measured by H_2-TA were all smaller than those measured by N_2O-RFC, with values between 40-65 μmol g^{-1}, corresponding to 3.3 m^2 g^{-1} for Cu/ZnO:Mg and 5.3 m^2 g^{-1} for Cu/ZnO:Ga. The theoretical maximum Cu-SA value, which can be expected for samples with the measured loadings of 8.5 - 10.8 % Cu and a particle size of about 10 nm (see below), is 5.7-7.3 m^2 g^{-1}, which leads to the reasonable assumption that the interface ratio of the particles is between 27 and 42 %. From the difference of the two measurement methods the number of oxygen vacancies at the surface of ZnO can be calculated. The highest values of 20 μmol g^{-1} was found for the Cu/ZnO:Ga sample, similar to Cu/ZnO:Al and Cu/ZnO. For Cu/ZnO:Mg this number was much lower with only 8 μmol g^{-1} indicating a different impact of the Mg^{2+} promoter onto properties of the ZnO component as shown below (Table 6.2).

Table 6.2: Cu content, Cu-SA determined by N_2O-RFC and H_2-TA and oxygen vacancies after reduction to 523 K.

	Cu added by impreg.[a] [wt%] (nominal value)	**N_2O-capacity (Cu- SA_{N2O}**[b]**)** [μmol g^{-1}]([m^{2}g^{-1}])	**Cu-$SA_{H2\text{-}TA}$**[c] [m^{2}g^{-1}] ([μmol g^{-1}])	**Oxygen vacancies** [μmol g^{-1}]
Cu/ZnO	9.4 (10)	67 (5.7 ± 0.2)	4.1 (50)	17
Cu/ZnO:Mg	8.5 (10)	51 (4.1 ± 0.1)	3.3 (41)	8
Cu/ZnO:Ga	10.8 (10)	86 (7.0 ± 0.1)	5.3 (64)	20
Cu/ZnO:Al	9.3 (10)	73 (5.9 ± 0.1)	4.4 (54)	18

[a]determined from XRF measurements
[b]metallic Cu-SA assuming a stoichiometric reaction of N_2O with Cu-surface atoms
[c]metallic Cu-SA assuming a stoichiometric reaction of H_2 with Cu_2O-surface atoms after oxidation of Cu surface with N_2O

SEM gave further insights into the microstructure of the samples (see Figure 6.2). The ZnO prepared by precipitation of Hydrozincite precursor exhibited a platelet-like and porous morphology assembling into spherical aggregates. Al-promotion did not influence the morphology drastically. However, the platelets appeared thinner rendering a more sheet like occurrence. Impregnation with Cu and re-calcination changed the morphology (see Figure 6.2e) and f)) towards more granular particles. For Al-promoted samples, the platelet morphology seemed to be less altered by this step. The reduced samples Cu/ZnO and Cu/ZnO:Al have been further investigated with HAADF-STEM (see Figure 6.3 and Figure S.5.3). The images reveal that the Cu nanoparticles (<10 nm, red) are dispersed on highly porous ZnO (yellow) supports.

With diffuse reflectance UV-vis spectroscopy optical band gaps of the supports were estimated. It was found that Mg^{2+} increased the apparent optical band gap of ZnO, whereas Al^{3+} and Ga^{3+} led to a decrease of the optical band gap (see Figure 6.4 and Table 6.3). This is in agreement with the observed color of the samples. ZnO:Mg was whitest, whereas ZnO:Ga and ZnO:Al were yellow in color. This can be interpreted as formation of defect states by Ga^{3+} and Al^{3+} in the band gap as is expected for trivalent dopants in n-type semiconductors, while Mg^{2+} makes ZnO more insulating. Upon heating the sample in inert gas to 503 K the band gap decreased by 70 - 120 meV. This is a result of two effects: expansion of the lattice parameters and to about 35 mV due to the thermal excitation of electrons and holes.[14,23] Change of the atmosphere at 503 K, either reducing or oxidizing, did not alter the optical band gap significantly at the temperature and time scale studied.

Table 6.3: Bandgap energies.

	Optical band gap[a] at RT [eV]	**Optical band gap[a] at 503 K [eV]**
ZnO	3.12 ± 0.12	3.03 ± 0.05
ZnO:Mg	3.20 ± 0.08	3.13 ± 0.05
ZnO:Al	3.07 ± 0.04	2.99 ± 0.02
ZnO:Ga	3.03 ± 0.05	2.91 ± 0.04

[a]As determined from Tauc-plot; errors are determined from uncertainty of linear fit.

Temperature programmed reduction (TPR) was performed to give further insight into the reducibility of the system e.g. by formation of oxygen vacancies. The pure supports showed a very weak reduction signal (see Figure 6.5a). Undoped ZnO started to reduce first, and ZnO:Mg showed the weakest and latest reduction signal. A relative strong

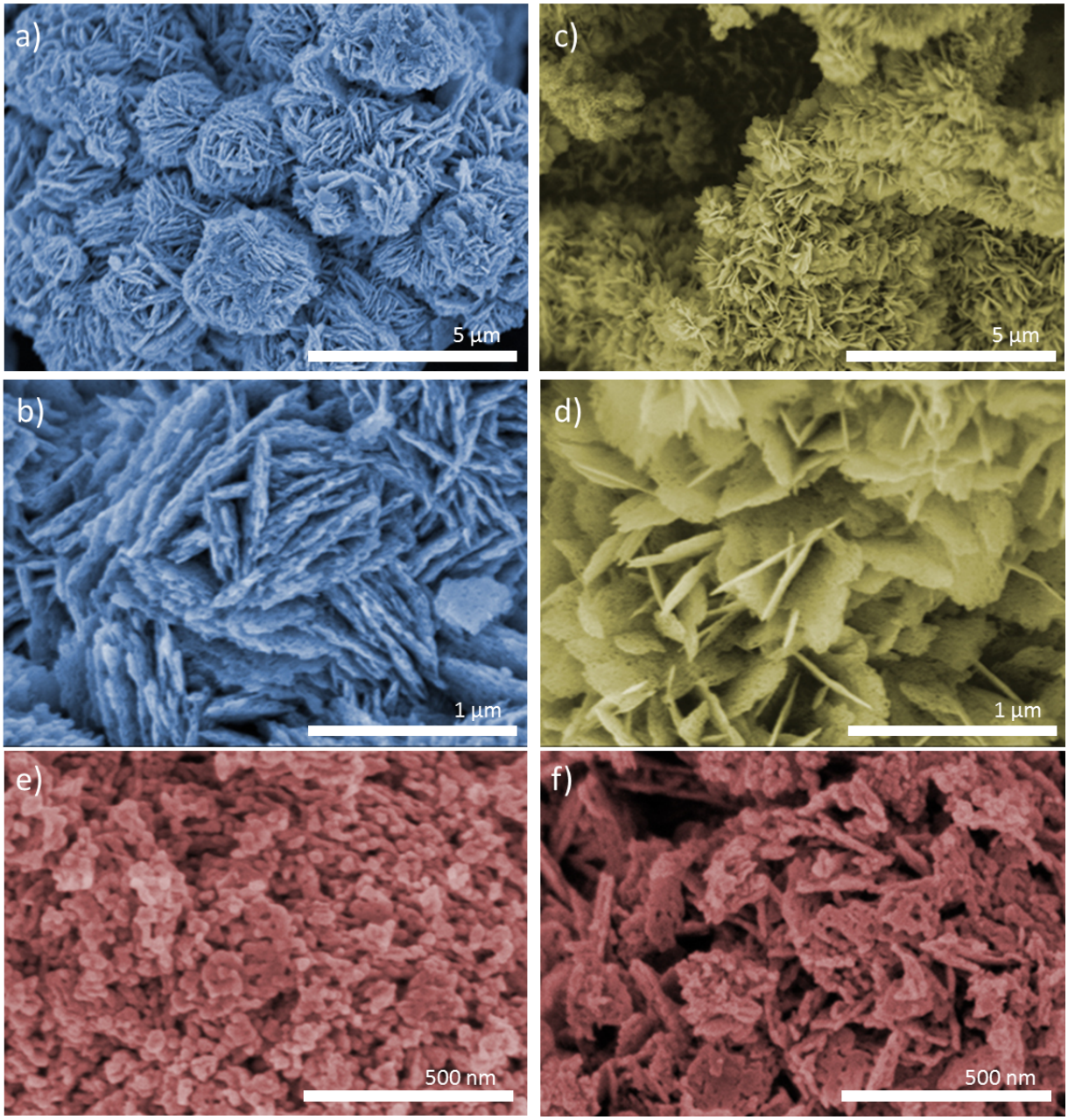

Figure 6.2: SEM images of ZnO:M supports: a),b) ZnO and c),d) ZnO:Al and of impregnated samples: e) CuO/ZnO and f) CuO/ZnO:Al.

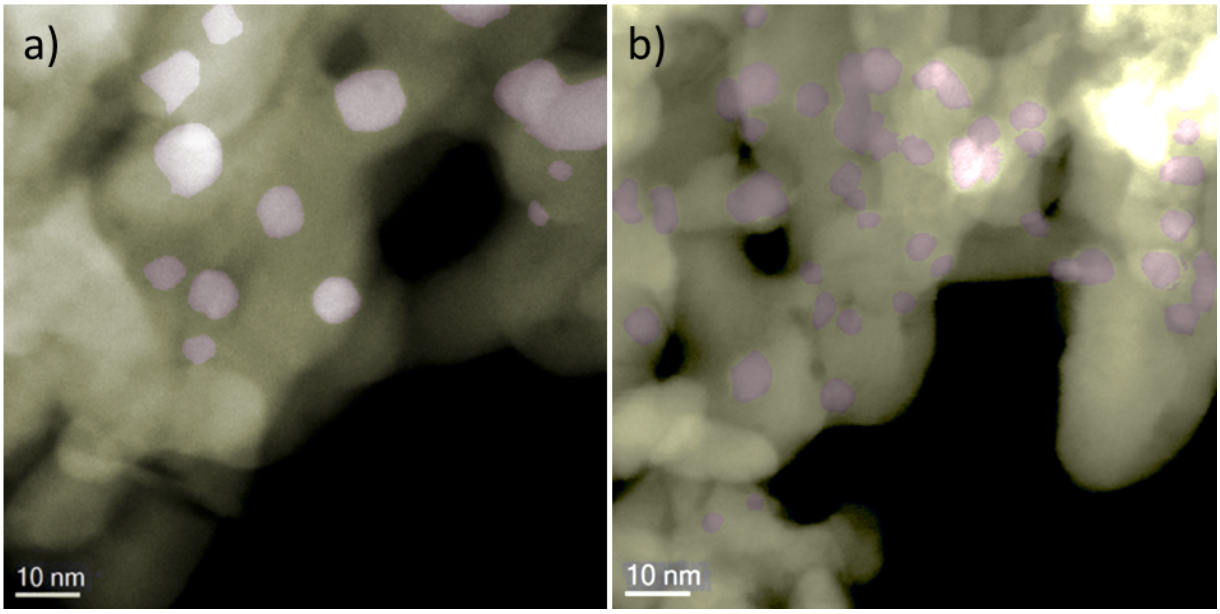

Figure 6.3: Colourized HAADF-STEM micrographs of a) Cu/ZnO and b) Cu/ZnO:Al. Within the images ZnO moieties are highlighted in yellow, whereas Cu particles are presented in a red colour. The original images are given in Figure S.6.3 in section 6.8.

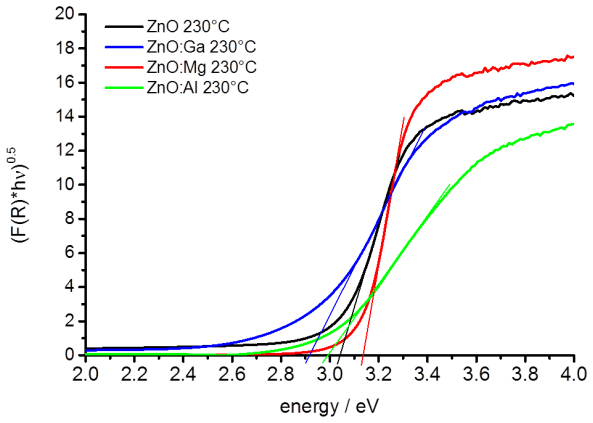

Figure 6.4: Tauc-plots for band gap estimation from UV/Vis spectra.

reduction signal around 460 K was present for ZnO and ZnO:Ga. This might be attributed to the reduction of singly occupied oxygen vacancies in the ZnO lattice as suggested by correlation with EPR results (see below). The profiles of the impregnated samples showed the successful deposition of nano-crystalline CuO, which was reduced at temperatures between 480 and 500 K depending on the support (see Figure 6.5b). These values agree well with reduction peak maxima reported for other systems with nano-crystalline CuO particles.[34,35] All peaks featured a strong shoulder at the low temperature side of the main peak. A similar shape was observed for the reduction of Cu-catalysts derived from a Cu,Zn,Al-layered double hydroxide (LDH) precursor.[36] The shoulder of this ex-LDH catalyst was assigned to the first step of the reduction of Cu(II) $\longrightarrow$ Cu(I) $\longrightarrow$ Cu(0) and caused by a strong interaction of Cu and oxide matrix, which kinetically stabilizes the Cu(I) intermediate.[36] A similar effect was seen here, which indicates a strong interaction between the Cu-species and the ZnO:M supports. A strong interaction between support and Cu-component was also confirmed by the non-additive behaviour of the reduction signals. The broad reduction signals of the support around 550 K have vanished in the impregnated samples (see Figure 6.5c). Furthermore, the much stronger contribution of the Cu-component to the reduction profile was significantly influenced by the promoter in the support, which also requires a strong interaction. The reduction onset temperature was lower for CuO than for any of the ZnO:M supports, as can be expected for the much nobler element Cu. Already the onset temperature of the CuO reduction was influenced by the promoter species. CuO/ZnO started to reduce first, around 400 K, and the promoted CuO/ZnO:M (M = Al, Ga, Mg) samples only started slightly later to reduce. Additionally, the main reduction peak is shifted from 480 K towards higher temperatures by 10 - 20 K in the order Ga<Al<Mg, as can be seen in the difference plots in Figure 6.5d. The medium shift of Al and Ga promoted CuO/ZnO:M might be explained by the formation of a more extended ZnO overlayer, compared to the unpromoted sample or an additional stabilization of the intermediate Cu(I) species by the SMSI, which might slow down the hydrogen consumption slightly. The reason for the strong shift of the reduction profile of CuO/ZnO:Mg is not so easy to understand. An explanation might be a lower hydrogen spillover effect, which might compensate for the weaker metal support interaction.

Quantification of the reduction signals under the assumption that only CuO was contributing to the hydrogen consumption yielded amounts between 10.7 and 14.1 wt % CuO. All samples showed a higher H_2-consumption than what would be expected from the XRF results, if only CuO contributed to the reduction signal. The contribution of the partial

reduction of ZnO to ZnO_{1-x} was higher for the impregnated CuO/ZnO:M than for the pure supports ZnO:M. A strong increase of the bulk reducibility of ZnO in the vicinity of Cu was observed, except for the Mg doped sample. Especially Al^{3+} seems to promote the oxygen vacancy formation in ZnO (see Table 6.4). These results for the bulk confirm the trend of the oxygen vacancies at the surface obtained from the different Cu-SA measurements earlier (Table 6.2). It becomes evident, that the promoter species influence both reduction processes, CuO $\longrightarrow$ Cu and ZnO $\longrightarrow$ ZnO_{1-x}. Furthermore the presence of Cu influences the reduction of ZnO $\longrightarrow$ ZnO_{1-x} and facilitates the formation of oxygen vacancies, by shifting it to lower temperatures and increasing the extent of vacancy formation. This phenomenon can probably be related to the SMSI effect, the formation of a ZnO overlayer on Cu, which is assumed to strongly facilitate the oxygen vacancy formation due to the driving force towards surface brass formation.

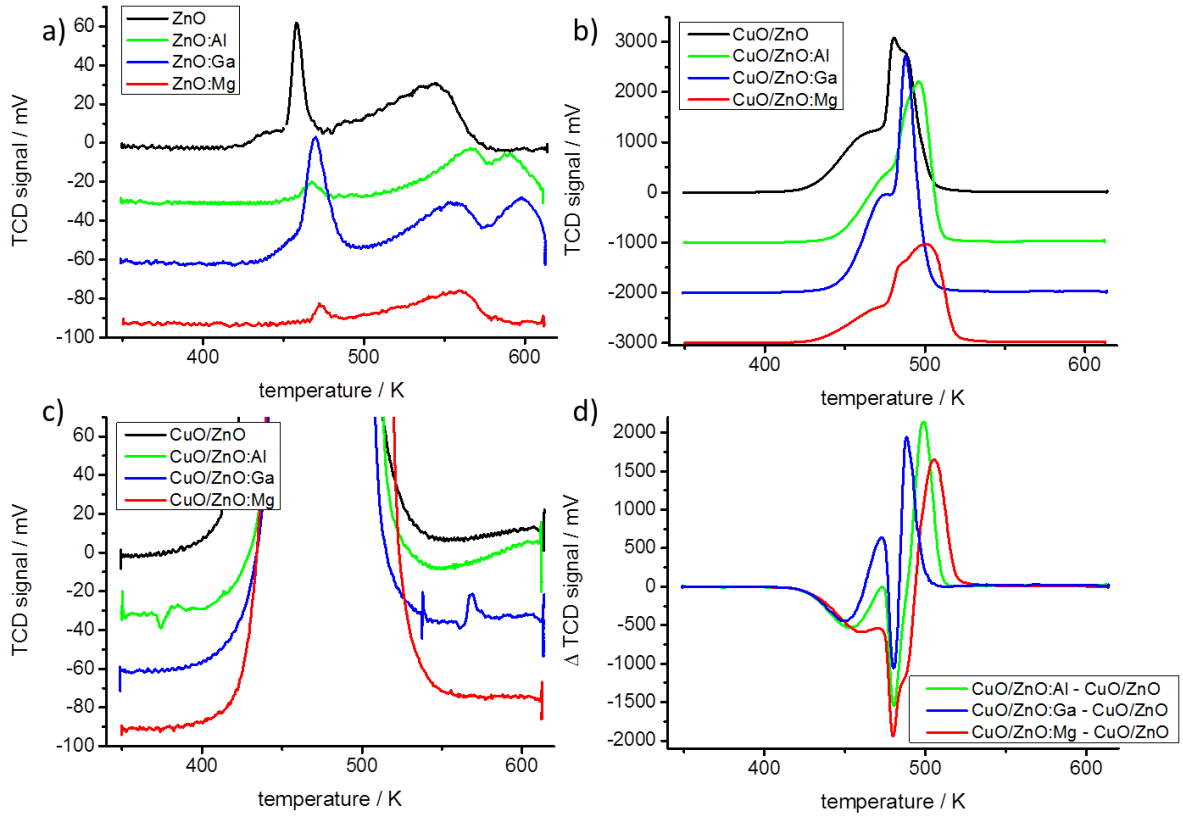

Figure 6.5: TPR profiles of a) pure ZnO:M supports and b) impregnated supports CuO/ZnO:M; c) detailed section of the profiles of CuO/ZnO:M; d) difference spectra of promoted samples CuO/ZnO:M relative to the unpromoted CuO/ZnO

Table 6.4: TPR results.

	H_2-consumption pure support [μmol g^{-1}]	**Reducible species pure support [%] (up to 623 K)**	**Calculated amount CuO (values from XRF) [wt%]**	**T_{max} [K]**	**Amount of reducible support species[a] [μmol g^{-1}]**
ZnO	46	0.4	12.7 (11.5)	480	151
ZnO:Mg	22	0.2	10.7 (10.4)	500	38
ZnO:Ga	74	0.6	14.1 (13.2)	488	113
ZnO:Al	37	0.3	13.0 (11.4)	496	201

[a]Calculated from difference of TPR and XRF CuO quantification.

Electronic properties

Using a contactless conductivity measurement technique based on the microwave cavity perturbation technique,[24] the conductivity of the supports in inert (N_2), reducing (5.2 vol % H_2 in N_2) and oxidizing (5.2 vol % O_2 in N_2) gas environments was measured at 503 K. The experiments were performed to identify the effect of the different dopant ions on 1) the absolute conductivity and 2) on the redox response of ZnO at the catalytically relevant temperature of 503 K. The results summarized in Figure 6.6a show that the conductivity behavior is strongly modified by the different dopants. The initial conductivity decrease for all samples during the first temperature ramp from room temperature to 503 K is unexpected for semiconductors, but could be explained by the desorption of residual water in the samples that gives also rise to a strong microwave absorption signal overlapping the original conductivity of ZnO. The decreasing conductivity during the final ramp from 503 K to room temperature shows indeed the expected temperature behavior of a semiconductor. ZnO is typically an n-type semiconductor with electrons as majority charge carriers, which explains the increasing conductivity in H_2 due to the donation of electrons into the material upon chemisorption or reaction. Interestingly, the conductivity of ZnO decreases already during the subsequent treatment in N_2, probably pointing to a rather weak adsorption of H_2 already desorbing in flowing N_2. The effect of O_2 is very small, leading only to a weak consumption of conduction electrons. The redox cycle is reversible as indicated by the repeated treatment in H_2 and O_2, though the conductivity increase is even more pronounced after the second H_2 treatment.

In ZnO:Al the conductivity rises by several orders of magnitudes compared to pure ZnO. The introduction of Ga induces an even higher absolute conductivity value. Both samples show as well an increasing conductivity in H_2, but in contrast to ZnO, exhibit also a decreased charge transport in O_2. The conductivities relax already in N_2 to the original values measured in inert gas, though the kinetics are significantly slower than in ZnO, suggesting a stronger adsorption of the gases in the doped materials. A completely different behavior is observed for ZnO:Mg. Mg^{2+} leads to both a decrease of the absolute value of the conductivity and to a totally extinguished redox response in H_2 and O_2. The effect of the dopants resembles very well the modification of the apparent band gap observed in the UV-vis spectroscopy experiments. Al and Ga with a preferred oxidation state of 3+ substituting Zn^{2+} in the crystal lattice are n-type dopants that create shallow donor states in the band gap of ZnO inducing a higher density of free charge carriers in the conduction band. This interpretation is supported by the observation of a decreased optical band gap. These donor states do not only increase the absolute conductivity, but can also strongly interact with H_2 and in particular with O_2 leading to an increased charge transfer with adsorbed molecules and hence to a stronger gas phase response of the conductivity. In contrast, Mg^{2+} apparently reduces the density of donor states significantly as also indicated by the increased optical band gap and hence decreases the absolute conductivity and quenches the interaction with H_2 and O_2. These findings indicate that the introduced dopants are strong electronic promoters for semiconducting ZnO. The interpretation that shallow donor states are formed by doping ZnO with Ga and Al is supported by EPR measurements. Figure 6.6b) clearly shows strong resonances at g values of 1.963 for Al and Ga-doped ZnO, which are attributed to shallow donor centers, typically ionized impurities,[37] in our case induced by the Al^{3+} and Ga^{3+} dopants. The pure ZnO and Mg-doped ZnO show only a very small resonance signal at this position, supporting the much lower concentration of donor states in these systems. A direct quantitative comparison is possible based on the double integral values of the signal depicted in the inset of Figure 6.6b.

There is a second, very broad resonance signal at lower magnetic field strength with a g-factor of 2.04 for ZnO and ZnO:Ga, which is close to the value reported for single electrons trapped in oxygen vacancies.[37] Interestingly this low-field resonance coincides with the occurrence of a (relatively) strong low-temperature reduction peak for the same two samples (compare with Figure 6.5a). This could indicate that the singly occupied oxygen vacancies are easily reducible species. Al^{3+} and Mg^{2+} doping lead to a strong decrease of this low-temperature reduction peak and of the EPR resonance signal around

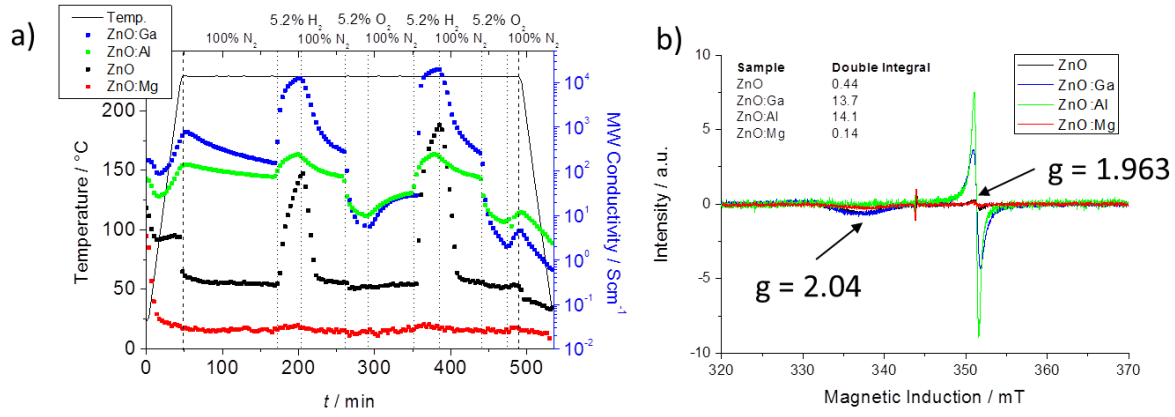

Figure 6.6: a) Microwave conductivity measurements of ZnO supports in different gas atmospheres at elevated temperatures; b) EPR measurements of the samples at 293 K under ambient conditions. The sharp signal at a magnetic induction of about 344 mT (g-factor: 1.9796) is from an external Cr^{3+}/MgO standard introduced into the resonator in order to normalize the intensity of the spectra to the maximum of this signal.

2.04. This corresponds to fewer singly occupied oxygen vacancies present in ZnO:Al and ZnO:Mg. Likely, the "hardness" of the smaller and highly charged cations Al^{3+} and Mg^{2+} leads to a stronger binding of lattice oxygen and thus prevents the formation of oxygen vacancies.[38] The different behavior of Al^{3+} and Ga^{3+} dopant, despite their similar valence electron configuration, could be explained by the difference in polarizability and ionic radii of the dopants, properties in which Ga^{3+} is much more similar to Zn^{2+} compared to Al^{3+}. Another reason can be the different occupation of the lattice sites in the wurtzite structure. The two different sites, which can be occupied by the Al- or Ga-dopants, are substitutional sites with tetrahedral symmetry and interstitial sites with octahedral symmetry. For Al^{3+} it was shown by NMR that for small concentrations the tetrahedral sites are occupied.[14] Ga^{3+} on the other hand could be expected to preferentially occupy octahedral sites due to their larger ionic radius.[30,38] This is also supported by the analysis of the ZnO lattice parameters obtained by XRD.[30] Rietveld analysis revealed a higher unit cell volume for ZnO:Ga and a slightly smaller volume for ZnO:Al (see Table S.6.1 in the Supporting Information) supporting the assumption that Al^{3+} occupies substitutional sites and Ga^{3+} preferentially octahedral interstitials. It is noted that there are also studies reporting the opposite behavior,[39,40] but here the above mentioned assignment is also supported by a couple of other properties that are different for the two materials, as conductivity behavior, band gap shift relative to the undoped material and ZnO lattice parameters. It seems these properties are also depending on the mode of preparation.

Surface characterization

Depth profiles of the catalyst surface of three samples Cu/ZnO, Cu/ZnO:Mg and Cu/ZnO:Ga have been recorded by XPS after pre-reduction and inert transfer into the measurement cell (see Figure 6.7). Significant deviation of the surface composition from the nominal composition is observed for all three measured samples. The Cu amount is enriched due to the mode of preparation (impregnation), yielding small Cu nanoparticles at the surface of the ZnO support. Different behavior is observed for the dopant. Mg content is constant with 2 - 3 % and corresponding to the nominal value. However the Ga content is strongly increased for the most surface sensitive measurement (8 %) and decreases for more bulk like measurements with higher excitation energy to 0. This behavior agrees very well with the behavior reported previously for ZnO:Al, that upon reduction an enrichment of Al^{3+} towards the surface takes place.[14]

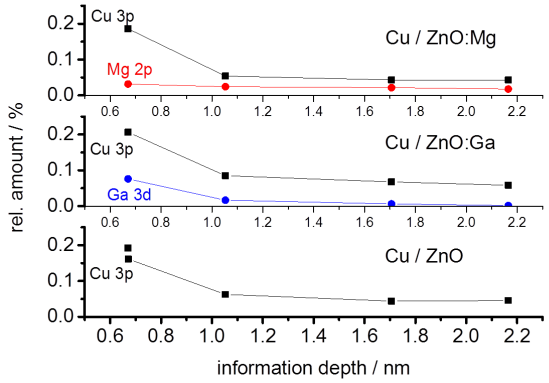

Figure 6.7: Surface compositions with depth profiles as determined by XPS.

6.4.2 Activity in rWGS and MeOH-synthesis

The activity of the catalysts has been tested in reverse water-gas shift (rWGS) at ambient pressure as well as in methanol synthesis at 30 bar. In both reactions the trend regarding the activities was the same for the sample series: the Mg-doped catalyst showed least activity, followed by the undoped catalyst, and highest activity was shown by the Al- and Ga-doped catalysts. This observation agrees well with the conductivity measurements of the supports indicating that the different electronic properties of ZnO as induced by the dopants affect the catalytic properties of Cu/ZnO. The rWGS reaction was tested performed using two different H_2 / CO_2 ratios and setups. With the stoichiometric 1:1 H_2 / CO_2

feed ratio, activities for CO formation of 21 - 31 μmol min^{-1} g$_{cat}^{-1}$ were measured at 503 K for the differently promoted samples. By normalizing the activity per Cu-SA$_{N2O}$, measured by N_2O-chemisorption, a so-called intrinsic activity was calculated (see Figure 6.8). In this reaction, additionally to the unpromoted ZnO samples impregnated with 10% Cu, two samples with 5 and 15 % Cu were tested. The 5 and 10 % samples showed a linear increase in activity and Cu-SA with respect to the copper loading and therefore they had the same intrinsic activity for rWGS. This indicates a homogeneous particle distribution. 15 % copper already led to intrinsically less active catalyst particles (see Figure 6.8), which is why a 10 % Cu loading has been used for comparison of the different supports. Activation energies for CO formation in rWGS were smaller for the more active Al- and Ga-doped samples (87 and 89 kJ mol^{-1}, respectively) and higher for the Mg-doped and unpromoted sample: 98 and 99 kJ mol^{-1}, respectively. This indicates that the tri-valent promoters in the support have a positive effect on the nature of rWGS sites, while Mg did not show a positive nor negative effect in this reaction.

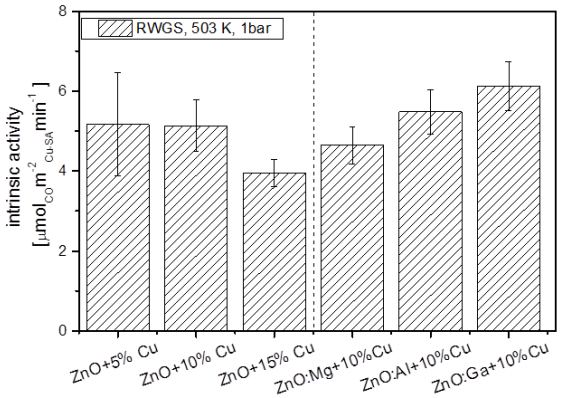

Figure 6.8: Intrinsic activity in rWGS reaction.

The reaction order in H_2 was 0.2 and in CO_2 it was 0.2-0.3 for the tested catalysts (see Table 6.5) which is of the same magnitude of reaction orders reported for Cu-based catalysts in rWGS before.[41] In the study by Ginés et al.[41]41 two different regimes are identified. With excess H_2 (H_2 / CO_2 > 3) the reaction order in hydrogen is negligible, but the reaction order in CO_2 is about 1.1. Under less hydrogen rich conditions, the order in CO_2 is smaller, about 0.3, and the reaction order in H_2 is 0.8. With the testing conditions used in this study (0.3 < H_2 / CO_2 < 3), we were in the transition between both regimes, that is why the reaction order of H_2 matches with the hydrogen rich conditions, but for CO_2 it is closer to CO_2 rich conditions. Furthermore, the reaction orders were influenced by the promoters:

Whereas the reaction order of H_2 decreased slightly upon promotion with the tri-valent cations Al^{3+} and Ga^{3+}, the reaction order in CO_2 increased. This agrees well with the commonly assumed surface redox mechanism for the rWGS,[42] except for the suggestion that clean metallic Cu is regarded as the active phase. The observed facilitated reducibility and the stronger adsorption of H_2 on the Al^{3+} and Ga^{3+} doped supports, indicate an active role of ZnO in the rWGS mechanism. Traces of methanol have been detected by GC under these reaction conditions, but they were below quantification limit. In the hydrogen rich

Table 6.5: Reaction orders of H_2 and CO_2 in rWGS.

	Reaction order H_2	**Reaction order CO_2**
Cu/ZnO	0.183±0.009	0.24±0.02
Cu/ZnO:Mg	0.180±0.001	0.23±0.02
Cu/ZnO:Al	0.150±0.002	0.32±0.02
Cu/ZnO:Ga	0.164±0.004	0.32±0.02

feed gas composition (H_2 / CO_2= 3/1) at ambient pressure methanol could already be quantified in the product stream. The activation energies in methanol synthesis for the more active Cu/ZnO:Ga, Cu/ZnO:Al and Cu/ZnO were determined to be 37-41 kJ mol^{-1} and an activation energy of 50 kJ mol^{-1} was found for Cu/ZnO:Mg showing a detrimental effect of Mg doping for methanol synthesis. Under these conditions, activation energies for rWGS are higher and show less difference with 112 kJ mol^{-1} for Ga and Al promoted catalysts and 115 kJ mol^{-1} for the Mg- doped and undoped sample (see Table 6.6).

Table 6.6: Activation energies in rWGS and methanol synthesis from different feed gases.

	RWGS (H_2/CO_2 = 1/1) CO formation[a] [kJ mol^{-1}]	**RWGS (H_2/CO_2 = 3/1) CO formation[b] [kJ mol^{-1}]**	**MeOH formation[c] (H_2/CO_2 = 3/1; 1 bar) [kJ mol^{-1}]**	**MeOH formation[b] (Syngas; 30 bar) [kJ mol^{-1}]**
Cu/ZnO	98.9±1	115.0±2	40.5±6	52.9±1
Cu/ZnO:Al	87.3±1	111.8±1	39.8±5	56.0±2
Cu/ZnO:Ga	89.1±1	112.1±3	37.2±4	56.9±2
Cu/ZnO:Mg	98.1±1	115.1±2	49.7±5	56.4±1

[a] T = 483-503 K
[b] T = 463-523 K
[c] T = 463-503 K; all errors are calculated from standard error of fit

The order in the activity of methanol synthesis at 30 bar from a typical syngas mixture with a CO_2 / CO / H_2 composition of 8 / 6 / 59 was the same as for the rWGS reaction: Cu/ZnO:Mg was least active, followed closely by Cu/ZnO. Cu/ZnO:Al and Cu/ZnO:Ga were nearly twice as active (see Figure 6.9a). The catalysts were quite stable over the 8 h time on stream, with only minor deactivation. Only Cu/ZnO:Al showed an activation behavior "induction period") and reached steady state after 2 h. The intrinsic activity calculated by normalizing the activity to the N_2O-chemisorption capacity showed smaller differences between the different samples than for rWGS (Figure 6.9b). Cu/ZnO:Al was slightly more active than the other samples, but the differences were low. Only if the activity was normalized to the Cu surface sites determined by H_2-TA, the differences were significant. Cu/ZnO:Al had the highest intrinsic activity, closely followed by Cu/ZnO:Ga. The Mg-doped and unpromoted samples had lower intrinsic activities. The apparent activation energy in this reaction is nearly the same for all the samples with approximately 56 kJ mol^{-1}. This value matches very well with the recently published activation energy of 57 kJ mol^{-1} for a high surface area reference-type catalyst (FHI-std) tested in our laboratory under the same conditions.[35] This indicates the comparability of the active sites of these model-type catalysts prepared by impregnation with industrial relevant systems prepared by co-precipitation.

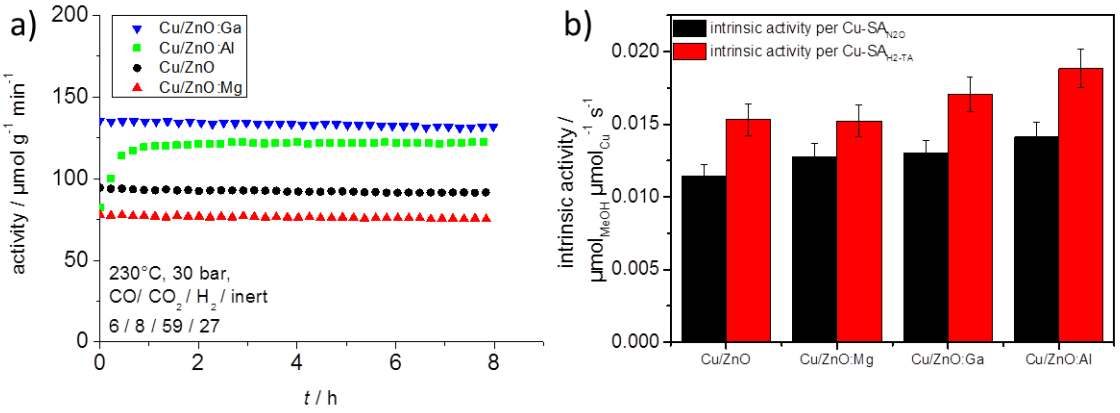

Figure 6.9: Activity of Cu/ZnO:M catalysts in methanol synthesis; a) weight time yield; b) intrinsic activity with respect to differently quantified Cu-sites.

For both reactions - methanol synthesis and rWGS - a dependency of the activity on the promoted support was found. In the rWGS reaction that was tested under mild conditions at ambient pressure and low reduction potential, Al^{3+} and Ga^{3+} clearly work as electronic promoters. The activation energy is lowered and reaction order in hydrogen decreased. At

the same time the intrinsic activity increased. This can be explained by an improvement of the reducibility of the ZnO support and a stronger adsorption of H_2, as was also shown by the conductivity measurements. Although in the commonly assumed surface redox mechanism for the rWGS usually the CO_2 dissociation is regarded as the rate determining step,[41,43] it is plausible to assume a beneficial effect also for the facilitation of the hydrogen adsorption especially under the hydrogen lean conditions used (compared to the usually hydrogen rich conditions used for CO_2 hydrogenation to methanol, where rWGS is regarded as a side reaction).

In methanol synthesis, under much more strongly reducing conditions of 30 bar and high H_2 + CO content, the negligible difference of the activation energy between the differently promoted catalysts indicates, that the electronic effect of the dopants on the ZnO does not significantly affect the energetic state of the active site of the rate determining step(s). The significant differences in intrinsic activity normalized by H_2-TA sites nevertheless point to a significant promoter effect, which must then be a structural effect. Interestingly, if normalized to the N_2O-capacity, the intrinsic activity only showed a much weaker effect of the promoter. It seems that, when comparing differently promoted catalysts with otherwise similar preparation history, the N_2O-chemisorption capacity scales nicely with the activities. Apparently, as the differences between the differently promoted catalysts in N_2O-normalized intrinsic activity were smaller, the oxygen vacancy defects that are probed by N_2O-RFC additionally to the Cu sites are linked to the activity. This can also explain the effect seen for promoted Cu/ZnO:Al catalysts prepared by co-precipitation of zincian malachite, where the intrinsic activity (normalized by the N_2O-capacity) decreases compared to the binary Cu/ZnO catalyst.[13] On the other hand, as shown in chapter 4, if e.g. the calcination temperature is varied, the number of oxygen vacancies does not seem linked to the intrinsic activities.

Oxygen vacancies, as also introduced by the promoter, should be linked to the reducibility of the ZnO and can be interpreted as a measure for the SMSI. The higher mobility of the ZnO and better availability of Zn atoms on the surface and at the steps of the Cu surface lead to a higher number of active sites for methanol synthesis, and a greater Cu-ZnO interface, which would explain the structural promoter effect seen for Al^{3+} and Ga^{3+} doped Cu/ZnO catalysts. Although the XPS data do not support an increased presence of Zn on the surface for the Cu/ZnO:Ga sample compared to the unpromoted and Cu/ZnO:Mg sample. However, this might be due to the fact that the XPS measurement was not performed under high pressure in-situ conditions, where the mobility of ZnO could

be more effective. A pressure dependent change of the active site is also supported by the observation that the activation energy for methanol is approximately 10 kJ mol^{-1} lower at ambient pressure and additionally depending on the promoter. Additionally charge transfer between the semiconductor and the metal, or band bending by defect states at the surface could explain the promoting effect of the Al^{3+} and Ga^{3+} dopant. Already Frost suggested the formation of a Schottky-junction as origin of the Cu-ZnO synergy.[44]

6.5 Summary and Conclusion

We successfully prepared Cu/ZnO catalysts in a two-step procedure, which allowed us to study the effect of different promoters onto the oxide support independently from the active metal part. Insights into the electronic structure of ZnO as a catalyst support and the influence of different dopants were provided by contactless conductivity measurements, EPR and UV-vis spectroscopy, and TPR measurements. Surface sensitive measurements of the impregnated catalysts yielded additional information of the active state. Comparison of the characterization data of the supports with the results from the activity measurements revealed parallel trends with respect to the dopants. While the tri-valent promoters Al^{3+} and Ga^{3+} improve conductivity and increase the defect level in the support, the Mg^{2+} dopant decreases the conductivity of the ZnO support. The catalytic data show that although the active phase is metallic copper, the promoted ZnO significantly influences the activity. From the rWGS activity data it is clear, that Al^{3+} and Ga^{3+} act as electronic promoters in the ZnO, lowering the activation energy and facilitating the H_2 activation. Mg^{2+} on the other hand has no significant influence on the activity. The small differences of the activation energy in methanol synthesis at 30 bar indicate that Al^{3+} and Ga^{3+} either are not influencing the rate-determining step of methanol synthesis or rather act as structural promoters for this reaction. Due to the highly reducing reaction conditions during methanol synthesis, a facilitated reducibility of ZnO seems not that important compared to less reducing reaction conditions with more CO_2. Although we assume that the different promoters stay in the lattice of the ZnO support, it might also be possible, that the promoters migrate into the Cu component under reaction conditions and effect the activity from there. The mobility and resulting surface enrichment of the Al^{3+} and Ga^{3+} promoter under reducing conditions was shown by XPS depth profiling. We show, that the SMSI can be tuned by the use of suitable cations to promote structurally and electronically the active site for rWGS and methanol synthesis.

6.6 Acknowledgements

The authors thank Wiebke Frandsen, Gisela Weinberg and Norbert Pfänder for SEM measurements and micrograph treatment, Pierre Kube for help with rWGS measurements, Jasmin Allan for XRD and Maike Hashagen for BET measurements.

6.7 References

[1] M. Behrens, F. Studt, I. Kasatkin, S. Kühl, M. Hävecker, F. Abild-Pedersen, S. Zander, F. Girgsdies, P. Kurr, B. L. Kniep, M. Tovar, R. W. Fischer, J. K. Nørskov, R. Schlögl, *Science* **2012**, *336*, 893.

[2] M. S. Spencer, *Top. Catal.* **1999**, *8*, 259.

[3] J.-D. Grunwaldt, A. Molenbroek, N.-Y. Topsøe, H. Topsøe, B. Clausen, *J. Catal.* **2000**, *194*, 452.

[4] Y. Choi, K. Futagami, T. Fujitani, J. Nakamura, *Appl. Catal., A* **2001**, *208*, 163.

[5] R. Burch, S. E. Golunski, M. Spencer, *J. Chem. Soc., Faraday Trans.* **1990**, *86*, 2683.

[6] M. Spencer, *Catal. Lett.* **1998**, *50*, 37.

[7] N.-Y. Topsøe, H. Topsøe, *Top. Catal.* **1999**, *8*, 267.

[8] R. Naumann d'Alnoncourt, X. Xia, J. Strunk, E. Löffler, O. Hinrichsen, M. Muhler, *Phys. Chem. Chem. Phys.* **2006**, *8*, 1525.

[9] V. Schott, H. Oberhofer, A. Birkner, M. Xu, Y. Wang, M. Muhler, K. Reuter, C. Wöll, *Angew. Chem. Int. Ed.* **2013**, *52*, 11925.

[10] Y. Kanai, T. Watanabe, T. Fujitani, M. Saito, J. Nakamura, T. Uchijima, *Catal. Lett.* **1994**, *27*, 67.

[11] B. E. Koel, J. Kim, *Handbook of Heterogeneous Catalysis*, chapter Promoters and Poisons, Wiley-VCH, Weinheim, **2008**, pp. 1593–1624.

[12] J. B. Hansen, P. E. H. Nielsen, *Handbook of Heterogeneous Catalysis*, chapter Methanol Synthesis, Wiley-VCH, Weinheim, 2nd Edition, **2008**, pp. 2920–2944.

[13] M. Behrens, R. Schlögl, *Z. anorg. allg. Chem.* **2013**, 2683.

[14] M. Behrens, G. Lolli, N. Muratova, I. Kasatkin, M. Hävecker, R. N. d'Alnoncourt, O. Storcheva, K. Kohler, M. Muhler, R. Schlögl, *Phys. Chem. Chem. Phys.* **2013**, *15*, 1374.

[15] U. Özgür, Y. Alivov, C. Liu, A. Teke, M. Reshchikov, S. Dogan, V. Avrutin, S. Cho, H. Morkoc, *J. Appl. Phys.* **2005**, *98*.

[16] A. Coelho, *TOPAS: General Profile and Structure Analysis Software for Powder Diffraction Data; Bruker AXS GmbH: Karlsruhe, Germany* **2006**, *version 3.0*.

[17] G. Chinchen, C. Hay, H. Vandervell, K. Waugh, *J. Catal.* **1987**, *103*, 79.

[18] S. Kuld, C. Conradsen, P. G. Moses, I. Chorkendorff, J. Sehested, *Angew. Chem. Int. Ed.* **2014**, *53*, 5941.

[19] R. Weber, *J. Catal.* **1995**, *151*, 470.

[20] A. Khodakov, B. Olthof, A. T. Bell, E. Iglesia, *Journal of Catalysis* **1999**, *181*, 205.

[21] K. Chen, A. T. Bell, E. Iglesia, *J. Catal.* **2002**, *209*, 35.

[22] D. Barton, M. Shtein, R. Wilson, S. Soled, E. Iglesia, *J. Phys. Chem. B* **1999**, *103*, 630.

[23] R. Smith, *Semiconductors*, Cambridge University Press, 2nd edn. Edition, **1978**.

[24] M. Eichelbaum, R. Stoßer, A. Karpov, C.-K. Dobner, F. Rosowski, A. Trunschke, R. Schlogl, *Phys. Chem. Chem. Phys.* **2012**, *14*, 1302.

[25] C. Heine, F. Girgsdies, A. Trunschke, R. Schlögl, M. Eichelbaum, *Appl. Phys. A* **2013**, *112*, 289.

[26] R. Shannon, *Acta Cryst. A* **1976**, *32*, 751.

[27] Z. Chen, G. Zhan, Z. Lu, *J. Mater. Sci.* **2014**, *25*, 1724.

[28] R. Zamiri, B. Singh, M. Scott Belsley, J. Ferreira, *Ceram. Int.* **2014**, *40*, 6031.

[29] H. Serier, M. Gaudon, M. Ménétrier, *Solid State Sci.* **2009**, *11*, 1192.

[30] A. Kaul, O. Gorbenko, A. Botev, L. Burova, *Superlattices Microst.* **2005**, *38*, 272.

[31] X. Zhang, X. Pu, Y. Chen, X. Gu, D. Xu, S. Zhang, *Mater. Lett.* **2013**, *112*, 129.

[32] J. Iqbal, T. Jan, M. Ismail, N. Ahmad, A. Arif, M. Khan, M. Adil, S. ul Haq, A. Arshad, *Ceram. Int.* **2014**, *40*, 7487.

[33] M. B. Fichtl, J. Schumann, I. Kasatkin, N. Jacobsen, M. Behrens, R. Schlögl, M. Muhler, O. Hinrichsen, *Angew. Chem. Int. Ed.* **2014**, *53*, 7043.

[34] J. Sloczynski, R. Grabowski, A. Kozlowska, P. K. Olszewski, J. Stoch, *Phys. Chem. Chem. Phys.* **2003**, *5*, 4631.

[35] J. Schumann, T. Lunkenbein, A. Tarasov, N. Thomas, R. Schlögl, M. Behrens, *ChemCatChem* **2014**, *6*, 2889.

[36] S. Kühl, A. Tarasov, S. Zander, I. Kasatkin, M. Behrens, *Chem. Eur. J.* **2014**, *20*, 3782.

[37] V. Ischenko, S. Polarz, D. Grote, V. Stavarache, K. Fink, M. Driess, *Adv. Funct. Mater.* **2005**, *15*, 1945.

[38] N. Vorobyeva, M. Rumyantseva, R. Vasiliev, V. Kozlovskii, Y. Soshnikova, D. Filatova, A. Baranchikov, V. Ivanov, A. Gaskov, *Russian Journal of Inorganic Chemistry* **2014**, *59*, 403.

[39] M. Gabás, A. Landa-Cánovas, J. Luis Costa-Krämer, F. Agulló-Rueda, A. R. González-Elipe, P. Díaz-Carrasco, J. Hernández-Moro, I. Lorite, P. Herrero, P. Castillero, A. Barranco, J. Ramón Ramos-Barrado, *J. Appl. Phys.* **2013**, *113*, 163709.

[40] M. Gabás, P. Torelli, N. T. Barrett, M. Sacchi, J. R. Ramos Barrado, *APL Materials* **2014**, *2*, 12112.

[41] M. Ginés, A. Marchi, C. Apesteguía, *Appl. Catal., A* **1997**, *154*, 155.

[42] G. Chinchen, M. Spencer, *J. Catal.* **1988**, *112*, 325.

[43] G.-C. Wang, J. Nakamura, *J. Phys. Chem. Lett.* **2010**, *1*, 3053.

[44] J. C. Frost, *Nature* **1988**, *334*, 577.

6.8 Supplementary information

Results from Rietveld refinement

Table S.6.1: Lattice parameters as obtained from Rietveld refinement, preferred orientation order 6.

Spacegroup: P 63mc	Lattice vector a	Lattice vector c	Unit cell volume
ZnO	3.25151(25)	5.21042(47)	47.7060(86)
ZnO:Al	3.25084(54)	5.20656(95)	47.651(18)
ZnO:Ga	3.25483(30)	5.21031(52)	47.803(10)
ZnO:Mg	3.25193(19)	5.21126(34)	47.7261(64)

Uncolored and additional SEM images

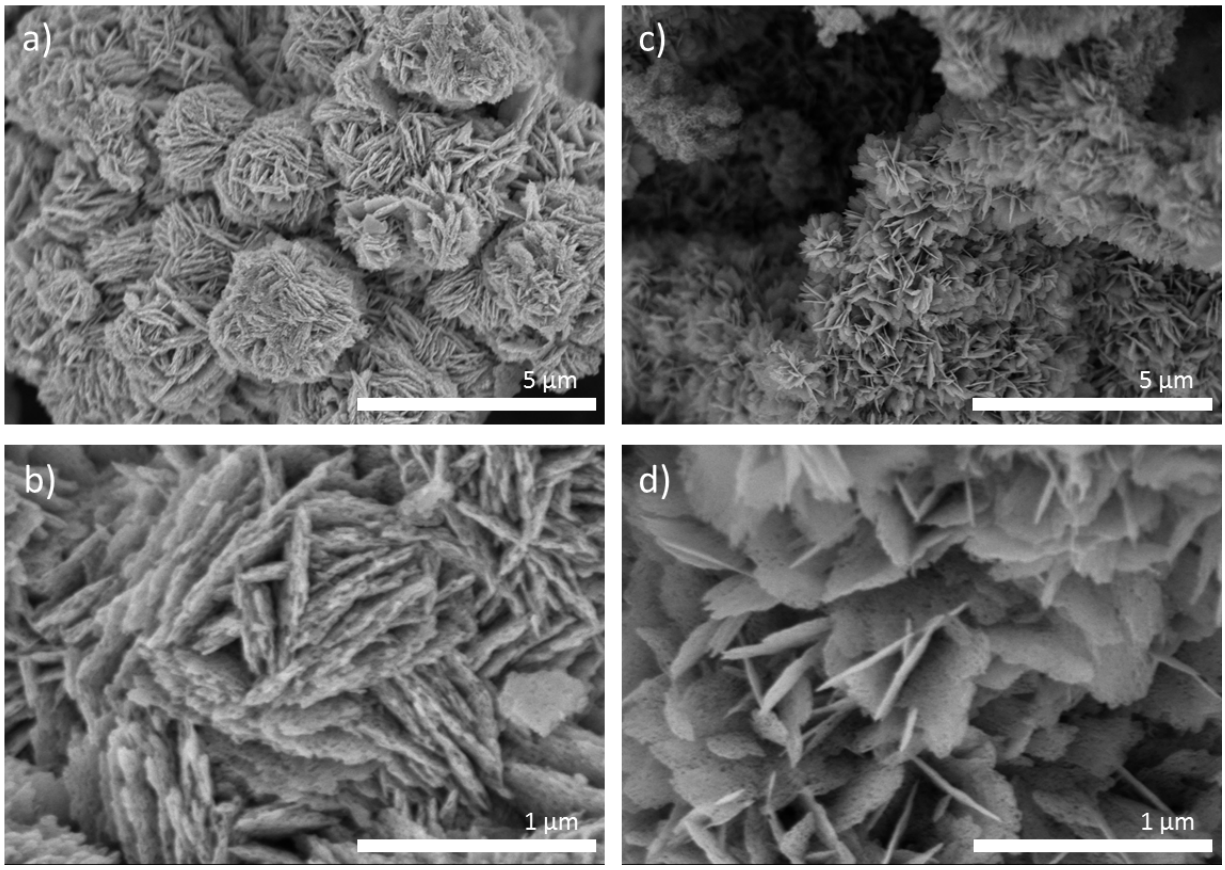

Figure S.6.1: Uncolored versions of SEM images from Figure 6.2 a-d).

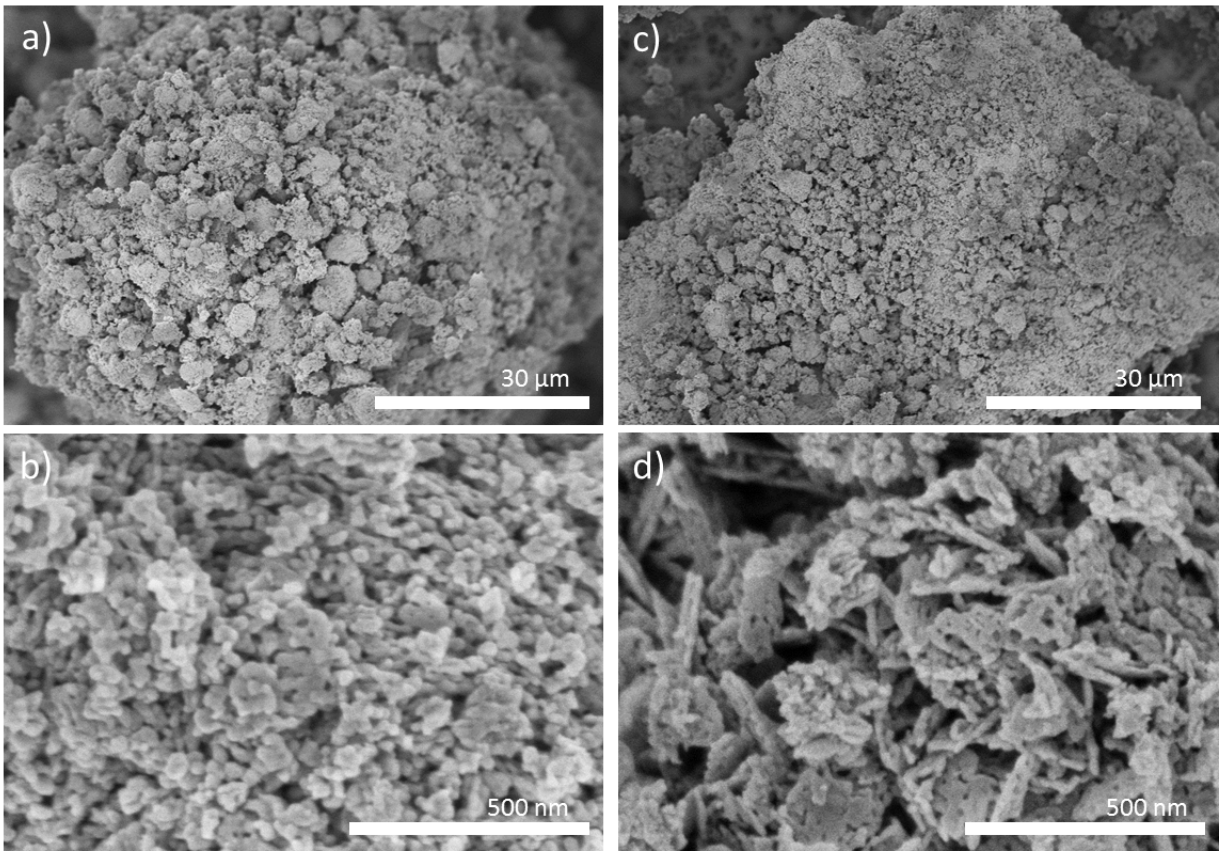

Figure S.6.2: Uncolored versions of SEM images from Figure 6.2 e,f).

Uncolored and additional STEM images

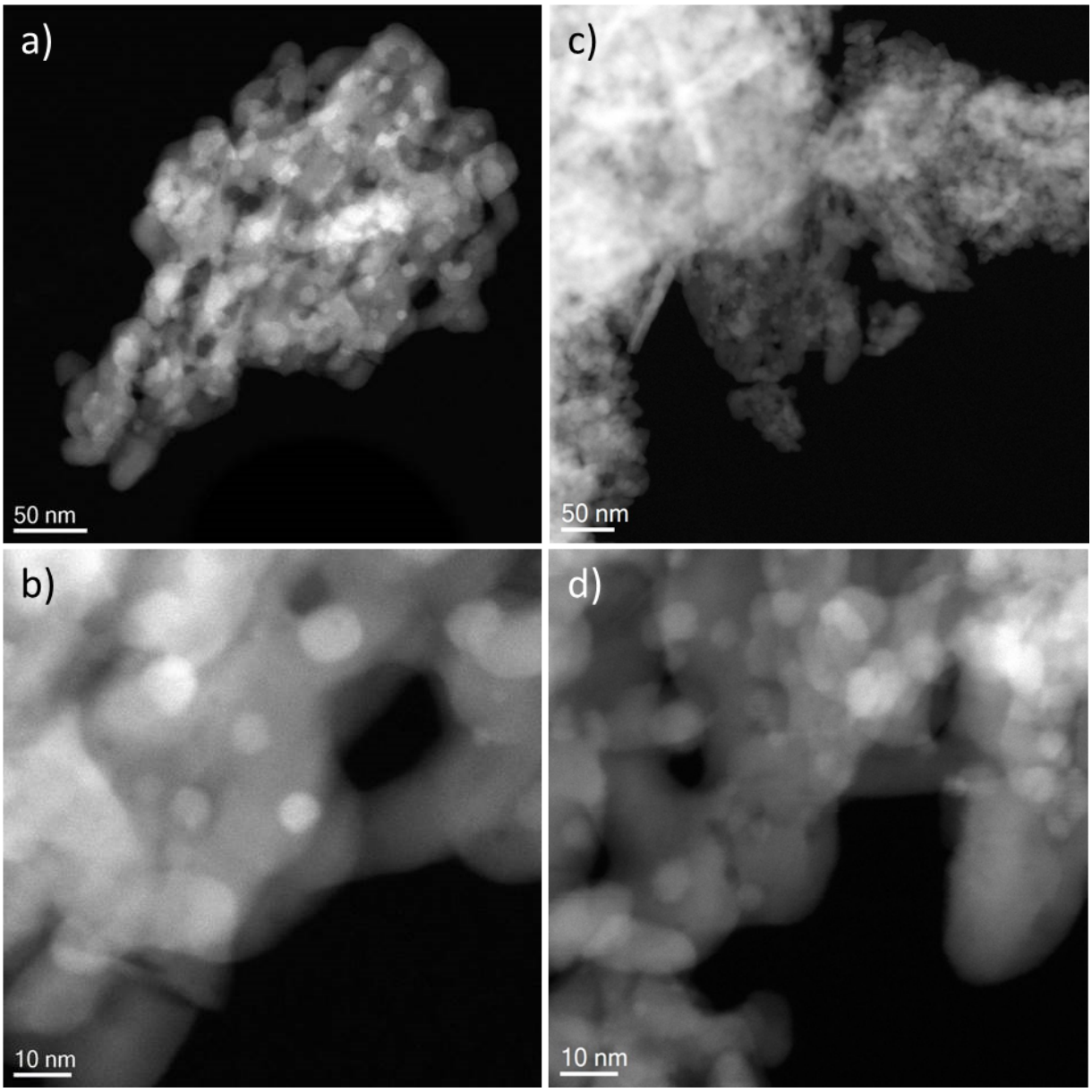

Figure S.6.3: Uncolored versions of STEM images. a), b) Cu/ZnO and c), d) Cu/ZnO:Al.

List of sample numbers

Table S.6.2: Internal sample numbers from FHI for future reference.

	support		**impregnated sample for rWGS measurement**	**impregnated samples for characterization and MeOH synthesis measurements**	**reduced samples measured at Bessy**
ZnO	# 13835	+5 % Cu	#12864		
		+10 % Cu	#12888	#16579	#16914
		+15 % Cu	#12984		
ZnO: Al	#13845 / #12042 / #18199	+10 % Cu	#13195	#16736	
ZnO: Ga	#13834 / #12028	+10 % Cu	#13213	#16630	#16907
ZnO: Mg	#12041	+ 10 % Cu	#13214	#16580	#16905

7 Summary and final conclusion

In this thesis binary Cu/ZnO as well as promoted ternary catalysts were prepared, characterized, and tested in CO_2-conversion reactions in order to get better insights into structure-function relationships. For binary Cu/ZnO catalysts with different Cu/Zn ratios it was shown, that aurichalcite precursors yielded superior catalysts in rWGS over zincian malachite. Beneficial microstructure, with higher BET-SA and smaller CuO domain size was obtained from catalysts with lower Cu-content and aurichalcite precursor structure. Consequently, the aurichalcite derived catalysts showed higher activity in the rWGS.

By varying the heating ramp from 0.1 to 2 $K\,min^{-1}$ during calcination up to 603 K, the amount of HT-CO_3 in calcined catalysts prepared from both ZM and AU precursors could be adjusted, corresponding to an additional weight loss during further calcination from 8 to 3 %. Presence of large amounts of HT-CO_3, after very mild calcination conditions, indicated that no significant segregation and crystallization of CuO and ZnO took place, in line with previous reports associating the HT-CO_3 with a large Cu/Zn interface. However despite distinct changes in crystallinity, decomposition profile and IR absorption, the differences of the catalytic activity in methanol synthesis were small and did not reveal a beneficial effect of a high HT-CO_3 content. On the contrary, dilution of the active Cu by carbonate, led to a decrease of activity in methanol synthesis per mass of calcined catalyst. The different precursor phases AU and ZM yielded catalysts with very similar activities in methanol synthesis after 15 h TOS. Contrary to the results obtained from rWGS, in methanol synthesis ZM derived catalysts started with a higher activity than AU catalysts. A faster deactivation was observed for the ZM samples and led to matching activities of both series after some reaction time.

For both precursor phases, AU and ZM, a significant increase in surface area and decrease of crystallite size was observed upon promotion with 3 % Al, proving that already small amounts of Al act as an efficient structural promoter, disturbing large crystallite growth and changing morphology of ZM. Promotion with 3 % Al led also to a significant stabilization of HT-CO_3 and thus to a restraint of crystallization during the calcination procedure.

Calcination at higher temperature than the usual 603 K led to a decrease in HT-CO_3 until at 793 K negligible HT-CO_3 was present in both promoted AU and ZM samples. It could be shown, that within the two sample series with different calcination temperatures the activity in methanol synthesis was not proportional to the surface sites measured by N_2O-RFC. The intrinsic activity seemed to increase with higher calcination temperature of the catalyst. It turned out, that this was an effect originating from the high amount of oxygen vacancies in ZnO in the samples calcined at lower temperatures. These vacant sites measured additionally to Cu-surface sites by N_2O-RFC did not contribute to the measured activities and thus lowered the calculated intrinsic activities. As was shown for the binary samples, a high amount of HT-CO_3 in the calcined sample did not lead to a high intrinsic activity in methanol synthesis, but it acted as a structural stabilizer, leading to high surface areas and resulted in a high number of oxygen vacancies in the ZnO component of the catalysts. Based on these results, the amount of HT-CO_3 in the calcined catalysts was established as a good probe for mild calcination conditions ensuring no strong sintering due to high water content in the atmosphere during calcination took place.

When comparing ZM and AU as precursors for methanol synthesis catalysts, it occured, that the Al promotion of ZM was much more effective than for AU. From the comparable binary starting point, e.g. in terms of N_2O-sites, a much stronger improvement was achived for ZM. One possible explanation could be, that a higher amount of Al is needed for optimal promotion of AU, as we also have a higher ZnO content in the AU sample.

What was observed for both precursor phases, is that the stability in methanol synthesis increased by an order of magnitude upon promotion with small amounts of Al. The increased stability is assumed to derive from Al doping of ZnO keeping the ZnO in the defective state with a high Cu/Zn interface and preventing it from dewetting and recrystallization. Activities normalized by the number of easily reducible surface sites, determined by H_2-TA, were comparable for both promoted sample series.

The highly active Al-promoted ZM derived catalyst was characterized in-depth at various stages of catalyst preparation. This uniform nano- and mesostructured composite material with small copper particle size, very high N_2O chemisorption capacity and high defect density enabled very high activity in methanol synthesis from CO_2-containing feed gases.

In order to better understand the role of the Al promoter on a fundamental level Cu/ZnO model-type catalysts were prepared in a two-step procedure, with the addition of the copper in a second impregnation step. The zinc oxide support could thus be studied

independently from the active metal part. Apart from the Al promoter, Ga^{3+} and Mg^{2+} were tested as dopants in order to be able to better judge on trends. ZnO was shown to be influenced tremendously by the different dopants. In addition to the structural impact of the dopants, which leads to smaller domain sizes and larger surface areas of the ZnO, electronic structure changes were also observed. Small amounts of the n-dopants Al^{3+} and Ga^{3+} led to a decrease of the optical band gap, introduction of ionized states and a strong increase of the microwave frequency conductivity. On the other hand, the Mg^{2+} dopant led to an increase of the optical band gap and a strong decrease of charged defects and conductivity. Comparison of the electronic structure data of the doped supports with the results from the activity measurements of the copper containing catalysts revealed parallel trends with respect to the dopants. Although the active phase in rWGS and methanol synthesis is commonly considered to be metallic copper, the promoted ZnO significantly influenced the activity. From the kinetic data of the rWGS reaction it is clear, that Al^{3+} and Ga^{3+} act as electronic promoters in the ZnO. The activation energy is lowered and the H_2 activation is facilitated. Mg^{2+} on the other hand has no significant influence on the activity. Smaller differences of the differently doped samples were observed for the activation energy in methanol synthesis at 30 bar. Due to the highly reducing reaction conditions during methanol synthesis, a facilitated reducibility of ZnO seems not that important compared to less reducing reaction conditions with more CO_2 during rWGS. The SMSI can be tuned by the use of suitable cations to promote structurally and electronically the active site for rWGS and methanol synthesis.

This work contributes to a better understanding of the industrial methanol synthesis catalyst. In particular, it highlights the role of realistic features of the active catalyst that are often neglected in model studies like its preparation history as inherited from the different precursor phases, the presence of small amounts of promoting species and residual carbonate in the pre-catalyst. These features were shown to have important and decisive effects on the catalytic activity and stability. The results reported in this thesis thus serve as a guideline of how to control the catalytic performance through structural and electronic control of the active phase, which in turn can be tuned by careful synthesis. Thorough understanding is the prerequisite of a knowledge-based catalyst design and adjustment to changed parameters which arise from the necessary change towards the sustainable feedstock of the future.

Appendix

List of publications

F. Studt, M. Behrens, E. L. Kunkes, N. Thomas, S. Zander, A. Tarasov, J. Schumann, E. Frei, J. B. Varley, F. Abild-Pedersen, J. K. Nørskov, R. Schlögl: The mechanism of CO and CO_2 hydrogenation to methanol over Cu based catalysts, *ChemCatChem* **2015**, DOI: 10.1002/cctc.201500123.

T. Lunkenbein, J. Schumann, M. Behrens, R. Schlögl, M. Willinger: Self-assembled catalyst promotion by overgrowth of layered ZnO in industrial $Cu/ZnO/Al_2O_3$ catalysts, *Angew. Chem. Int. Ed.* **2015**, DOI: 10.1002/anie.201411581.

J. Schumann, T. Lunkenbein, A. Tarasov, N. Thomas, R. Schlögl, M. Behrens: Synthesis and Characterisation of a Highly Active Cu/ZnO:Al Catalyst, *ChemCatChem* **2014**, *6*, 2889-2897.

M. B. Fichtl, J. Schumann, I. Kasatkin, N. C. Jacobsen, M. Behrens, R. Schlögl, M. Muhler, O. Hinrichsen: Counting of oxygen defects vs. metal surface sites in methanol synthesis catalysts by different probe molecules, *Angew. Chem. Int. Ed.* **2014**, *53*, 7043-7047.

A. Tarasov, J. Schumann, F. Girgsdies, N. Thomas, M. Behrens: Thermokinetic investigation of binary Cu/Zn hydroxycarbonates as precursors for Cu/ZnO catalysts, *Thermochim. Acta* **2014**, *591*, 1-9.

A. Tarasov, S. Kühl, J. Schumann, M. Behrens: Thermokinetic study of the reduction process of a $CuO/ZnAl_2O_4$ catalyst, *High Temp-High Press* **2013**, *42*, 377-386.

S. Zander, E. L. Kunkes, M.E. Schuster, J. Schumann, G. Weinberg, D. Teschner, N. Jacobsen, R. Schlögl, M. Behrens: The Role of the Oxide Component in the Development of Copper Composite Catalysts for Methanol Synthesis; *Angew. Chem. Int. Ed.* **2013**, *52*, 6536-6540.

J. Chen, H. Ye, L. Aé, Y. Tang, D. Kieven, T. Rissom, J. Neuendorf, M.C. Lux-Steiner: Tapered aluminum-doped vertical zinc oxide nanorod arrays as light coupling layer for solar energy applications; *Sol. Energ. Mat. Sol.* **2011**, *95*, 1437-1440.

Matthias B. Fichtl, David Schlereth, Nikolas Jacobsen, I. Kasatkin, J. Schumann, M. Behrens, R. Schlögl, K.-O. Hinrichsen: Kinetics of deactivation on $Cu/ZnO/Al_2O_3$ methanol synthesis catalysts, Appl. Catal. A, submitted.